THESIS FOR DEGREE OF LICENTIATE OF ENGINEERING

Adding Utility to Carbon Materials: Introducing Dopants Using Highly Soluble Metal Salts and Functionalizing Surfaces via Bromomethylation

SAMUEL JOSEPH FRETZ

CHALMERS

Department of Chemistry and Chemical Engineering
CHALMERS UNIVERSITY OF TECHNOLOGY
Gothenburg, Sweden 2018

Adding Utility to Carbon Materials: Introducing Dopants Using Highly Soluble Metal Salts and Functionalizing Surfaces via Bromomethylation

SAMUEL JOSEPH FRETZ

Licentiatuppsatser vid Institutionen för kemi och kemiteknik
Chalmers tekniska högskola.
Nr 2018:03

Department of Chemistry and Chemical Engineering
Chalmers University of Technology
SE-412 96 Gothenburg
Sweden
Telephone +46 (0)31-772 1000

Cover: A visual representation of the utility of the bromomethylation reaction. In the first step, the carbon surface is functionalized using this reaction, which is followed by bromide displacement with diallylamine. In the final step, sulfur is infused with the carbon using heat treatment at 155°C, then at 185°C to polymerize the sulfur with the allyl groups. This surface-polymerized sulfur showed improved performance in lithium-sulfur batteries.

Printed by:
Chalmers Reproservice
Gothenburg, Sweden 2018

Abstract

Carbon-based materials have received intense research interest over the past few decades due to their outstanding combination of properties including porosity, non-toxicity, chemical inertness, low density, and electrical conductivity, which has allowed them to find a wide array of applications including supercapacitors, batteries, CO_2 capture, fuel cells and catalysis. To expand their utility, a variety of techniques have been developed to enhance their reactivity and functionality. One such method is doping, wherein heteroatoms (i.e. non-carbon elements) are purposefully incorporated into the carbon structure with the goal of introducing new reactivity to the material. In this thesis, several systematic studies were carried out on copper and iron salts as dopants for ordered mesoporous carbons (OMC). It was found that the selection of the counter anion to the metal cation has a profound influence on the resultant OMC's structure, chemical composition, metal loadings, and the type of metal obtained (i.e. chelated ions or nanoparticles). We applied a host of characterization methods to elucidate the effect that the anion has on the transition metal-doped OMC. Many copper salts were used to create copper-doped OMCs (Cu-OMCs). High copper loadings of about 5-8 wt% were obtained from using $Cu(BF_4)_2$-nH_2O as the dopant salt, compared to previous loadings of < 1 wt% using iron salts. The copper species was determined to be metallic copper (Cu^0) nanoparticles with diameters of about 40-50 nm. The high copper loadings, however, were found to be deleterious for use as sulfur hosts in lithium-sulfur (Li-S) batteries, with reversible capacities about 50% lower than undoped OMCs. The Cu-OMCs were also tested for O_2 reduction on rotating disc electrodes (RDEs), but their catalytic performance was found to be quite poor. The same approach of using different anions was applied to iron salts in the context of polymer electrolyte membrane fuel cells (PEMFCs). The anion was found to have a strong effect on the OMCs structure, iron loading, and O_2 reduction activity. High iron loadings of above 3 wt% were obtained for some of the soluble salts, but their activity in PEMFCs did not increase appreciably compared to the standard chloride salt.

Another method for increasing the utility of carbon materials is grafting or surface functionalization, which consists of covalently attaching small, organic molecules to the carbon surface. In the last part of this thesis, we report a novel grafting method – the bromomethylation reaction. Several carbon materials efficiently and reproducibly undergo this reaction and surface-bound bromomethyl groups are stable for months in ambient conditions. Subsequently, many nucleophiles can substitute bromide resulting in monolayer-functionalized surfaces tailored for a specific application. We employ diallylamine and ethylenediamine as nucleophiles to produce amine-functionalized carbons for use as the conductive additive for sulfur in Li-S batteries. Such carbons exhibit improved performance over their unmodified precursors demonstrating the utility of this two-step scheme for functionalizing carbon surfaces. We hope that this two-step method of introducing organic groups to carbon surfaces will find wide-spread use in many applications.

List of Publications

I. Influence of Iron Salt Anions on Formation and Oxygen Reduction Activity of Fe/N-Functionalized Mesoporous Carbon Catalysts
S. J. Fretz, C. Janson, W. R. Rosas, and A. E. C. Palmqvist
Manuscript

II. Bromomethylation of Carbon: A Versatile Synthetic Building Block for Functional Surfaces
S. J. Fretz, C. T. Lyons, E. Levin, C. E. D. Chidsey, T. D. P. Stack, and A. E. C. Palmqvist
Manuscript

Contribution Report to the Listed Publications

I. I prepared all Fe-OMCs and characterized them with N_2-sorption, XRD, TGA, and EA. I wrote the majority of the first draft of the manuscript and was the main author.

II. I prepared and characterized Br-Vulcan, All_2N-Vulcan, EN-Vulcan. I also prepared and characterized Vulcan+S, All_2N-Vulcan+S, and EN-Vulcan+S and studied them in Li-S batteries. I wrote the majority the majority of the first draft of the manuscript and was the co-first author.

Table of Contents

Abbreviations

PS	polysulfides
LiPS	lithium polysulfides
pTSA	*para*-toluenesulfonic acid
Li-S	Lithium-sulfur (batteries)
PEMFC	polymer electrolyte membrane fuel cell or proton exchange membrane fuel cell
OTf	trifluoromethanesulfonate or triflate
OAc	acetate
FNH_2	furfurylamine
FOH	furfuryl alcohol
OMC	ordered mesoporous carbon
Cu-OMC	copper-doped ordered mesoporous carbon
Fe-OMC	iron-doped ordered mesoporous carbon
Cu NP	copper(0) nanoparticle
ORR	oxygen reduction reaction
TGA	thermogravimetric analysis
DSC	differential scanning calorimetry
EA	elemental analysis
XRD	X-ray diffraction
SAXS	small angle X-ray scattering
XRF	X-ray fluorescence
XPS	X-ray photoelectron spectroscopy
TEM	transmission electron microscopy
BET	Brunauer-Emmett-Teller (theory for surface area determination)
BJH	Barett-Joyner-Halenda (theory for determination of pore volumes and diameters)

1 Introduction

The 21st Century could very well become the most important century in human history. During the upcoming decades, humanity will face many unprecedented challenges – climate change, overpopulation, and rampant pollution to name a few. Furthermore, the ever-increasing desire of developing countries and communities to become industrialized puts pressure on the environment and its limited resources. A large part of industrialization and, indeed, of living a comfortable lifestyle, is reliable access to electricity. Post-industrial countries such as those in North America and Europe used combustion of reduced carbon reagents – coal and hydrocarbons – to power their industrial revolutions and the subsequent electrification. If such methods are used by the developing world and its large population in the current era, the resultant pollution will surely prove too much for the environment to handle. Thus, the burden falls on scientists and engineers to invent new methods for creating and storing electricity, not just for the developing world, but also to replace the old combustion-based systems still in place in the post-industrial world.

Electricity, by its nature, requires a conductive medium through which to move. Well-known examples of conductors include metals such as copper, silver, gold, iron, and lead. Less well known is common carbon. While not as conductive as the aforementioned metals (see Table 3), carbon exhibits many advantages including low cost, high abundance, porosity, non-toxicity, chemical inertness, and low density. More importantly, carbon possesses the unique ability to form four strong covalent bonds to itself and to most other elements in the Periodic Table. Such propensity for diverse bonding arrangements has required chemists to dedicate a whole sub-discipline of chemistry to carbon – organic chemistry. This ability also allows for easily tunable properties in the element itself; the characteristics of simple, everyday charcoal can be modulated effectively by changing its elemental composition or covalently bonding organic molecules to its surface. Ironically, carbon, which powered the Industrial Revolution and supplied the concomitant pollution, may also provide the necessary material properties for clean, renewable electricity, not as the fuel itself, but as an integral, indispensable component of 21st Century technologies.

Humanity's familiarity with carbon may also provide some distinct advantages for using this material in emerging technologies. Carbon is one of the few elements that has been known to human beings since ancient times. To the earliest human civilizations, carbon was known in the forms of soot and charcoal.[1] One of the main allotropes of carbon, diamond, was likely known to the Chinese as early as 2500 BCE.[2] The other common allotrope of carbon, graphite, was probably recognized in antiquity but was likely confused with minerals of similar appearance and texture like molybdenite (MoS_2).[3] Whereas diamond is sp^3 hybridized and possesses properties such as optical transparency, extreme hardness, and electrical insulation, graphite is sp^2 hybridized and

displays strong visible absorptions, soft, lubricating properties, and electrical conductivity. If the carbon material does not show any long-range order, it is usually referred to as amorphous carbon (sometimes called charcoal) and exhibits a mixture of sp^2 and sp^3 hybridization. This type of carbon, however, typically shares more characteristics with graphite, namely the appearance (black) and electrical conductivity. It is this form of carbon that has found prominent use in energy applications. In Roman times, amorphous carbon was made by heating wood in a clay dome.[3] This is the same chemistry that is used to make carbon today – a technique called *pyrolysis* or *carbonization*.

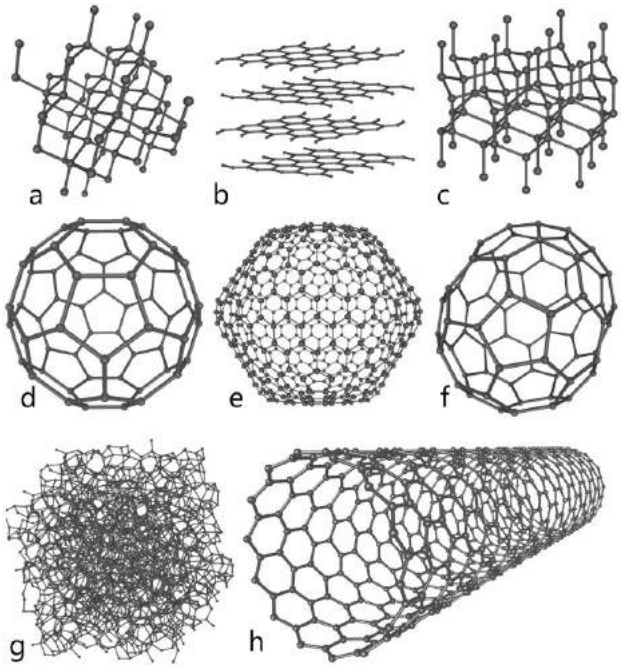

Figure 1. The structures of eight allotropes of elemental carbon. a) Diamond, b) Graphite, c) Lonsdaleite, d) C_{60} also called Buckminsterfullerene), e) C_{540} Fullerene, f) C_{70} Fullerene, g) Amorphous carbon, h) Single-walled carbon nanotube. This thesis is primarily concerned with the amorphous allotrope of carbon.[4]

Amorphous carbons are of considerable research interest because they are easy to make and modify and have tunable properties to meet the demands of a given application, which include batteries, fuel cells, supercapacitors, CO_2 capture, and catalysis among others. The central theme of this thesis is the synthesis and modification of amorphous carbons with the goal of improving their performance in batteries and fuel cells.

This thesis is divided into four Studies. The objective of Studies 1, 2, and 3 was to change the elemental composition of amorphous carbons by incorporating heteroatoms (non-carbon atoms) into the carbonaceous structure. The heteroatoms, also called *dopants*, should lead to the formation of surface sites for favorable interactions with sulfur in lithium-sulfur (Li-S) batteries or for catalytic oxygen (O_2) reduction to water in polymer electrolyte membrane fuel cells (PEMFCs). Study 4 focuses on covalently bonding organic functional groups to the carbon surface in a

process called *grafting*. Such surface-bound groups were chosen to strongly bind to sulfur species undergoing redox chemistry in Li-S batteries.

2 Background

2.1 Carbon synthesis

2.1.1 Natural and artificial carbon synthesis

Three of the main allotropes of carbon - graphite, diamond, and amorphous - are formed in three very distinct ways. Naturally occurring graphite forms in either metamorphic or igneous environments in the Earth's crust from amorphous precursors like coal and decaying organic matter, requiring high temperature and pressure. Graphite is never formed in sedimentary environments. Formation of graphite requires that the local concentration of oxygen be low or else carbon oxides (CO and CO_2) are formed.[5] Diamond, by contrast, is not formed within the Earth's crust, but rather deep within the Earth's mantle at depths of 140 to 190 kilometers, where the pressure is much greater than for the formation of graphite. Carbon-containing minerals provide the carbon source and the diamond growth occurs slowly, over periods of 1 to 3.3 billion years. After formation, diamonds are brought to the Earth's surface by volcanic activity. Despite common belief, diamonds are *not* formed from coal (coal metamorphism).[6] Figure 2 shows the phase diagram for carbon and the conditions under which graphite and diamond form.[7]

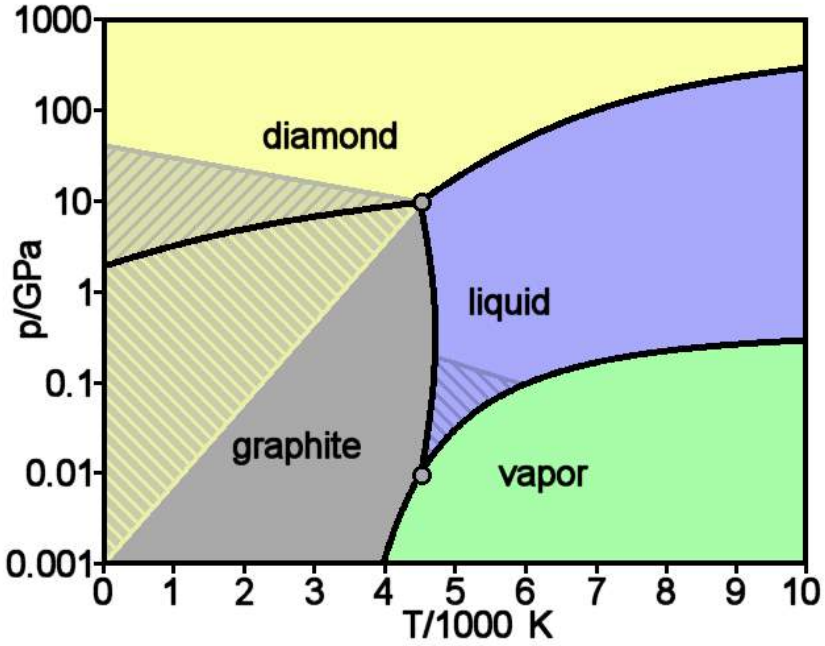

Figure 2. Phase diagram for carbon. Note that the pressures required to form diamond are much greater than for graphite. The hashed regions indicate conditions under which one phase is metastable; two phases can co-exist in these regions.[7]

The amorphous form of carbon occurs when a carbon-containing material, many times an organic polymer like those found in wood, is heated with insufficient oxygen to combust the whole sample. This is the reason why the Romans used clay domes when heating wood to form charcoal – to exclude excess oxygen. In the modern era, this method of transforming organic material into

carbon is called *pyrolysis* or *carbonization* and is typically performed under inert atmospheres (i.e. nitrogen or argon). During this process, most, but not all, of the heteroatoms are expelled from the structure under the heating, leaving behind a black, soft residue. The resulting structure is largely based on carbon-carbon bonds and is typically >90% carbon by mass.[8] Typical temperatures used for carbonization are in the range of 600°C to 3000°C with higher temperatures chosen to decrease the heteroatom content and increase the degree of order in the carbon lattice. Indeed, heating certain types of amorphous carbons at high temperatures approaching 3000°C produces carbons that are essentially graphitic and contain very few heteroatoms. The process of converting amorphous carbon to graphite is referred to as *graphitization*. These types of graphitizing carbons are called "soft" carbons and proceed through an intermediate liquid phase during carbonization. Examples of soft carbons are chars, soots, cokes, and coals. Conversely, materials such as cellulose and coconut shells remain entirely in the solid phase during carbonization. These materials produce carbons that do not develop any significant degree of crystallinity after heat treatment at 3000°C. Such carbons are designated as non-graphitizing carbons or "hard" carbons. Some examples of hard carbons include glassy carbons, carbon fibers, and carbon blacks.[8] In the case of glassy carbon, the interwoven, tangled 3D arrangement of the graphitic (graphene) sheets provide the resistance to graphitization.

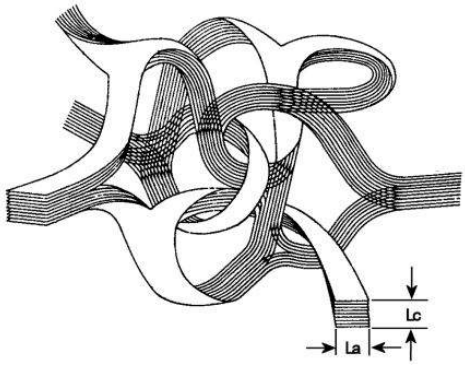

Figure 3 Drawing of the glassy carbon structure.[9] This material contains random orientations of the graphitic sheets. Their interwoven nature prevents conversion to graphite upon heat treatment at 3000°C.

As mentioned previously, the rearrangement of carbon atoms to form graphite generally requires heating at very high temperatures. However, adding certain inorganic and organic compounds can accomplish the same feat at lower temperatures. Many different additives have been used to induce graphitization including compounds of Co, Cu, and Fe.[8] This alternative approach is called catalytic graphitization and is discussed as part of Study 3.

2.1.2 Doping of amorphous carbon materials

Not only does the nature of the carbon-containing starting material, called the carbon precursor, have a dramatic impact on whether the carbon is hard or soft and the degree of graphitization, but also on the elemental composition. The percentage of heteroatoms can constitute a significant percentage of the material's structure, usually in the range of 1-12 wt%.[10] Purposeful

incorporation of heteroatoms into the carbonaceous structure, called *doping*, is an effective way of altering the carbon's properties. The main method for creating doped carbon materials is a bottom-up method involving the carbonization of organic precursors, which contain the desired heteroatoms. In this way, the bulk of the carbon is doped and also many of these dopants are present as surface functional groups, thereby modifying the material's surface properties. In the context of an application, the dopant can play just as important of a role as the carbon's structure.[11] For the syntheses involving doping, the temperature of carbonization must not be too high or else graphitization will occur to some extent, which lowers the heteroatom content. On the other hand, temperatures that are too low could result in incomplete carbonization (i.e. organic residues present in the carbon), which lowers the conductivity and structural strength of the carbon.

In a typical bottom-up synthesis involving doping, three main components are employed:

1. A carbonizable, organic molecule, called the carbon precursor, which supplies the bulk of the carbon in the final product.
2. Any additives needed for doping if the carbon precursor lack that element
3. A structure directing agent or template to give the final carbon a porous, high surface area structure.

Examples of structure directing agents and templates include mesoporous oxides, e.g. silica[12] and $CaCO_3$,[13] and eutectic salt mixtures such as $ZnCl_2$ with NaCl.[14] Carbonization of the carbon precursor mixture without such agents will yield bulk carbons with low surface area and porosity. A negative replica of the structure directing agent results from this method.

An important trait of the carbon precursor is non-volatility. In principle, any carbon-containing substance can serve as a carbon precursor. However, given the high temperatures involved for carbonization, if the rate of evaporation is higher than carbonization, very little material will remain. It is for this reason that a polymerizable carbon precursor is often employed in such syntheses. As a monomer, the precursor can easily infiltrate the pores of the template via fast diffusion. Then, by polymerizing the precursor within the pores prior to carbonization, the boiling point is greatly increased, thereby making carbonization more likely. One study also found that pre-polymerizing the precursor also resulted in better replication of the template compared to the unpolymerized control sample.[15]

In some syntheses, a solvent such as water or ethanol is employed if the carbon precursor and/or additives are solids at room temperature (e.g. glucose, urea);[13] in others, the carbon precursor is also the solvent (e.g. furfurylamine,[15] furfuryl mercaptan[16]). In either case, the elemental composition of the carbon precursor and additives dictates the doping of the final carbon product: using furfuryl mercaptan results in a sulfur-doped carbon, urea and glucose in aqueous solution a nitrogen-doped carbon, etc.

2.1.3 Doping with transition metal salts

The main challenge with doping with transition metals is how to incorporate them into the synthesis process. Most studies on doping of carbon deal with main group elements, principally nitrogen, [10, 14, 17-20] but also boron, [21-24] phosphorous, [25-26] and sulfur.[11, 27-28] For these elements, the organic carbon precursor contains that element covalently bonded within itself; for nitrogen doping, an amine or nitrile can be used; for phosphorous, a phosphine; for sulfur, a thiol or thiophene, etcetera. By contrast, simple, organic molecules containing transition metals are not so readily available. Some do exist and have been used for making transition metal-doped carbons such as metal-containing porphyrins,[29-33] phthalocyanines,[34-36] and phenanthroline complexes.[37-38] These complexes, however, are typically large, thereby preventing facile template pore impregnation. Furthermore, they tend to be expensive and, many times, must be synthesized using organic chemistry beforehand.

Another method of doping carbon materials is to simply dissolve the transition metal, typically as a salt, directly into the carbon precursor solution. The advantages of such a method are its simplicity and low cost. The carbon precursor solution usually also contains a coordinating atom, usually nitrogen, which forms coordinate covalent bonds to the transition metal cation in the solution. During the synthesis process, these metal-ligand bonds are incorporated into the final carbon structure, thereby forming a metal-centered *active site*. These are typically denoted as ML_x, where M is the transition metal and L is the ligand and x is the number of bonds between M and L. For example, an iron atom ligated by four nitrogen atoms is denoted as FeN_4.[15]

The major difference between doping with main group elements and doping with transition metal salts is that, in the case of salts, there are two parts: the metal cation and the counter anion. Most focus is on the metal cation and relatively little attention is paid to its anion, even though the counter anion plays an important role in determining the salt's properties including solubility, redox potential, and chemical reactivity. Importantly, for multivalent metal ions (ions with a charge of 2+ or greater) with a monovalent anion, doping will involve two or three times the number of anions as cations. For example, using $FeCl_2$ or $FeCl_3$ as an iron source, the number of chloride ions will be twice or three times higher than the iron cations.

Given the inherently polar nature of salts, most are soluble in only the most polar of solvents, namely water. As an example, sodium chloride (NaCl) is quite soluble in water (360 g L^{-1}), but has a very limited solubility in common organic solvents such as ethanol (0.65 g L^{-1}), acetonitrile (0.003 g L^{-1}), and acetone (0.00042 g L^{-1}).[39] Since many carbon precursor solutions typically use organic solvents, especially those where the carbon precursor is also the solvent (as is the case in this thesis), most salts will exhibit limited solubility. *It must be stressed that the final metal doping concentration (i.e. the metal loading) in the carbon material is ultimately limited by this solubility.* Therefore, to increase the metal loading, the solubility of the metal salt must be increased. The

idea of increasing the loading of the transition metal dopants is to simply provide more *active sites* to the surface of the carbon material. The term *active site*, in the context of this thesis, means one of two concepts (Figure 4):

1. A Lewis acidic site to which sulfur and polysulfides can bind (Studies 1 and 2).
2. A metal-centered site on which oxygen reduction reaction can take place (Study 3).

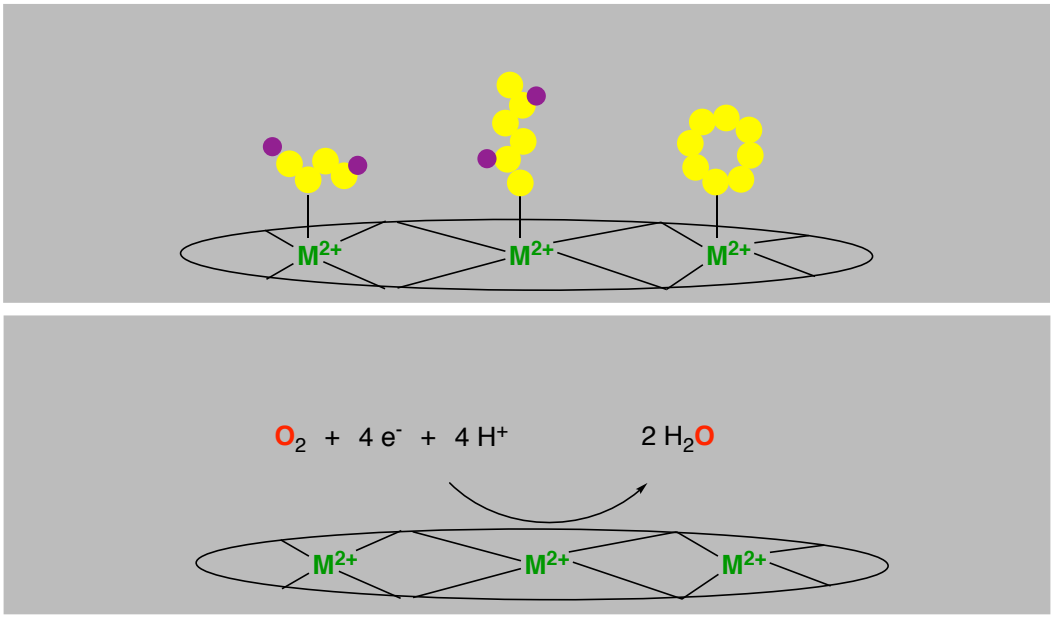

Figure 4. Illustration of metal-centered (M^{2+}) active sites in doped carbons: sites to which sulfur species can bind (top) or sites that can catalyze the oxygen reduction reaction (ORR, bottom).

While previous studies have demonstrated that adding too much dopant to the carbon can indeed disrupt the carbon lattice to point where extra dopant atoms actually hurt the performance,[10] most metal loadings are so low (0.5 to 1.0 wt%) that this was not a primary concern.[15] Instead, one of the initial goals of this work (Studies 1 and 2), was to simply increase the metal loading by using salts other than the standard chloride.

2.1.4 Selection of the dopant anion: weakly coordinating anions

An old "trick" from classical inorganic chemistry is to change the anion of a given metal salt to increase its solubility. Most soluble anions are not monoatomic like chloride, but instead spread the negative charge symmetrically over multiple electronegative atoms (e.g. O, N, F). This increases their polarizability, lowers their nucleophility (i.e. coordinating ability), and increases their chemical robustness.[40] In most cases, these anions are the conjugate bases of strong or super acids. Figure 5 details commonly used anions used to increase the solubility of the salt in organic media.

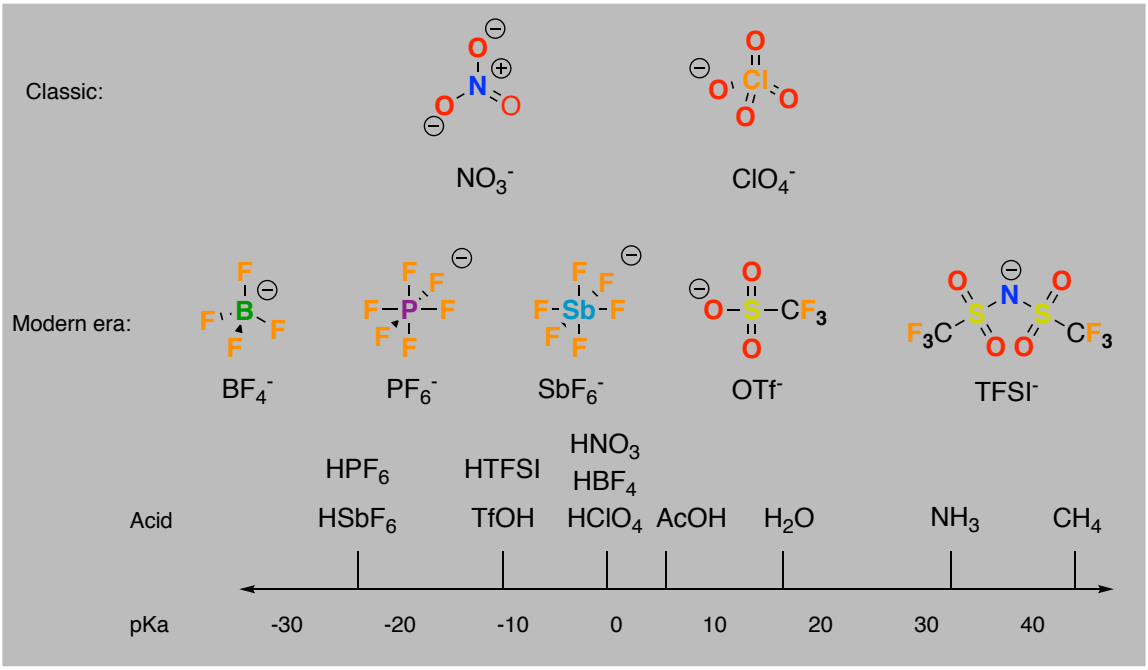

Figure 5. Structures of commonly used weakly coordinating anions. The approximate pKa of the conjugate acid is shown below the structures.

The "old school" anions used were nitrate (NO_3^-) and perchlorate (ClO_4^-), which are the conjugate bases of nitric acid and perchloric acid, respectively. These salts are commonly available for most metal cations and are typically much more soluble in organic solvents than the corresponding chloride. For example, the solubility of NaCl in acetone is 0.00052 g L^{-1} but $NaClO_4$ is 518 g L^{-1}.[41]

The main issue associated with nitrate and perchlorate salts is their tendency to act as oxidizers and, in some circumstances, as explosives. To combat this feature, other anions were synthesized that lacked an explosive nature and were even more soluble than perchlorates. Most of the common weakly coordinating anions used today are tetrafluoroborate (BF_4^-), trifluoromethanesulfonate (triflate, OTf^-), hexafluorophosphate (PF_6^-), and hexafluoroantimonate (SbF_6^-). These were among the first anions to be evaluated for the salts used in Studies 1 and 2.

2.1.5 Selection of the dopant cation: Hard-soft acid base theory (HSAB)

The metal chosen to dope the OMCs is of the utmost importance. The nature of this selection determines many of the OMCs properties including catalytic activity, Lewis acidity, redox potential, and chemical reactivity. For most transition metals, they are available commercially as the salt of at least one weakly coordinating anion. Sometimes multiple salts are available. The principal question to ask is *which metal is the best for the chosen application*. For fuel cells where catalytic O_2 reduction is the key step, many studies have shown that Fe and Co are the most apt;[36, 42-43] hence, four Fe salts were chosen for Study 3, including three soluble ones.

In the context of Li-S batteries, however, the choice of metal is slightly more complex. As stated at the beginning of this section, the goal of doping the OMC with transition metal ions was to add Lewis acidic sites to the carbon skeleton. It is to these sites that the sulfur species, particularly the lithium polysulfides (LiPS), will bind and be better retained within the cathode of the battery. The interaction between the metal center and the LiPSs should be as strong as possible.

To answer this question, we invoked the concept of Hard-Soft Acid Base Theory (HSAB).[44] HSAB is routinely employed in inorganic and organometallic chemistry to explain the stability of certain Lewis acid-base adducts (e.g. metal complexes) over others and preferences in bonding arrangements. A Lewis acid-base adduct results from electron pair donation from a base into an empty, low energy orbital of an acid, forming a covalent bond (Figure 6). Table 1 shows the characteristics and examples of hard and soft acids and bases.

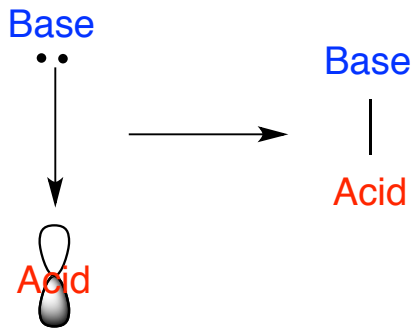

Figure 6. Reaction involving a Lewis acid with an empty orbital and a Lewis base with at least one lone pair of electrons. The stability of the product of the reaction, typically called an adduct, is explained using HSAB.

Table 1: Characteristics and examples of hard and soft acids and bases

Characteristic	**Hard**	**Soft**
Atomic radius	Small	Large
Oxidation state	High	Low or neutral
Polarizability	Low	High
Nature of bonding	Ionic	Covalent
Examples of acids	H^+, Li^+, Al^{3+}, Ti^{4+}, BF_3	Pt^{2+}, Hg^{2+}, Au^+, BH_3
Examples of bases	OH^-, F^-, Cl^-, CO_3^{2-}	H^-, PPh_3, SCN^-, I^-, R-SH

There are some general periodic trends for both Lewis acids and bases in terms of their hard-soft character. Lewis bases, by definition, must have at least one free electron pair for bonding and, as such, typically come from more electronegative elements in the Periodic Table (i.e. the p-block). As one moves down the p-block, the outer most electrons are more shielded from the nucleus and are more prone to be attracted or repelled by other charges or molecules. This increase in polarizability makes these bases softer; thus I^- is the softest halide bases whereas F^- is the hardest. Figure 7 shows the general hard-soft character of these elements.

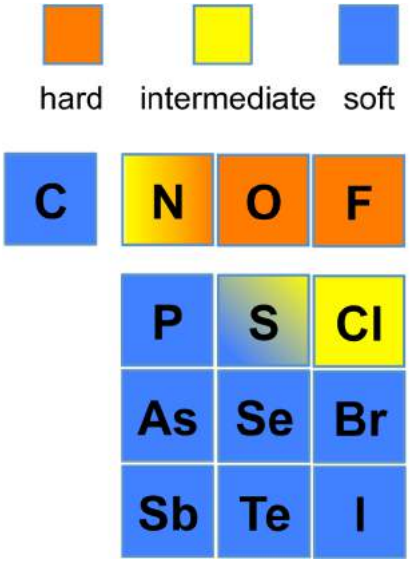

Figure 7. General trend in Lewis basicity for the p-block elements.

As shown in this figure, sulfur, as a base, is of intermediate, bordering on soft character. Another general trend in hard-soft character is with oxidation state: the more oxidized a given atom is the harder it is, the more reduced, the softer. Therefore, sulfur as reduced PS, will exhibit a strongly soft character. *To maximize the interaction with PS, a soft Lewis acid should be selected.*

Lewis acids typically hail from more electropositive elements in the Periodic Table (i.e. the s- and d-blocks), although oxidized p-block elements can be Lewis acids as well (e.g. Si^{4+}, Pb^{2+}, BF_3, I_2). Figure 8 shows the overall hard-soft character of these acids.

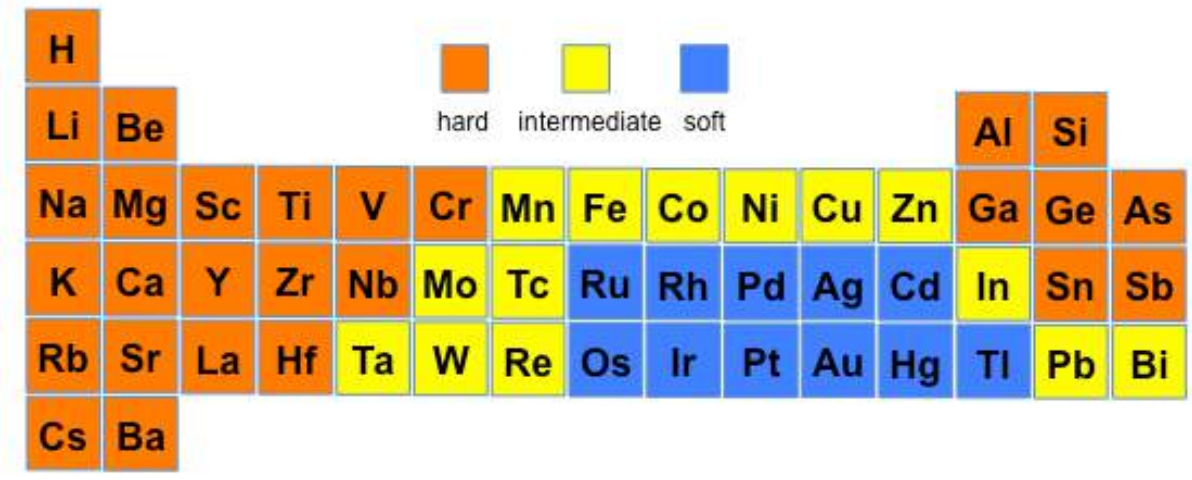

Figure 8. General trends in Lewis acidity for the s-, d-, and some p-block elements.

The general trend is that alkali and alkali earth cations are very hard as are the early transition metals. The softer Lewis acids come from the later transition metals, particularly from the second

and third row. In selecting a Lewis acid with which to couple the soft sulfur and PSs, a mid or late transition metal seems to fit the bill. Iron, the element used to dope the OMCs for PEMFCs, seems to be also applicable for Li-S batteries given its intermediate softness. However, the oxidation state of Fe plays an important role. The two common oxidation states of Fe, 3+ and 2+, are usually designated as a hard and intermediate acid, respectively. A softer metal center would likely serve better. Metal centers such as Au^{+}, Pt^{2+}, Pd^{2+}, and Hg_2^{2+}, are among the softest available and show exceptionally strong interactions with sulfur; indeed, an older name for an organic thiol group (R-SH) is *mercapto*, which is short for *mercury capturing*, due to its marked affinity for mercury. For these metal ions, though, their toxicity and/or cost prohibit their use. Alternatives to these are late, first row transition metals in low oxidation states including Co^{2+}, Ni^{2+}, Cu^{2+}, and Zn^{2+}, which are usually regarded as intermediate acids. Copper represents an interesting case since its common oxidation states are 1+ and 2+. Cu^{+} is normally designated as a soft acid. Thus, copper was initially chosen as the dopant and the results of using salts of copper with weakly coordinating anions is detailed in Studies 1 and 2.

2.2 Grafting of functional groups to carbon surfaces

Another method to expand the utility of materials, carbon included, is to covalently bond small organic molecules to their surface. This process is usually referred to as grafting. While grafting can be confused with doping since many of the grafted functional groups contain one or more types of heteroatoms, in the context of this thesis, doping refers exclusively to the bottom-up, templated process using heteroatom-containing precursors, which was detailed in Section 2.1.2. In contrast to doping, grafting takes a preformed material and subjects it to reactive species in either the solution or gas phase to form covalent bonds with the surface. The key distinction between the two methods is that doping changes the elemental composition of *both* the bulk material and the surface while grafting affects *only* the surface of the material, leaving the bulk material unchanged.

Grafting has been used extensively for other materials: for gold, thiols are employed to attach organic groups to the surface; for TiO_2, carboxylic and phosphonic acids can add additional functionality by forming titanol esters; for silica, silanes are routinely used to graft organic functional groups to surface silanols. In the case of carbon materials, the relatively unreactive surface means that more forceful conditions are required. One common method is oxidation with O_2, O_3, HNO_3, H_2SO_4, or H_2O_2, which forms carboxylic acids, alcohols, and ketones and other oxygen-containing functional groups.[45-48] In a second step, organic chemistry reactions can couple small molecules to these functional groups. Examples include esterifications,[49] amidations,[50] S_N2 reactions with alkyl chlorides/bromides,[51] or silinations with organic silanes.[52-54] However, the first step involves relatively harsh conditions to oxidize the carbon surface. If such conditions are not chosen carefully, prolonged exposure to the oxidant can result in destruction of the carbon framework and loss of porosity and electrical conductivity.[55] Moreover, with gas phase oxidants

like O_2 and O_3, too high of temperature and/or too long of exposure can result in complete combustion of the carbon material.

One of the more common grafting techniques is attachment via diazonium chemistry. Using this method, an aniline derivative is treated with isoamyl nitrite,[56] sodium nitrite,[57] or nitrosonium hexafluorophosphate[58] usually under acidic conditions to form the diazonium salt *in situ*, which then reacts with the carbon surface while liberating N_2. In other cases, the carbon is treated with a previously synthesized diazonium salt, which is then reduced at the carbonaceous electrode to functionalize the surface.[59] This approach has the advantage of avoiding the deterioration of the carbon skeleton associated with surface oxidation. However, the diazonium species is highly reactive and can react with an already grafted molecule on the surface, thereby forming multilayer coverages, resulting in pore clogging, reduced surface area, and easily detached surface groups.[58] Additionally, diazonium salts are hard to synthesize and isolate and are not compatible with many functional groups.

The focus of Study 4 is to introduce a new type of grafting reaction to the field of carbon materials – the bromomethylation reaction. This reaction is reproducible, highly selective, and yields high surface coverages in a strictly monolayer fashion. Furthermore, the bromomethyl groups grafted onto the carbon surfaces serve as a versatile attachment point for a wide variety of organic functional groups in subsequent functionalization reactions (S_N2). We believe that this novel reaction will find great utility within the carbon community.

2.3 Lithium-sulfur batteries

One field in which carbon materials have found great utility is lithium-sulfur (Li-S) batteries, where the carbon constitutes the conductive additive for the sulfur side of the battery. A battery is based on electrochemistry, or spontaneous electron transfer between an electron donor (D) and electron acceptor (A). Spontaneous, in this context, signifies that electron transfer will occur between the donor and acceptor if a viable pathway is available (i.e. the change in Gibbs Free Energy, ΔG, is negative). One such pathway results from putting the two in close proximity to each other; in other words, if the donor and acceptor are simply mixed together physically, sometimes with the aid of a liquid solvent, the spontaneous electron transfer occurs from the donor to the acceptor and the energy released manifests itself in the form of heat (left diagram in Figure 9). For the modern era, however, heat is not the desired form of energy, but rather electricity. The design of a battery is to allow the electron transfer to happen, but to force it to produce electricity; in this case, the viable electron transfer pathway is not direct physical contact between the donor and acceptor, but rather connecting them with an external electronic conductor (i.e. a metal wire). In this configuration, the negative charge carriers, the electrons, are allowed to flow through the conductor whereas the positive charge carriers, the ions, must travel a different path through the intervening electrolyte. No cations can travel through the wire just like no electrons can travel through the electrolyte. The separation of pathways for the negative and positive

charges causes the production of electricity. After travelling their separate paths, the two types of charges recombine on the electron acceptor side of the cell. Using this configuration, some energy is still released as heat, but a sizeable portion is converted into the desired form of electricity (right diagram, Figure 9).

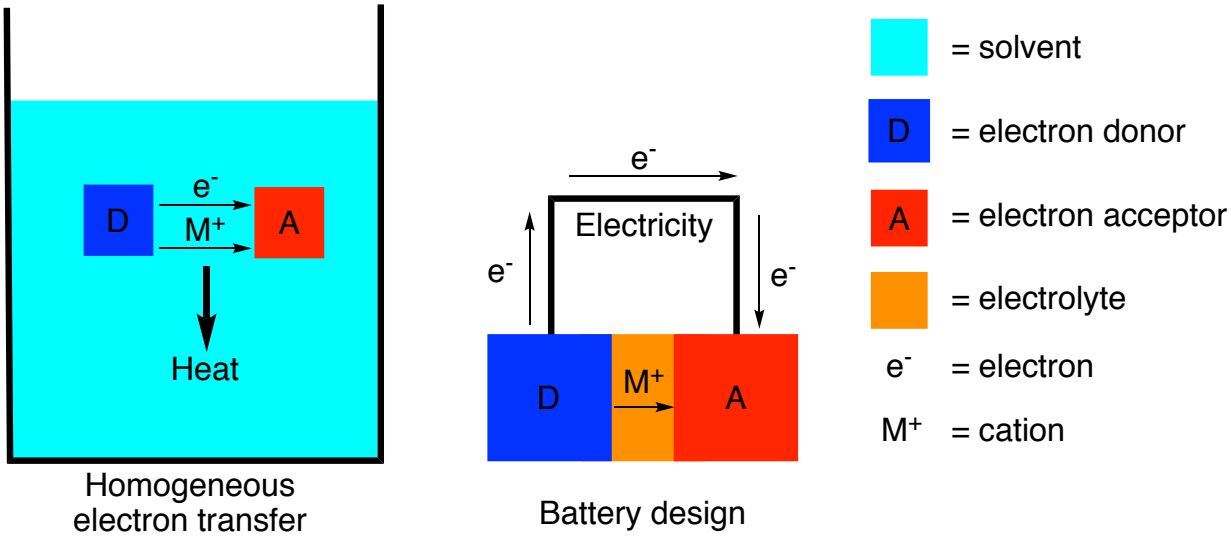

Figure 9. Comparison of homogeneous electron transfer (left) vs. battery design (right) between the donor (D) and acceptor (A). In homogenous electron transfer, both the electrons (e^-) and cations (M^+) travel the same path and the energy change, ΔG, is released as heat. In contrast, in the battery architecture, the electrons and cations take different paths and most of the energy is captured as electricity.

In the context of a battery, the electron donor is called the anode and the electron acceptor the cathode. The two halves of the cell are separated by the electrolyte. The circuit is completed by electronically connecting the anode and cathode with a wire. The first battery was invented by Volta in Italy in 1800 by piling zinc and silver disks together separated by a cloth soaked in a sodium chloride solution.[60] These constituted the anode, cathode, and electrolyte, respectively. Today, the basic battery concept is still the same, although with different materials for each component. Among the currently used technologies are lead acid, nickel metal hydride, and lithium-ion (Table 2). Lead acid batteries, invented in 1859, constitute the majority of the batteries today (> 80%) due to their low-cost, well-defined electrochemistry, relatively high voltage (2 V) and high recycle rate.[61] This wide-spread usage comes in spite of their modest capacities and heavy weight of their components. Nickel metal hydride (Ni-MH) batteries first appeared in Japan in 1990 as an alternative for nickel-cadmium and have found use as small, rechargeable cells.[62] Lithium-ion (Li-ion) batteries were patented in 1990 and have revolutionized the portable electronic devices market due to their high voltage and energy densities, low weight, and small size.[62]

However, even at their full theoretical capacity, lithium-ion batteries exhibit an energy storage capability that is too low to meet the demands of several major markets including transportation

and electrical grid storage. Going beyond lithium-ion batteries requires exploring anode and cathode materials with different electrochemistries. Lithium and oxygen, as the anode and cathode respectively, would seem to fit the bill. As oxygen is "free" and doesn't contribute any significant weight, the Li-O_2 cell has its capacity based on Li alone. As shown in Table 2, the theoretical energy density of this cell is around 11586 Wh kg^{-1}, which is close to the energy density of gasoline (approximately 13,000 Wh kg^{-1}). However, many severe problems plague this cell, which limit its prospects for the future.[63] An alternative system is the Li-S cell, in which the eponymous elements serve as the anode and cathode, respectively. The electrolyte consists of lithium salts dissolved in organic solvents; lithium cations (Li^+) serve as the positive charge carriers in this type of cell. The Li-S battery touts a theoretical energy capacity almost seven times higher than lithium-ion cells and has inspired much research interest in the past few decades.[64]

Table 2. Comparison of battery technologies

Technology	Capacity (mAh g^{-1})	Nominal voltage	Energy density (Wh kg^{-1})
Lead acid ref [62]	65	2.0	170
Ni-MH, ref [61]	206	1.35	278
Li ion*, ref [61, 65]	200	3.4-3.8	720
Li-S‡, ref [64]	1675	2.15	2500
Li-O_2§, ref [62-63]	3862	3.10	11586

*Based on $C_6Li + CoO_2 \leftrightarrow 6C + LiCoO_2$

‡Based on $16Li + S_8 \leftrightarrow 8Li_2S$

§Based on $2Li + O_2 \leftrightarrow Li_2O_2$ (non-aqueous, mass of Li only)

Besides its higher capacity and energy density, sulfur has other distinct advantages including cost, abundance, and non-toxicity. However, many problems occur in this system, the majority of which stem from the insulating nature of S. Whereas elemental Li is a conductor, S is an excellent insulator (Table 3). To overcome this issue, conductive additives are used to "wire up" the S, thereby making it electrochemically accessible during battery cycling. This is where the aforementioned carbon materials come into the Li-S system (Figure 10). The addition of such electro-inactive materials, however, comes at a cost. In most of the cathodes described in the literature, the weight percent of sulfur is typically below 60%, thereby lowering the overall electrode capacity. Even with the conductive additives, due to the insulating nature of S and its discharge products lithium disulfide (Li_2S_2) and lithium sulfide (Li_2S), most Li-S cells suffer from poor sulfur utilization; in many cases, the percent of sulfur used electrochemically is well below 70% during the first cycle and usually decreases with repeated cycling.

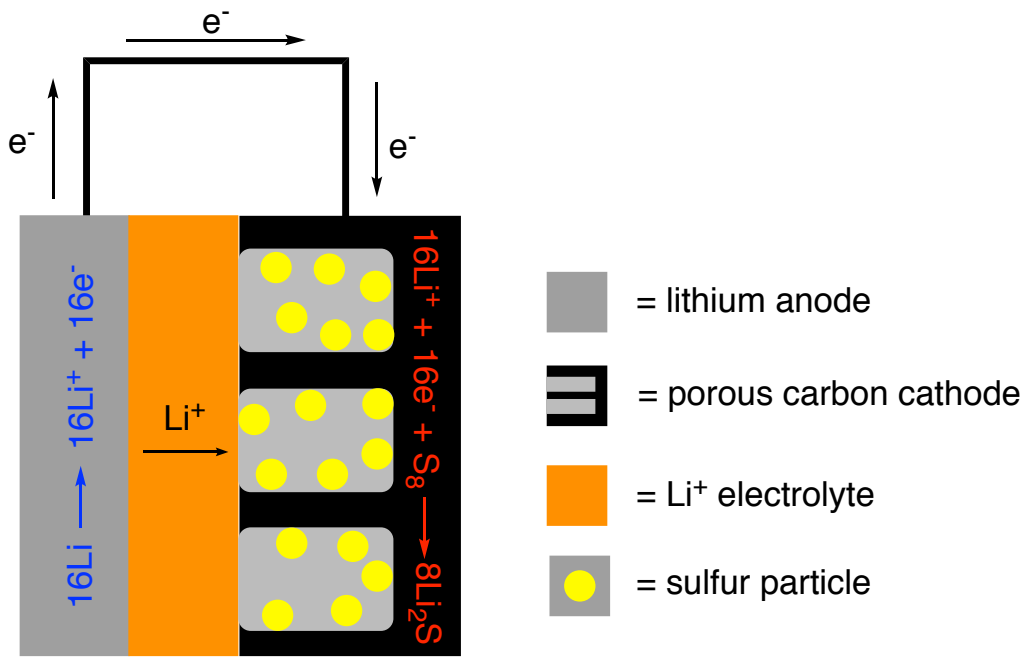

Figure 10. Illustration of a Li-S battery. One of the key components is the porous carbon, used as an additive to make the sulfur conductive.

Table 3. Resistivities of some common elements.[66]

Material	Resistivity (Ω m)
Lithium	9.28×10^{-8}
Sulfur (S_8)	1.00×10^{15}
Copper	1.68×10^{-8}
Silicon	6.40×10^{2}
Carbon (amorphous)	$5.00 – 8.00 \times 10^{-4}$
Carbon (graphite)	$2.50 – 5.00 \times 10^{-6}$ (II basal plane) 3.00×10^{-3} (⊥ basal plane)

The dilution with carbon and underutilization of S are not the only problems associated with the Li-S cell. The redox system that reversibly converts elemental lithium and sulfur to Li_2S, while seemingly simple, is actually quite complex (Figure 11). This process occurs through partially reduced sulfur species called lithium polysulfides (LiPS), which have the structure Li_2S_n, where $3 \leq n \leq 8$. These LiPS are poorly characterized structurally and exist in rapid equilibrium in solution.[67] As the cell is discharged, the average LiPS chain length is reduced (n decreases) until solid Li_2S_2 and Li_2S is produced. In most of the conventional electrolytes, the starting and ending products are only sparingly soluble, but the LiPS demonstrate a much higher solubility. While a high solubility allows for better sulfur utilization, it also permits the sulfur to diffuse away from the electrode. The LiPS can diffuse to the lithium anode and react directly on the metal surface.

This results in low Coulombic efficiency, high self-discharge rates, and loss of active material. The repeated dissolution-precipitation of sulfur species is accompanied by a large volumetric change; upon complete discharge from S to Li_2S, the volume increases by 80%. If sufficient space is not available, this expansion and contraction can break the carbon framework of the cathode, causing catastrophic battery failure.

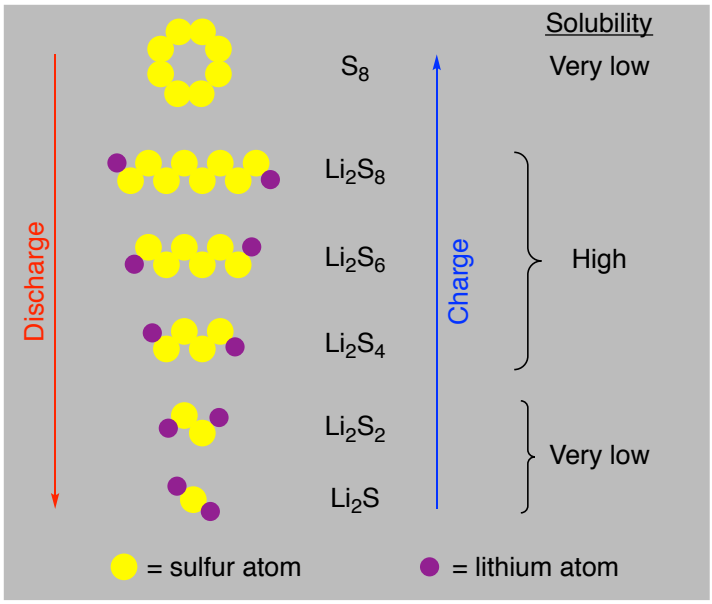

Figure 11. Illustration of the interconversion of sulfur (S_8) to Li_2S during battery cycling. The complex electrochemistry is compounded with the drastic changes in solubilities, resulting in poor performing Li-S batteries despite their high theoretical capacities.

A large portion of research in the Li-S field focuses on how to curtail some or all of these deleterious features of sulfur. Many strategies revolve around using porous carbons to house the sulfur and the LiPS. In many cases, these carbons are doped in the hope of better retaining the LiPS within the cathode.[10, 17, 20, 23-24] In other instances, grafting of small molecules to a porous carbon surface has been employed in an attempt to stabilize the sulfur discharge products.[57] These were the goals of Study 2 and Study 4, respectively.

2.4 Proton exchange membrane fuel cells

Another field in which carbon materials have found extensive use is fuel cells. A fuel cell shares many characteristics with a battery. A fuel cell also contains an anode and cathode, separated by an ionically conducting electrolyte. However, unlike most batteries where the amount redox active material is fixed (i.e. no material leaves or enters the cell), in a fuel cell, the electroactive materials, the fuels, are pumped in on either side and the discharge products, the exhaust, are removed. The electrons and cations are separated from each other on the anode side and the electrons travel the external circuit while the cations traverse the electrolyte. The charges

recombine on the cathode side where they form the discharge product. This produces electricity, which can be drawn from the cell.

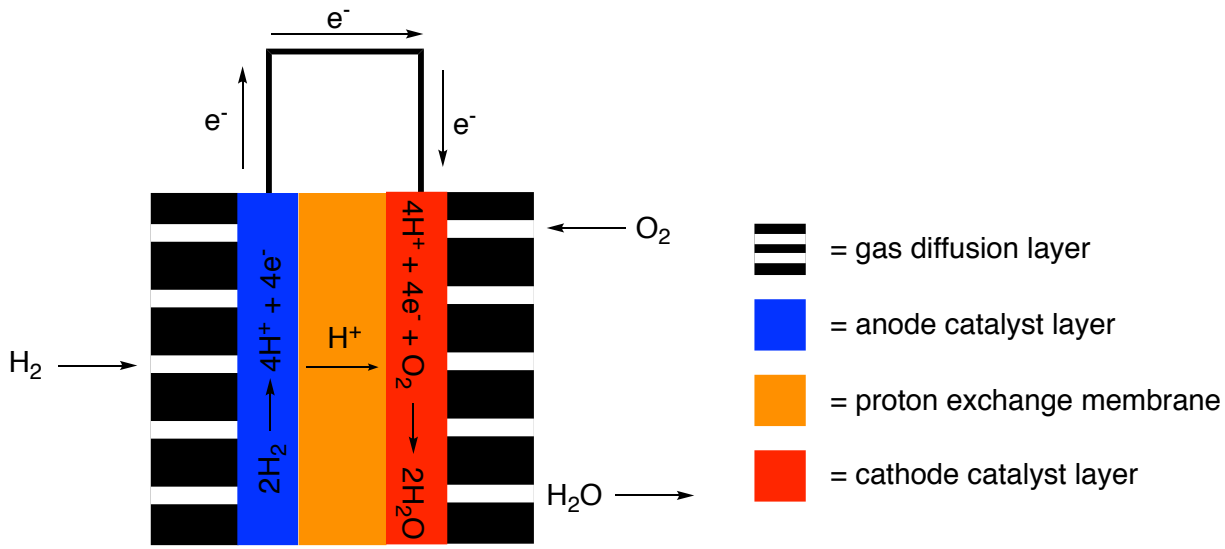

Figure 12. Illustration of a proton exchange membrane fuel cell (PEMFC).

The type of fuel cell employed in this thesis is the most common type of fuel cell, the PEMFC. PEMFC can stand for either polymer electrolyte membrane fuel cell or proton exchange membrane fuel cell. The fuel for this type of cell can be hydrogen, methanol, ethanol, formic acid, or dimethyl ether on the anode side and oxygen is the most common oxidant on the cathode side. The PEMFC utilizing hydrogen (H_2) as the fuel is the most commonly encountered type of cell. On the anode side, H_2 is the electron donor and is split into electrons and protons (Equation 1). The electrolyte, as the two PEMFC names imply, consists of an acidic, water-based polymeric membrane; protons (H^+) are the positive charge carriers in this cell, similar to Li^+ in the Li-S system. The H^+ diffuse through the polymer electrolyte membrane while the electrons travel the external circuit. On the cathode side, dioxygen (O_2) acts as the electron acceptor and, together with protons from the electrolyte, forms two molecules of water (Equation 2). The overall reaction is shown in Equation 3.

$$2H_2 \rightarrow 4H^+ + 4e^- \quad (1)$$

$$4H^+ + 4e^- + O_2 \rightarrow 2H_2O \quad (2)$$

$$2H_2 + O_2 \rightarrow 2H_2O \quad (3)$$

The anode reaction is referred to as the hydrogen oxidation reaction (HOR) and the cathode reaction is referred to as the oxygen reduction reaction (ORR). It must be stressed that the overall PEMFC reaction is no different than the direction combustion of H_2 in the presence of O_2.

However, since a PEMFC directly converts the chemical energy into electrical energy, the efficiency is much higher. By comparison, a combustion engine first converts the chemical energy to thermal energy, then to mechanical energy, then finally to electrical energy. With each step, energy is lost in the form of heat. Under ideal conditions, a fuel cell fed by pure H_2 and O_2 could reach an ideal efficiency of 83% (Equation 4).[68]

$$\eta_{ideal} = \frac{\Delta G_{ideal}}{\Delta H_{ideal}} = \frac{-237.2\ {}^{kJ}/_{mol}}{-285.9\ {}^{kJ}/_{mol}} = 0.83 = 83\% \quad (4)$$

Calculations have shown that a real fuel cell could reach efficiencies of up to 54%, with real life fuel cells having performances reaching 36%. This can be compared to an electric car, for which electricity has been produced from natural gas, where the overall conversion efficiency is about 24%.[69-70] Overall, the efficiency of any fuel cell can be calculated from its operating voltage (E_{cell}) as compared to its ideal voltage (E_{ideal}, Equation 5):

$$\eta = \frac{\Delta G_{cell}}{\Delta H_{ideal}} = \frac{-nFE_{cell}}{\Delta G_{ideal}/_{0.83}} = \frac{-0.83nFE_{cell}}{-nFE_{ideal}} = \frac{0.83E_{cell}}{E_{ideal}} \quad (5)$$

η = efficiency (unitless)
ΔG = change in Gibbs free energy (kJ mol^{-1})
ΔH = change in enthalpy (kJ mol^{-1})
n = number of electrons transferred (mol)
F = Faraday constant (96485 C mol^{-1})
E_{cell} = actual cell voltage during operation (V)
E_{ideal} = thermodynamic cell voltage (V)

In the case of both the HOR and ORR, the reaction does not proceed perfectly. While the theoretical or thermodynamic voltage (E_{ideal}) is 1.23 V, in practice, the cell voltage (E_{cell}) is measurably less (typically 0.50-0.85 V). This loss in voltage exists because some of it is needed to drive both reactions to occur at a reasonable rate; indeed, as the reaction proceeds more quickly (i.e. more current is drawn from the cell), the voltage drop is greater (Figure 13). To attenuate this loss, catalysts are employed in both the anode and cathode. Platinum is the typical catalyst used for both reactions, but its cost and scarcity point to a need to develop cheaper, more abundant catalysts. Of the two reactions, the HOR is simpler since fewer bonds are broken and formed and only very small amounts of Pt are needed for efficient catalysis. Figure 14 shows that the voltage losses, or polarizations, are minimal from the HOR.

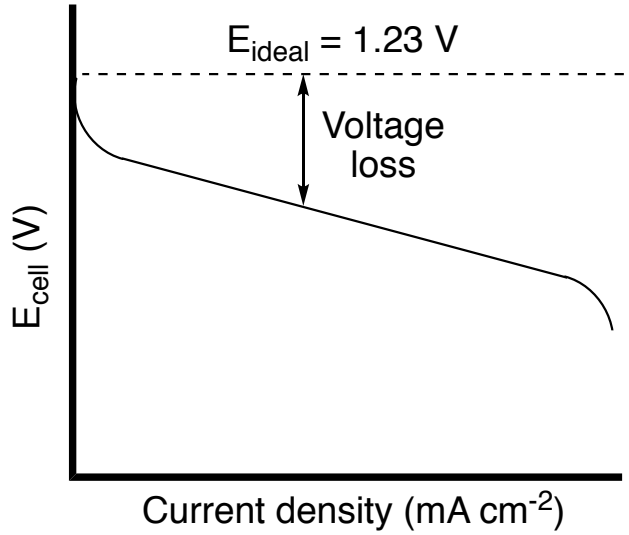

Figure 13. Illustration of ideal and actual fuel cell voltage and current characteristics. As more current is drawn from the cell, the voltage loss is greater.

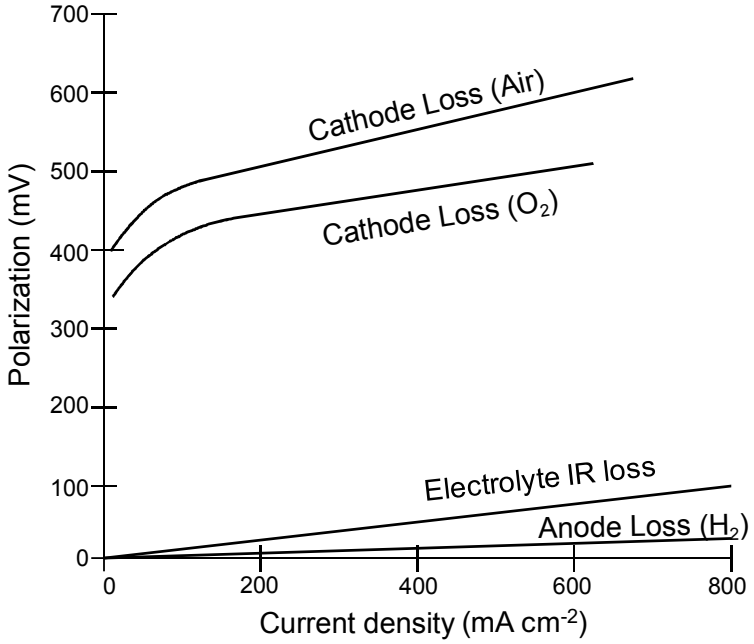

Figure 14. Contributions to the voltage loss (polarization) in a PEMFC. The majority of this loss comes from the cathode and the ORR, with smaller contributions from the electrolyte IR drop and HOR anode reaction.[69]

In the case of the ORR, the polarization is significantly higher and is the major contributor to the voltage losses in a PEMFC. Thus, a significant amount of research in this field focuses on how to minimize the voltage loss on the cathode side by catalyzing the ORR. Carbon materials, with their variable compositions, high surface area, and porous structures are well suited for this task. In a landmark study, it was found that nitrogen-doped carbon nanotubes efficiently catalyze the ORR.[71] The advantage of these carbons stems from that their synthesis uses strictly Earth-abundant elements. Additionally, various studies have found that co-doping carbons with both

nitrogen and transitions metals (e.g. Fe, Co) could also enhance their activity towards the ORR.[38, 72] The goal of Study 3 was to increase the Fe content, and, in turn the catalytic activity of ordered mesoporous carbons, by using more soluble iron salts.

3 Experimental methods

The experimental characterization of the synthesized or surface-modified carbons can be divided into four main categories: structural, elemental, thermal, and electrochemical.

1. Structural: nitrogen-sorption (N_2-sorption), X-ray diffraction (XRD), small angle X-ray scattering (SAXS), and transmission electron microscopy (TEM).
2. Elemental: X-ray photoelectron spectroscopy (XPS), X-ray fluorescence (XRF), and elemental or combustion analysis (EA).
3. Thermal: thermogravimetric analysis (TGA) and differential scanning calorimetry (DSC).
4. Electrochemical: rotating disk electrode (RDE), Li-S battery testing, and PEMFC single cell tests.

The Li-S battery testing and PEM fuel cell tests are also applications and represent the end goal of these studies. Their sample preparation methods are also considerably more involved and complex. As such, the Li-S battery fabrication methods are discussed in its own section (Section 4). The PEMFC single cell tests were conducted by a colleague (Caroline Janson) and the preparation and testing details are discussed in her licentiate thesis and are also described in detail in Study 3.

3.1 Structural characterization

3.1.1 Nitrogen-sorption

Nitrogen-sorption (N_2-sorption), short for nitrogen adsorption-desorption, is a technique used to study the surfaces of solid materials. It can reveal useful information about surface properties of a powder including surface area, pore volume, and pore diameter distributions. Nitrogen adsorption on solid surfaces and in pore spaces is a complex phenomenon involving energy interactions and phase changes. In a typical experiment, the powder is rigorously dried, placed in a tube of known volume, and attached to the instrument. The sample is cooled in a liquid nitrogen bath and small aliquots of nitrogen gas are administered by the instrument. Since the surface atoms of the solid have a bonding deficiency, it becomes energetically favorable at these low temperatures to interact with the nitrogen molecules, i.e. physisorption. At low pressures, well below the saturation pressure (P_0), the nitrogen molecules adsorb to the most energetic sites on the surface, eventually forming a monolayer. At this stage, the BET calculation is performed (Equation 6) to determine the surface area of the material; the more nitrogen adsorbed at this stage, the higher the surface area (Equation 7).

$$\frac{p}{V(p_0 - p)} = \frac{1}{V_m C} + \frac{C - 1}{V_m C}\left(\frac{p}{p_0}\right) \tag{6}$$

$$S = \frac{V_m \sigma N_A}{m V_0} \quad (7)$$

p = partial pressure of nitrogen (mmHg)
p_0 = saturation pressure of nitrogen (mmHg)
V = volume of nitrogen adsorbed (cm^3 at STP)
V_m = amount of nitrogen in a monolayer (cm^3 at STP)
C = constant showing the interaction between nitrogen and the surface (unitless)
S = specific surface area ($m^2\ g^{-1}$)
σ = molecular area of nitrogen (16.2 $Å^2$ per molecule)
N_A = Avogadro's number (6.023×10^{23} molecules per mol)
m = sample mass (g)

Using the above equations, a plot of $P/(V(p_0 - p))$ vs. p/p_0 should yield a straight line with intercept $1/V_mC$ and slope of $(C-1)/V_mC$. From the line of regression, the value of C and V_m can be obtained. Subsequently, Equation 7 can be utilized to determine the surface area of the material normalized by mass.

As more nitrogen is administered to the sample, multilayers begin to form. Inside the pore volume, as the multilayers come into close proximity to each other, the additional gas molecules are now bonded on multiple sides and condensation becomes very favorable. Called capillary condensation, this results in a large quantity of gas to adsorb over a short range of pressures. At this point, the BJH calculation is performed to determine the pore volume and pore size distributions of the material. The pressure is increased further to nearly the saturation pressure, at which point the pressure is reduced and the desorption isotherm is measured. For porous materials, it is common to observe a hysteresis; the pressure must be lowered below the pressure at which the capillary condensation occurred during the adsorption isotherm.

N_2-sorption analyses were conducted on a TriStar 3000 Instrument.

3.1.2 X-ray diffraction

X-ray diffraction (XRD) is a technique used to probe the atomic scale of a crystalline solid. The sample is irradiated with monochromatic X-rays with wavelengths similar to interatomic spacings (e.g. for Cu K_α X-rays, λ = 1.54 Å), which interact with the sample and form a diffraction pattern. Typically, the sample is a fine powder so all possible crystal orientations relative to the X-rays are possible. This collapses the diffraction pattern to one dimension: the angle between the incoming and diffracted X-rays (i.e. 2θ). By contrast, for single crystal X-ray diffraction, the two angles between the crystal and the X-rays are considered, which yields more structural information at the cost of more complicated instrumentation and sample preparation.

The angle between the sample and the X-rays is scanned and the intensity of the reflected radiation is measured. Diffraction occurs when some of the crystallites in the sample meet the requirements of Bragg's Law (Equation 8).

$$2dsin\theta = n\lambda \tag{8}$$

n = integer (diffraction order)
d = interatomic spacing (Å)
θ = angle between sample and the incident X-rays (°)
λ = wavelength of the X-rays (Å)

Structural information about the sample is contained in the angle at which diffraction occurs (unit cell parameters, symmetry), the intensity of the reflection (atomic positions within the lattice, relative concentrations for impure samples), and shape of the peak or full width at half maximum (crystallite size and defect concentrations).

The XRD measurements conducted for this thesis were carried out on finely ground powder samples using a Bruker XRD D8 Advance instrument operated in the Bragg-Brentano geometry using Cu K_α radiation.

3.1.3 Small angle X-ray scattering

Small angle X-ray scattering (SAXS) is closely related to other X-ray techniques, particularly XRD, but whereas XRD probes atomic scale periodicity (i.e. atomic lattices at the Ångström scale), SAXS studies periodicity on a larger scale, called the mesoscale, which is typically from 1 to 100 nm. The corresponding 2θ angles are thus much smaller; as shown in Equation 8, if d is much larger, then θ, or $\sin(\theta)$, must be much smaller to equal the same value of $n\lambda$. Typical 2θ values for SAXS are 1° to 5° while for XRD 10° to 80° is the common range. SAXS can reveal information about mesoporosity, micelles in solution, and alignment of nanofibers among others. A requirement for SAXS is a scattering contrast due to the electron density between the particles and the matrix. This can be, for example, pore walls made of SiO_2 or carbon and the pore volume filled with air. As with XRD, the diffraction peaks can be indexed using the Bragg equation, but in SAXS these peaks represent long-range order on the mesoscale.

SAXS measurements were performed on a Mat:Nordic SAXS/WAXS/GISAXS instrument from SAXSLAB using a Cu K_α radiation source.

3.1.4 Transmission electron microscopy

Transmission electron microscopy is a powerful tool for studying the fine structure of materials. In many ways, TEM is analogous to conventional light microscopy: there is an illumination source,

a condenser system to control illumination of the sample, the sample, then finally an objective lens that forms the image after the light/electrons interact with the sample.

The major difference between TEM and an optical microscope is the illumination source: whereas optical microscopes use visible light (λ = 400 – 700 nm), TEMs utilize high energy electrons with accelerating voltages of 100 – 200 keV. For an accelerating voltage of 200 keV, the corresponding λ is 0.0025 nm, signifying that much smaller objects can be resolved. In practice, however, the imperfections of the magnetic lenses limit this resolution to the Ångström or nanometer scale, depending on the design of the microscope.

In this work, all TEM images were taken using an FEI Tecnai T20 microscope with a LaB_6 filament with an accelerating voltage of 200 keV.

3.2 Elemental characterization

3.2.1 X-ray photoelectron spectroscopy

X-ray photoelectron spectroscopy (XPS) is a characterization tool for the study of the elemental composition, oxidation state, and electronic structure of a material. Under high vacuum, the sample is irradiated with X-rays of a known energy and electrons are ejected, called photoelectrons. Based on the energy of these electrons, a binding energy can be measured, using Equation 9.

$$E_b = h\nu - E_k \tag{9}$$

E_b = electron binding energy
$h\nu$ = energy of incident X-rays
E_k = kinetic energy of photoelectrons

The binding energy is unique to a given element and can be used to determine the elemental composition at the surface. Small variations in this binding energy reveal the oxidation state of the element. For example, the approximate binding energy of carbon in C-C bonds is 283 eV whereas in C=O bonds it is 286 eV. Another important aspect of XPS is its surface sensitivity. The probing depth of XPS is typically between 1 - 5 nm. For comparison, XRD probes many microns into the sample, depending on its composition. A major strength of XPS is its ability to measure most elements, specifically Li and higher. Other X-ray techniques (XRF, EXAFS) are only applicable to heavier elements (Na and higher).

XPS analysis was ran on a Quantum 2000 scanning ESCA microprobe from Physical Electronics with a monochromatic Al K_α (1486.6 eV) X-ray source. The beam size was 100 μm and the analyzed

area was approximately 400 x 600 μm. The take-off angle was 45° with respect to the sample surface and the probing depth was approximately 4-5 nm.

3.2.2 X-ray fluorescence spectroscopy

X-ray fluorescence (XRF) is a technique used for elemental analysis of a sample. The sample is irradiated with high-energy X-rays and the secondary or characteristic X-rays emitted from the sample are measured. Based on the intensity of these characteristic X-rays, the elemental composition of the sample can be determined. The intensity is compared to calibration data in the instrument, which yields reasonably accurate concentrations to about 0.1 wt%. More exact concentration determinations, down to the parts per million level, require that a calibration curve be made from similar samples with known concentrations. In principle, the lightest element that can be measured and quantified by XRF is Be, but in practice, due to low X-ray yields from lighter elements, elements lighter than Na are difficult to measure. Unlike XPS, XRF spectroscopy is conducted in transmission mode such that the entire sample is measured; thus, XRF yields bulk elemental compositions. One of its primary disadvantages, however, is that the oxidation state of the element in question cannot be determined.

XRF was conducted on a Spectro Xepos HE XRF spectrometer using calibration data supplied by the manufacturer.

3.2.3 Elemental analysis

Elemental or combustion analysis (EA) is a quick and simple way of analyzing the "organic" elements of a sample, namely H, C, N, and S. A small quantity of sample is placed in a small piece of tin foil and loaded into the elemental analyzer. The sample is then dropped into a combustion tube where it is heated at 900°C in a pure oxygen atmosphere to ensure complete combustion of the sample. In subsequent steps, the excess oxygen is removed and the gases are reduced and purified such that only simple gases, products of the organic elements, remain. H is analyzed as H_2O, C as CO_2, N as N_2, and S as SO_2. These four gases are collected, quantified, and then presented as a weight percent of the total sample mass. The quantification happens in a single run. All other elements in the sample, whether gaseous and non-detectible (e.g. O, P, Cl, F) or solid and non-combustible (e.g. Fe, Si, Cu) are presented as a residual mass. EA, combined with other techniques such as TGA, XPS, and XRF, provide powerful tools for elucidating the elemental composition of a material.

EA was conducted on a Elementar Vario MICRO Cube HCNS analyzer.

3.3 Thermal characterization

3.3.1 Thermogravimetric analysis

Thermogravimetric analysis (TGA) is a method of thermal analysis where the mass of the sample is measured as a function of temperature. These measurements can provide information about various physical phenomena including phase transitions, solid-gas reactions (i.e. oxidation or reduction), chemi- and physisorptions, and thermal stability. The atmosphere can be inert (N_2, Ar), oxidizing (air, O_2), reducing (H_2 in N_2), or reactive (HCl, NH_3), depending on what properties are being studied. The temperature can be increased at a constant rate (dynamic) and/or can be held constant at a given temperature (isothermal). TGA can be coupled with other techniques such as differential scanning calorimetry (DSC), infrared spectroscopy (FTIR), or mass spectrometry to yield additional information about the processes occurring while the sample is heated.

In the context of this thesis, two main TGA programs were ran. The first program was under air heating at 30° min^{-1} to 900°C followed by an isotherm at 900°C for 20 min. This program was ran to combust all carbon and organic components from the sample, leaving behind only non-combustible material behind (e.g. SiO_2 and metal oxides). The final mass can be used to determine the effectiveness of silica template etching or metal loadings within the OMC. The second program was ran under N_2 heating at 10°C min^{-1} to 550°C followed by an isotherm at 550°C for 15 min. This program was used for determining sulfur loadings as well as quantification of grafted surface groups, namely amines.

TGA measurements in this study were performed on a Mettler TGA-DSC.

3.3.2 Differential scanning calorimetry

Differential scanning calorimetry (DSC) is a common thermal characterization method for the detection of phase transitions within a material. The heat flow is measured relative to a known sample and the difference is monitored. Two types of DSC are commonly used: power compensated and heat flux. For this work, the latter type was used.

The samples studied by DSC in this thesis were encased in sealed pan so that no material can leave or exit the system. The reference was an empty sealed pan. The two pans are placed in the DSC furnace where they are heated or cooled at the same rate and their temperatures are measured. If and endothermic process occurs (e.g. melting) the sample absorbs energy and a feature is recorded in the DSC trace. Usually endothermic processes are shown as a negative feature (pointing down). In the case of an exothermic process (e.g. crystallization), the sample gives off energy and are shown as a positive feature (pointing up).

The DSC used in this work was DSC Q1000 from TA Instruments.

3.4 Electrochemical characterization

3.4.1 Rotating disc electrode

Rotating disc electrode (RDE) is an electrochemical technique utilizing a three-electrode system to investigate reaction mechanisms related to redox chemistry, principally in the solution phase. In a typical set-up, the three electrodes are the reference, working, and counter:

Working electrode:	responsible for studying the reaction(s) of interest
Counter electrode:	balances the current passed to/from the working electrode; maintains electrical neutrality in the cell
Reference electrode:	provides a constant potential against which the potential of the working electrode is measured

Unlike other electrochemical techniques, in RDE, the working electrode is not static, but rather rotated at a constant angular velocity. This creates a convection force that replenishes the solution at the electrode surface, thereby making the flux of the redox active species to the surface constant (i.e. the flux is independent of time). The voltage is scanned at a constant rate from a potential where no redox processes occur to ($E < E_{1/2}$) to one where electron transfer is very fast ($E > E_{1/2}$). During this time, the current is measured as a function of the voltage.

At low potentials, the electrode kinetics dominate (i.e. rate of electron transfer); at high potentials, electron transfer is fast and the reaction is under mass transport control. At these potentials, the limiting current (I_L) can be modelled with the Levich equation:

$$I_L = 0.201nFAD^{\frac{2}{3}}\nu^{-\frac{1}{6}}c^{\infty}w^{\frac{1}{2}} \quad (10)$$

n = number of electrons transferred
F = Faraday constant (96485 C mol^{-1})
A = electrode area (cm^2)
D = diffusion constant ($cm^2\ s^{-1}$)
ν = kinematic viscosity ($cm^2\ s^{-1}$)
c^{∞} = bulk concentration (mol L^{-1})
w = rotation rate (rotations per min)

One of the most important parameters to be gained from RDE is the half-wave potential, $E_{1/2}$, or the potential at which the current is equal to one-half of the limiting current. This potential can reveal how well a catalyst is at facilitating a reaction, with better catalysts having $E_{1/2}$ closer to the thermodynamic potential (i.e. less overpotential).

4 Electrode and Li-S battery fabrication

4.1 Overview of the process

Once a carbon is made or modified, the eventual goal of this work is to test its competence as a host for sulfur in a Li-S battery. This is a multi-step process in which many parameters can be varied to alter the ultimate performance of the carbon. One of the central objectives of this thesis is to systematically alter the carbon's structure, composition, or surface functionalities and to see the effect these changes have on the battery performance; the intervening steps are merely necessities to transform the newly made carbon into a battery. In other words, the procedures for converting the carbon materials into batteries should be as uniform, reliable, and as reproducible as possible so that any observed differences in battery performance are attributable to the variations of the carbon materials under investigation.

This conversion takes place in three main steps: sulfur impregnation, electrode fabrication, and battery assembly. These steps are summarized in Figure 15 below:

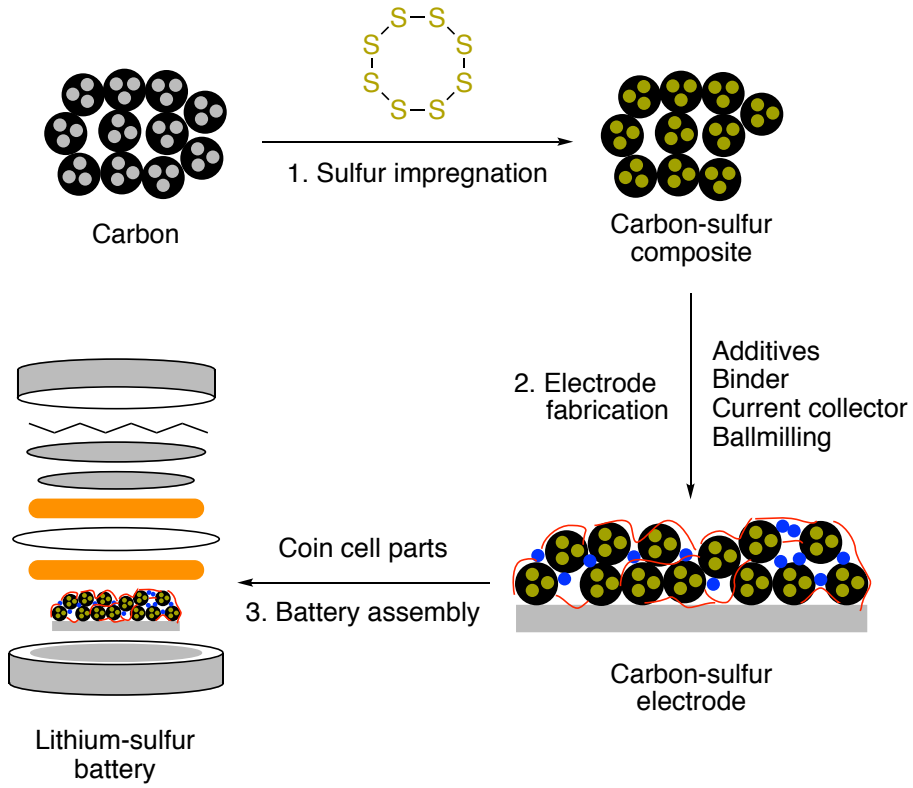

Figure 15. Overview of the processes employed in converting a carbon into a lithium-sulfur battery.

4.2 Sulfur impregnation

For sulfur impregnation, the amount of sulfur added must be carefully measured. For certain types of carbon (e.g. ordered mesoporous carbons, OMCs), there is an optimal amount of sulfur to add; for others, the sulfur content can be varied depending on the nature of the study. OMCs

have a well-defined pore structure and pore volume. It is from this pore volume that the mass of sulfur to be added can be calculated: if the pores are completely filled with the discharge product Li_2S, what volume (and mass) of sulfur does this correspond to? The calculation for the mass of Li_2S is calculated from the pore volume and mass of the OMC and the density of Li_2S. The units are shown in parentheses.

$$Mass\ Li_2S\ (g) = OMC\ pore\ volume\ (cm^3 g^{-1}) * OMC\ mass\ (g) * \rho\ Li_2S\ (g\ cm^{-3}) \quad (11)$$

Once the mass of Li_2S is known and because the molar ratio of S to Li_2S is 1:1, the mass of sulfur to add becomes the ratio of molecular weights (MW) of S and Li_2S:

$$Mass\ S\ (g) = \frac{Mass\ Li_2S\ (g)}{MW\ Li_2S\ (g\ mol^{-1})} * MW\ S\ (g\ mol^{-1}) \quad (12)$$

One can easily calculate the percent pore filling of the OMC based on the density of S; the pores are always filled to 55.9% of their total capacity. This corresponds to the aforementioned 80% volumetric expansion upon complete conversion of S to Li_2S: 55.9% x 180% ≈ 100%. While the percent of the pore volume filled with S does not change, the percent mass loading of S does increase with larger pore volumes. As shown in Table 4, increasing the pore volume from 0.5 cm^3 g^{-1} to 2 cm^3 g^{-1} increases the S loading from 36.7 to nearly 70 wt%. As one of the goals of the Li-S community is to maximize sulfur loading, increasing the pore volume of the carbon host is an effective way of accomplishing this objective.

Table 4. Calculation of how increasing the pore volume increases the maximum sulfur loading.

Pore volume (cm^3 g^{-1})	**Percent S loading (wt%)**
0	0
0.5	36.7
1.0	53.7
1.5	63.5
2.0	69.8

For other types of carbon with less well-defined pore structures (or none at all), no such calculation can apply and typically a moderate amount of sulfur is added. For the non-porous carbons used in this study (e.g. Vulcan), a final sulfur content of 45 wt% in the electrode was desired, which corresponds to 56.25 wt% in the C-S composite (if the C-S composite is used as 80 wt% of the electrode slurry; see Section 4.3).

Once the correct amount of sulfur is determined, the sulfur must be mixed with the carbon. This process occurs in multiple steps and is illustrated in Figure 16. The first step is to dry the carbon

to evacuate all pores and to obtain an accurate weight of the carbon. Then, the sulfur is mixed physically with the carbon, followed by heating at 155°C for 16 h to melt diffuse the sulfur into the carbon structures. The choice of 155°C is because liquid sulfur exhibits the lowest viscosity at this temperature.[73] For porous carbons like OMCs, there is an optional final step, which is to place the C-S composite into a vacuum oven at 200°C for 45 min. This is to remove any sulfur outside of the pores (i.e. surface-sulfur) while keeping the sulfur inside the pores intact. As sulfur is a strong insulator, keeping it strictly inside the pore space can decrease the electrical resistance among OMC particles and increase overall conduction within the electrode film.

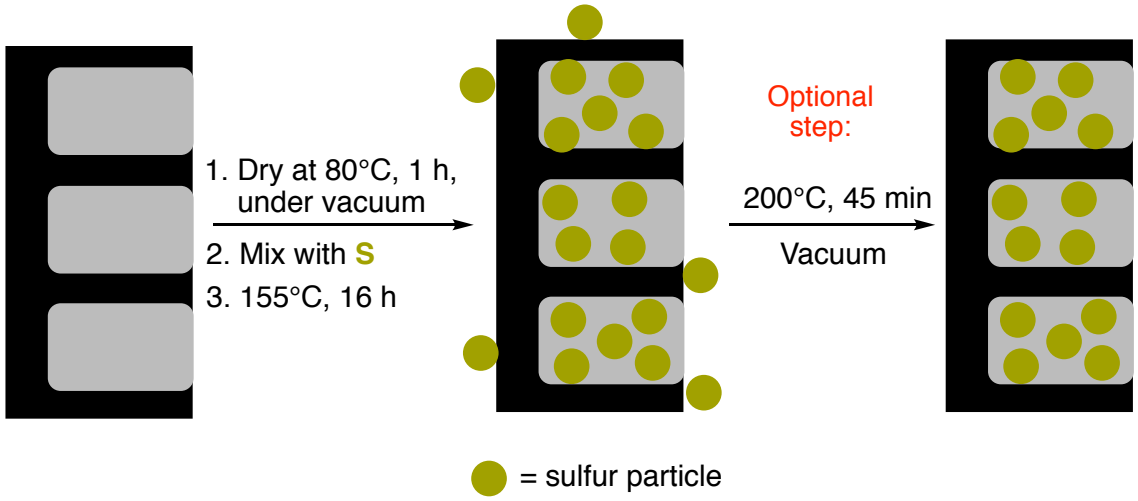

Figure 16. Depiction of the sulfur impregnation process into porous carbons. The last step is to remove any surface-sulfur.

To determine the final sulfur loading of the composite, one can subject it to thermogravimetric analysis under a nitrogen atmosphere or to combustion analysis (see Section 3). For samples containing delicate organic functionalities on the surface (e.g. grafted amines from bromomethylated carbons), combustion analysis is preferred as some of the mass loss in TGA is attributable to decomposition and detachment of these surface-bound functional groups.

With respect to the carbon-sulfur mixing process, this can be done with either a mortar and pestle or with ball milling. One short study with Vulcan-based electrodes, presented below, found that violent ball milling can have deleterious effects on the battery performance. The two mixing methods are compared below in terms of their battery performance. For the ball milled sample, the C and S were dry milled (i.e. no solvent) at 22 Hz for 30 min whereas the other C-S composite was gently mixed in a mortar and pestle for about 5 min. The electrodes and batteries were fabricated as detailed in the following sections in this chapter. Two batteries of each type were made and are presented in Figure 17 and Figure 18.

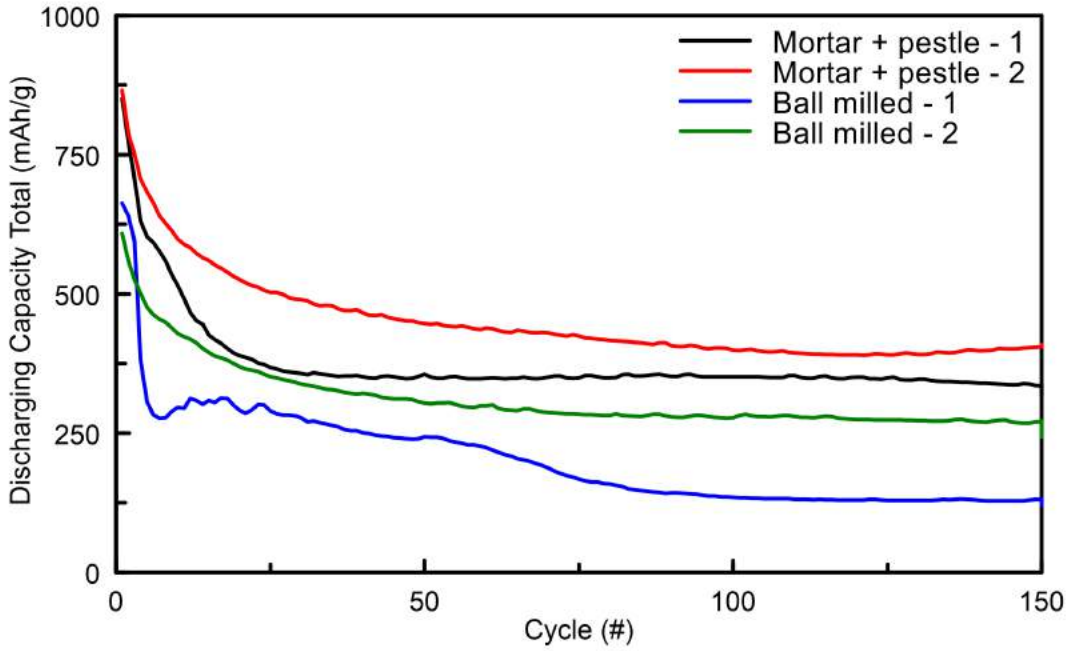

Figure 17. Cycling behavior of as a function of Vulcan + S mixing method.

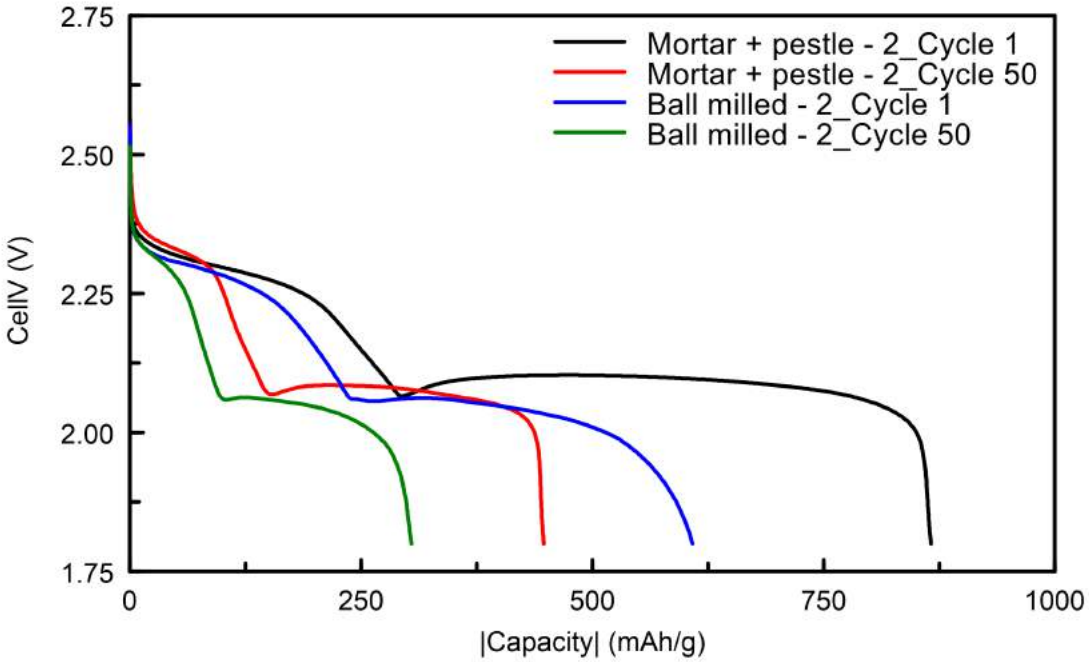

Figure 18. 1st and 50th discharge profiles of the better performing Li-S batteries of both mixing methods.

Figure 17 shows that, while there is some natural variation between batteries (see Figure 27), the mortar and pestle mixed samples measurably outperform both ball milled samples. The initial capacity is higher and the retention of sulfur over prolonged cycling is better. Figure 18 shows the discharge profiles of the 1st and 50th cycles of each type of cell, using the higher performing cell of each mixing method. In the case of the ball milled sample, the voltage is lower for both

plateaus, indicating a higher resistance to electron transfer to the sulfur. The plausible explanation for this deteriorated performance is loss of surface area upon ball milling; by dry ball milling pure Vulcan for 30 min at 22 Hz, the surface area was found to decrease from 330 $m^2 g^{-1}$ to < 100 $m^2 g^{-1}$, as determined by N_2-sorption.

It should be noted that no such problem was found for OMCs. No measurable decrease in battery performance was found with prolonged ball milling to mix the carbon and sulfur together. However, this study does point to potential problems associated with violent ball milling. When in doubt, the much gentler mortar and pestle mixing method is preferred.

4.3 Electrode fabrication

Once the C-S composite is made, the next step is electrode fabrication. The final goal of this step is to transform the C-S composite from a dry powder into a form amenable for battery testing. This process occurs in two sub-steps: transform the C-S composite into a "slurry" followed by coating it onto a piece of aluminum foil, called the current collector. The current collector serves two main purposes: one, as the name implies, it collects the current at the back of the cell and delivers it to the external circuit; two, it acts as a physical support for the coating, thereby allowing the electrode to be self-supporting.

4.3.1 Slurry composition and mixing

In a typical slurry making process, the C-S composite is ball milled together with Vulcan and a polyvinylidene fluoride (PVDF) binder along with N-methyl-2-pyrrolidone (NMP) as the solvent/dispersant (Figure 19). The first three components are mixed in an 8:1:1 mass ratio, respectively, with extra NMP added to adjust the viscosity of the slurry (Table 5).

Table 5. Typical components of an electrode slurry

Component and description	Role in electrode	Weight percent
C-S composite	S is electroactive material, carbon is conductive additive and material under investigation.	80
Vulcan	Additional conductive additive; small carbon nanoparticles help electronically connect larger particles in the film.	10
PVDF Binder	Tethers carbon particles together, helps slurry adhere to the current collector.	10
NMP	Works as the solvent/dispersant for the slurry. The amount added must be adjusted according to the types of carbon used and amount of sulfur in the carbon.	N/A

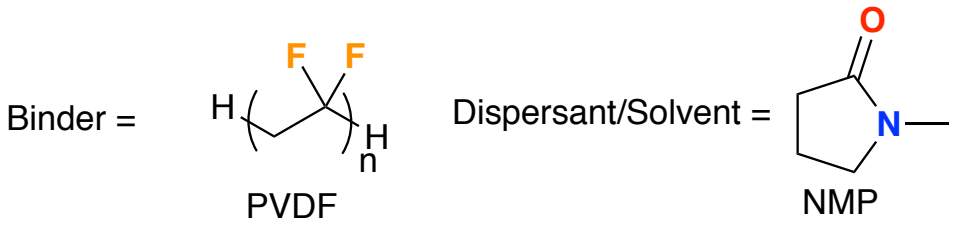

Figure 19. Chemical structures of the PVDF binder and NMP solvent/dispersant.

Vulcan XC-72R, is a type of conductive carbon nanoparticles of average diameter 50 nm.[74] The role of the added Vulcan is to provide small carbon particles that can effectively "fill the gaps" between the much larger OMC particles. This greatly increases the conductivity of the final electrode film.

The binder does exactly what its name says: it "binds" the carbon particles together as well as to the aluminum current collector. This allows the slurry to form a "paint" and to strongly adhere to the current collector. With no binder, the mixture simply dries and falls of the aluminum as a powder. The PVDF is added as a 5 wt% solution in NMP. PVDF is very slow to dissolve in NMP and so it is added as a pre-made solution. This ensures that the PVDF is well dispersed throughout the slurry and yields homogeneous electrodes. The roles of these three components as well as the current collector are illustrated in Figure 20.

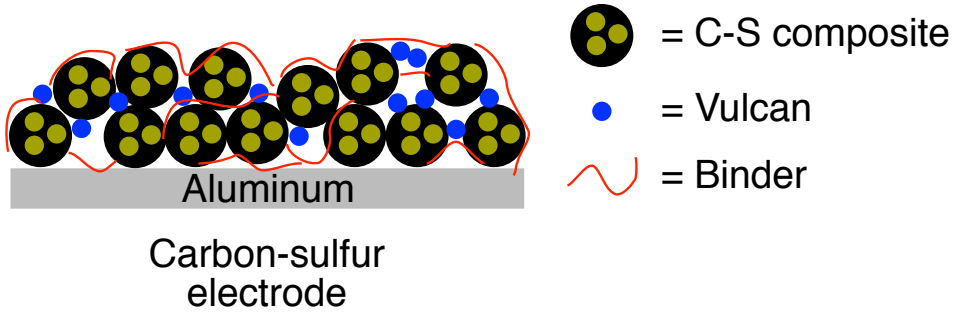

Figure 20. Illustration of the roles that the C-S composite, Vulcan, binder, and current collector perform in the electrode.

The electrode fabrication procedure has drastic effects on the final battery performance; indeed, this procedure can have a larger impact on the electrochemical testing than the nature of the carbon itself. An otherwise well-performing carbon will yield subpar battery results if the electrode preparation is done poorly. In the case that the electrode preparation is extremely defective (i.e. the carbon falls off the current collector after drying, Figure 21), battery testing cannot proceed at all. Therefore, if the goal of the study is to determine the impact of systematically modifying the carbon that houses the sulfur, then the electrode fabrication must be as simple and as reproducible as possible so as to minimize any effects of this procedure on the final battery performance.

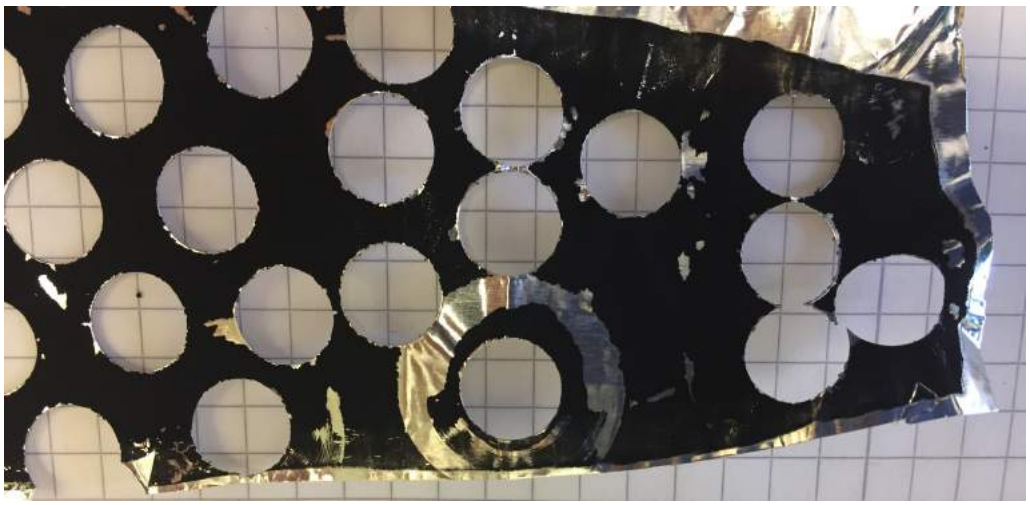

Figure 21. Picture of a poorly mixed electrode. The electrode film easily detached from the surface of the current collector when 13 mm diameter cathodes were cut.

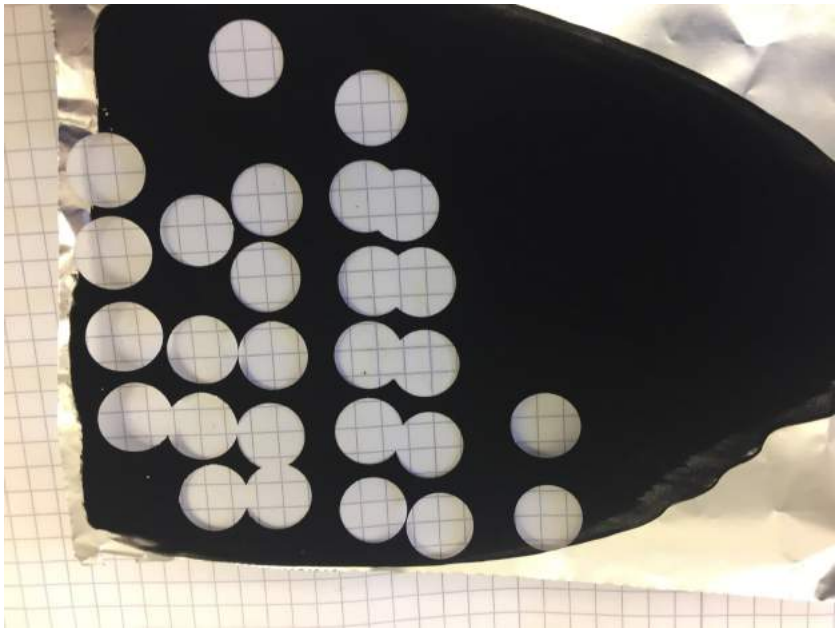

Figure 22. Picture of a well-mixed, well-coated electrode. Upon cutting the cathodes, the electrode film stayed completely adhered to the current collector.

4.3.2 Electrode coating

After making the slurry, the second sub-step is coating it onto the aluminum current collector. Two important tools assist in the coating process to make it as reproducible as possible: the doctor blade and auto-coater. The doctor blade is effectively a “gate” that only allows objects of a certain height or lower pass underneath it. The gate forces the slurry down to the preset height, thereby allowing the slurry to be coated at a consistent thickness. For all electrodes studied

herein, a coating height of 250 μm was chosen. After drying, the typical thickness (not including the current collector) was between 40 - 60 μm, representing a contraction factor of about 5. Film thicknesses after drying were measured mechanically with calipers (sensitivity = ± 5 μm).

The auto-coater serves two primary functions: one is to supply a flat surface on which to coat and the other is to provide a "hand," a moveable bar, that can push the doctor blade over the aluminum foil at a constant velocity. The auto-coater has the ability to pull vacuum on its flat surface, thereby allowing the current collector to maintain a flat profile. To perform the coating, the auto-coater pushes the doctor blade over the slurry at a constant velocity. The velocity of the hand can be adjusted from 1 mm s^{-1} to 200 mm s^{-1}. For all electrodes presented in this thesis, a slower velocity of 10 mm s^{-1} was chosen.

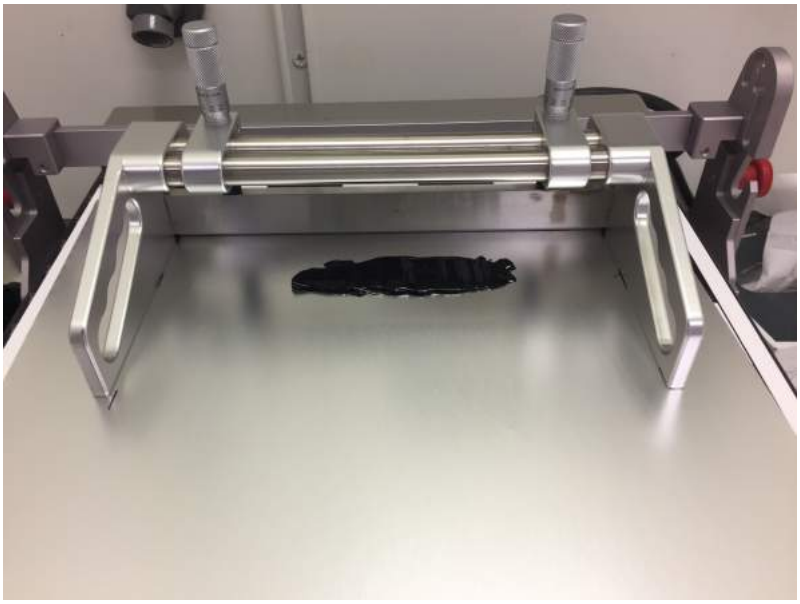

Figure 23. Picture of the doctor blade placed behind the carbon slurry just before coating.

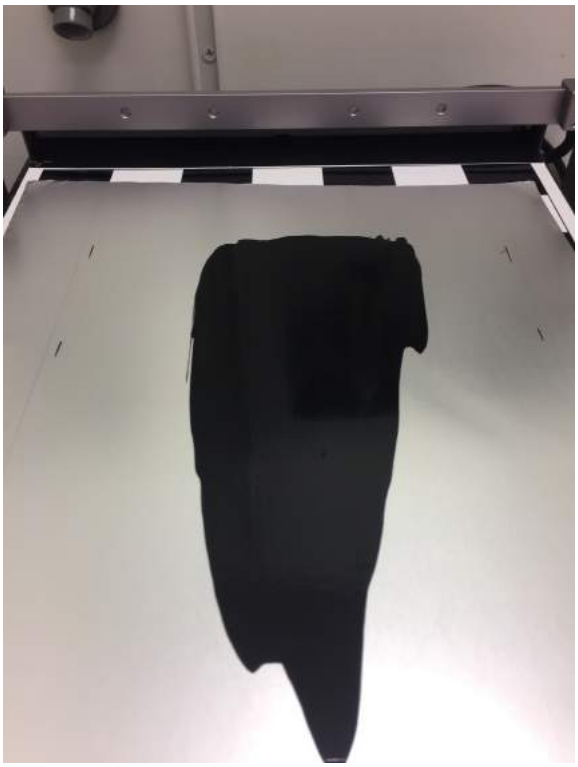

Figure 24. Picture of the carbon slurry after coating.

The coating now must be dried to remove the NMP solvent. The drying process is yet another variable in this process. Whether the electrode is allowed to dry slowly or quickly can have an influence on its performance as a cathode. This parameter was studied for the commercially available OMC CMK3 wherein two drying procedures were tested: one where the coatings were allowed to dry at room temperature (RT) for 16 h in the fume hood, followed by 2 h at 80°C; the other where the electrodes where dried immediately after coating at 80°C. All other parameters were kept the same. Three RT dried and two 80°C dried electrodes were tested in Li-S cells.

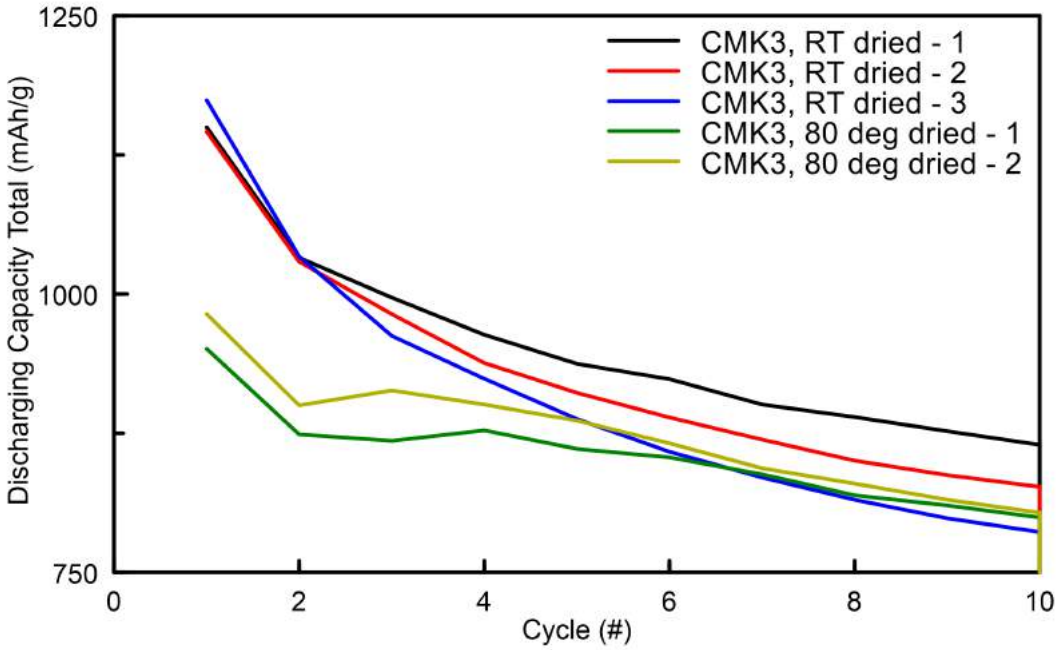

Figure 25. Performance of RT and 80°C dried CMK3 electrodes during the first 10 cycles.

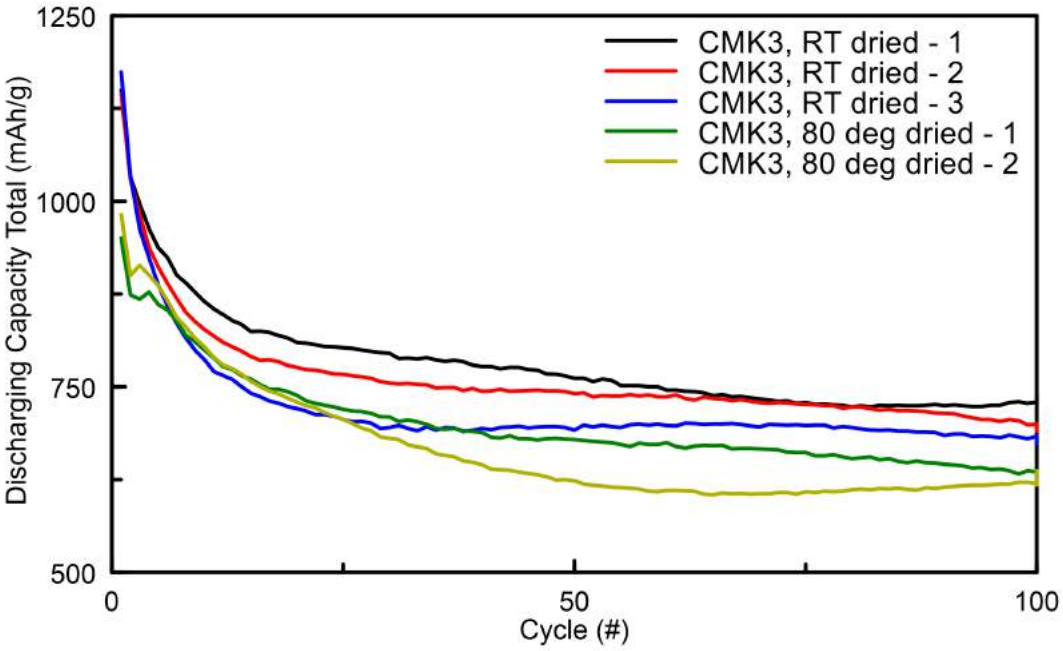

Figure 26. Long term cycling performance of RT and 80°C dried CMK3 electrodes.

Figure 25 shows the short-term cycling behavior. The RT dried electrodes have greater initial capacities while the 80°C dried ones show a somewhat stable capacity for the first few cycles before losing electroactive sulfur. The long-term cycling shown in Figure 26 reveals that all three RT dried cathodes outperform their 80°C dried counterparts. From this brief study, it was concluded that RT drying, while taking longer, yielded superior cathodes. Therefore, all battery

data presented in this thesis comes from cathodes dried for 16 h at RT before drying for 2 h at 80°C.

4.4 Battery fabrication

The ultimate test for a new carbon material is to test it as an electrode in a Li-S battery. The process continues from the electrode into a full cell. While in the glovebox, the electrode is built into a so-called "coin cell" for testing as the cathode in a Li-S battery. As with the electrode fabrication procedure, the coin cell construction can have a profound impact on the battery performance. The goal is to standardize the coin cell construction so as to minimize differences between samples. Regrettably, even when testing the exact same C-S cathode using the exact same coin cell making procedure, relatively large differences in battery performance can result (Figure 27).

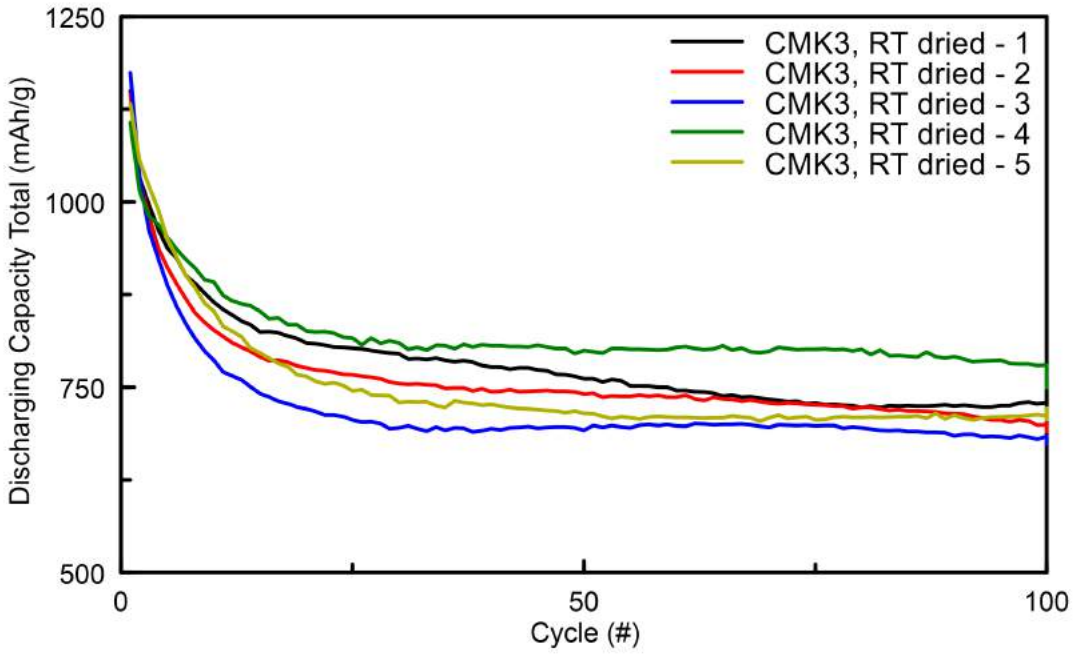

Figure 27. Cycling behavior of five Li-S cells made from the same electrode coating using the same battery fabrication procedure.

These results show that even when all variables should lead to equal performance, there will always be some variability. This applies to both short- and long-term cycling: the initial capacities vary between 1105 and 1175 mAh g^{-1} while the reversible capacities vary between 680 and 780 mAh g^{-1}. Also, the relative performance of the cells can also change as cycling continues.

Overall, this demonstrates that for one to say definitively that that one electrode performs better than another, the capacity must be considerably higher. *Considerably*, in this context, means at least 100 mAh g^{-1} higher, preferably 200 mAh g^{-1}. It is also for this reason that multiple cells for each electrode are made to ensure that the difference in capacity is reproducible.

To make a coin cell, the following device architecture is used with the parts listed in Table 6. These components are then constructed using the architecture shown in Figure 28.

Table 6. Coin cell components

Coin cell part	Purpose	Specifications	Picture
Casing and cap	To house the cell, to contain an inert atmosphere	Inner diameter = 20 mm	
Plastic gasket	To seal the cell hermetically	Outer diameter = 20 mm Inner diameter = 16 mm	
Spacer and spring	To provide pressure between all cell components; to assure electrical contact	Outer diameter = 16 mm	
Separator	Permeable membrane for Li^+ ions, to prevent electrical contact between anode and cathode	Porous polyethylene sheet (Celgard 2400) cut into 16 mm diameter circles	
Li anode	Used as counter and reference electrode for S cathode	Cut into 14 mm circles, oxide/nitride surface layer scraped off one side before use	
C-S cathode	Used as working electrode, study the carbon as a host for S	Cut into 13 mm diameter	
Electrolyte	To provide ionic conductivity	40 μL total volume	See Section 4.5

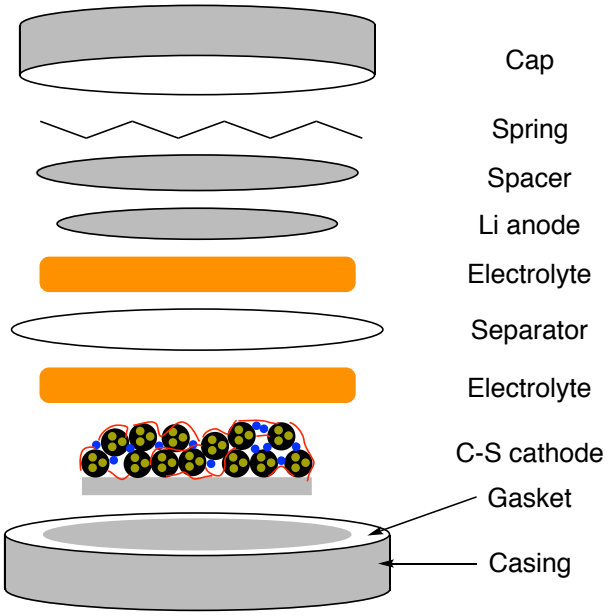

Figure 28. Construction of a Li-S coin cell with the component parts. The relative diameters of each component are taken into account.

4.5 Battery electrolyte

A large volume of research in the Li-S battery field, and indeed in all battery research, is dedicated to the study of electrolytes. This thesis focuses on the cathode, not the electrolyte, but a summary of common Li-S electrolytes is warranted.

The electrolyte must meet several requirements:

1. Provide fast Li^+ transport
2. Form a solid-electrolyte interface (SEI), if applicable
3. Be sufficiently non-volatile for long-term cycling
4. Be cheap and environmentally benign
5. In the case of Li-S batteries, allow solvation of LiPS

Any given electrolyte has three basic components: the solvent, which provides the medium for ion diffusion; a salt, which provides the Li^+ ions for ionic conductivity; and additives, which are mixed with the electrolyte to improve battery performance. The solvents typical of Li-ion batteries such as alkyl carbonates are not applicable in Li-S cells due to reactions with radical polysulfides.[67] Instead, the solvents for Li-S batteries are usually linear and cyclic acetals and ethers such as 1,3-dioxolane (DOL), 1,2-dimethoxyethane (DME), and tetraethylene glycol dimethyl ether (tetraglyme). A previous study[75] has shown that the linear DME provides higher LiPS solubility and reaction kinetics while the cyclic DOL forms a more stable SEI on the Li surface; therefore, using both solvents creates a synergetic effect and increased battery performance.

Other, less volatile solvents, have also been employed in Li-S cells like ethyl methyl sulfone[73], ionic liquids[76], and equimolar Li salt – tetraglyme complexes.[77]

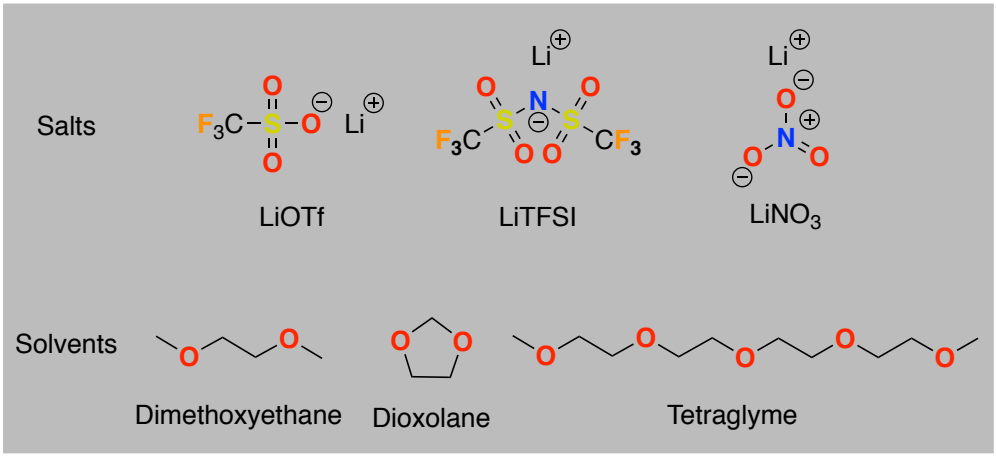

Figure 29. Chemical structures of common salts and solvents used in electrolytes for Li-S batteries

The Li salt is a central part of the electrolyte. It should be highly soluble in the solvent, provide fast Li^+ conduction, and be stable during cycling. The typical salts employed are salts of superacids, or Li salts with weakly coordinating anions (see section 2.1.4). Some of the classic salts including lithium tetrafluoroborate ($LiBF_4$) and lithium hexafluorophosphate ($LiPF_6$) are not amenable to Li-S electrolytes due to reactions with the dissolved LiPS.[78] Two other soluble salts, lithium trifluoromethanesulfonate (LiOTf) and lithium bis(trifluoromethanesulfonyl)imide (LiTFSI) have found to be the most suitable salts.[78] Of the two, LiTFSI is preferred because of its higher ionic conductivity and attenuated corrosion of the aluminum current collector.[79]

A key additive used in Li-S electrolytes is lithium nitrate ($LiNO_3$). A patent in 2008 revealed that by adding $LiNO_3$ to the electrolyte, the shuttle mechanism could be effectively stopped.[80] Consequently, these results have made $LiNO_3$ the single most important electrolyte additive and it is used in almost every Li-S publication after 2008.[81] The hypothesis was that the nitrate anions are reduced on the Li surface to Li_xNO_y, forming an SEI and preventing reactions with dissolved LiPS.[82] This hypothesis, however, is being reexamined; an alternate role of the nitrate anions in the electrolyte is to act as oxidation catalysts for PS to sulfur within the proximity of the sulfur cathode upon recharging.[81] In either case, $LiNO_3$ has been found to be an invaluable electrolyte additive. The use of $LiNO_3$ as an additive comes with a downside: Li-S cells utilizing this salt cannot be discharged below about 1.8 V since, below this value, the nitrate ions start to be reduced.

With all this considered, the final electrolyte composition chosen for the Li-S batteries in this thesis was a standard solution of 1 M LiTFSI with 0.4 M $LiNO_3$ in 1:1 DOL:DME (v/v) due to its high performance, high PS solubility, and common usage. The electrolyte was made with DOL and DME dried with 3Å molecular sieves in a glovebox. The salts used were ultra-low H_2O content LiTFSI

(H_2O < 20 ppm) and $LiNO_3$ that had been dried in vacuum at 50°C overnight in the glovebox. A few molecular sieves were added to the electrolyte to reduce the H_2O content further. The measured H_2O level by Karl-Fischer titration was < 60 ppm. For all cells, a total of 40 μL of this electrolyte was used per cell, which is in excess of what is needed. In most cases, closing the cell resulted in electrolyte being "squeezed" out of the cell. The decision to use excess electrolyte was to ensure that the battery performance was not limited by the amount of electrolyte used.

4.6 Battery testing

The battery testing constitutes the most important test for a new carbon material. Once the coin cell is made, a variety of testing procedures are available. Two of the most common are cyclic voltammetry (CV) and constant current (CC). Only CC testing was used in this thesis. As its name implies, current is drawn from the coin cell at a constant rate and the voltage is measured as the dependent variable. The current is drawn until a cut-off voltage is reached and the direction of the current is reversed. The process is the same going the other direction until the other cut-off voltage is reached and the current is again reversed. Figure 30 shows the voltage profile for one cycle of a typical Li-S cell. The cut-off voltages were 2.8 and 1.8 V.

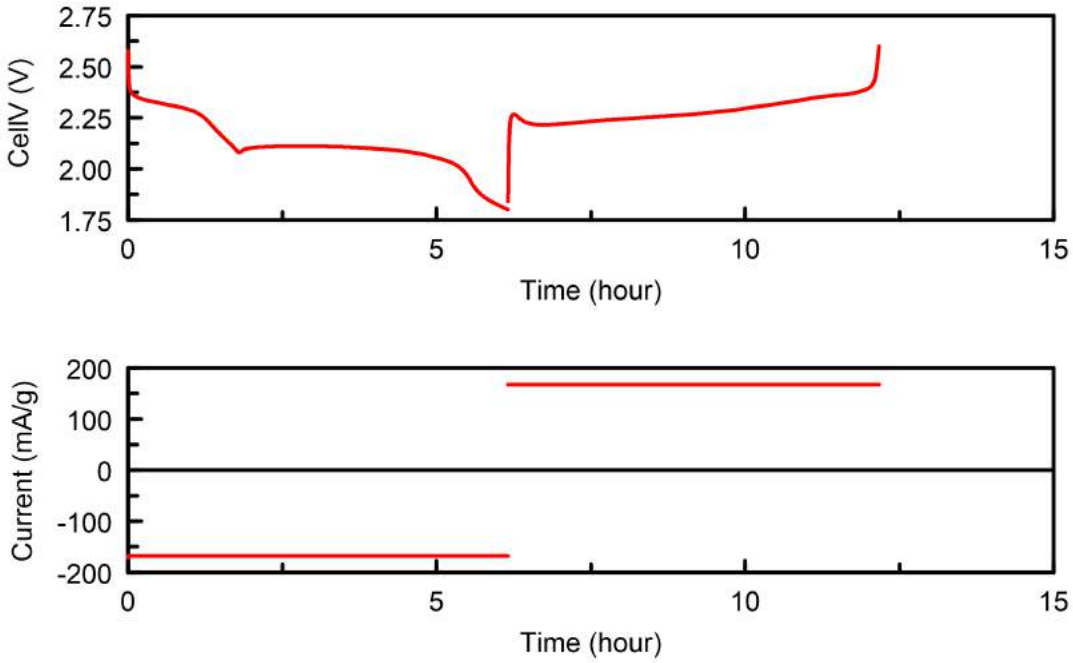

Figure 30. The upper panel displays typical discharge and charge profiles of a Li-S cell. The lower panel shows how the current is constant over time at its direction only changes when the cut-off voltage is reached.

Since the current is constant with respect to time, the x-axis can be either time (hours) or charge passed into or out of the cell (mAh g^{-1}). The latter is usually preferred to determine the performance of the cell.

The amount of current applied to cell can be measured in a few ways. Since electrodes can vary in weight, area, thickness, etc., it is important to normalize the current by one of these measurements. In most cases, the current is normalized by mass, specifically the mass of the cathode with all or some of its components being accounted for (see discussion at the end of this section). Some studies report the applied current in mA g^{-1} and for some electrochemical devices like supercapacitors, reporting the current as such is the norm. However, the battery community typically reports applied current as a "C-rate." The C-rate takes into account the theoretical capacity of the electroactive material and applies a current such that it is (theoretically) 100% charged or discharged in a certain amount of time. A rate corresponding to 1 C means that the battery should be completely (dis)charged in 1 hour; a rate of 5 C corresponds to 1/5 of an hour or 12 minutes; a rate of 0.1 C or C/10 ("C over 10") corresponds to 10 hours. All cells presented in this study were cycled at a rate of C/10.

The theoretical capacity for elemental sulfur is based on its mass and two electrons per sulfur atom. Equation 13 shows the conversion of this capacity to the usual units of capacities, or mAh g^{-1}:

$$\frac{Charge}{Mass} = \frac{2\ e^-}{32.06\ amu} = \frac{3.2\ x\ 10^{-19} C}{5.324\ x\ 10^{-23} g} = \frac{8.889\ x\ 10^{-23} Ah}{5.324\ x\ 10^{-23} g} = 1675\ mAh\ g^{-1} \qquad (13)$$

Thus, the theoretical capacity of elemental S is 1675 mAh g^{-1}. As detailed in Section 2.3, this capacity is much higher than those for typical Li-ion cells, which are about 150-200 mAh g^{-1}. To determine the amount of current actually applied to the cell, this theoretical capacity is divided by the time during which the cell should be (dis)charged: at a rate of 1 C, 1675 mA per g S is applied; at a rate of 5 C, 8375 mA per g S is applied; at a rate of C/10, 167.5 mA per g S is applied. Since all cells were cycled at a rate 0.1 C and have sulfur loadings of about 2 mg, the applied current to the cell was about 0.335 mA.

Although not performed in this study, many publications report how the cell responds to increasing the C-rate. Given the highly insulating nature of sulfur and its discharge products Li_2S_2 and Li_2S, Li-S batteries typically suffer the effects of increased C-rates more than other battery technologies. With increased current, the capacity is decreased and the voltage is lowered due to a higher iR drop and polarization. Less time is afforded for ion transport and equilibration among sulfur species. A hallmark of a good carbon (or a good Li-S cell as a whole), is exhibiting a high conductivity so that, at higher C-rates, the capacity and voltage loss is minimized. Figure 31 illustrates how increasing the C-rate affects battery performance.

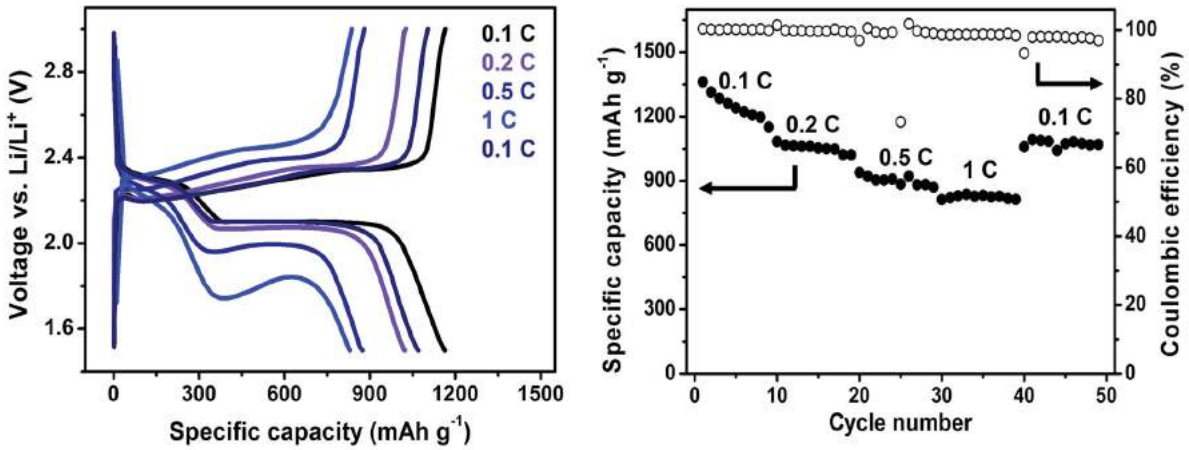

Figure 31. Example of how increasing the C-rate affects battery performance. Increasing the C-rate lowers both the capacity and the voltage.[57]

Many cycles, typically 100s to 1000s, are measured for a high performing coin cell, usually at the same C-rate. This type of repeated testing reveals valuable information on how well the carbon host can retain the active sulfur within its porous structure. A central goal of this project was to synthesize new carbon materials to better retain the LiPS, thereby minimizing the capacity loss. Figure 32 shows the capacity fading for two carbons, one with a porous structure (CMK3), and Vulcan, which lacks such a structure. While CMK3 loses some capacity during the first few cycles, the capacity eventually stabilizes to about 75% of its initial value after about 25 cycles. The stabilized value is called the *reversible capacity*. By contrast, the Vulcan electrode suffers a considerably larger initial loss and also experiences a slower, gradual loss afterwards and the capacity never reaches a stable value, even after 100 cycles.

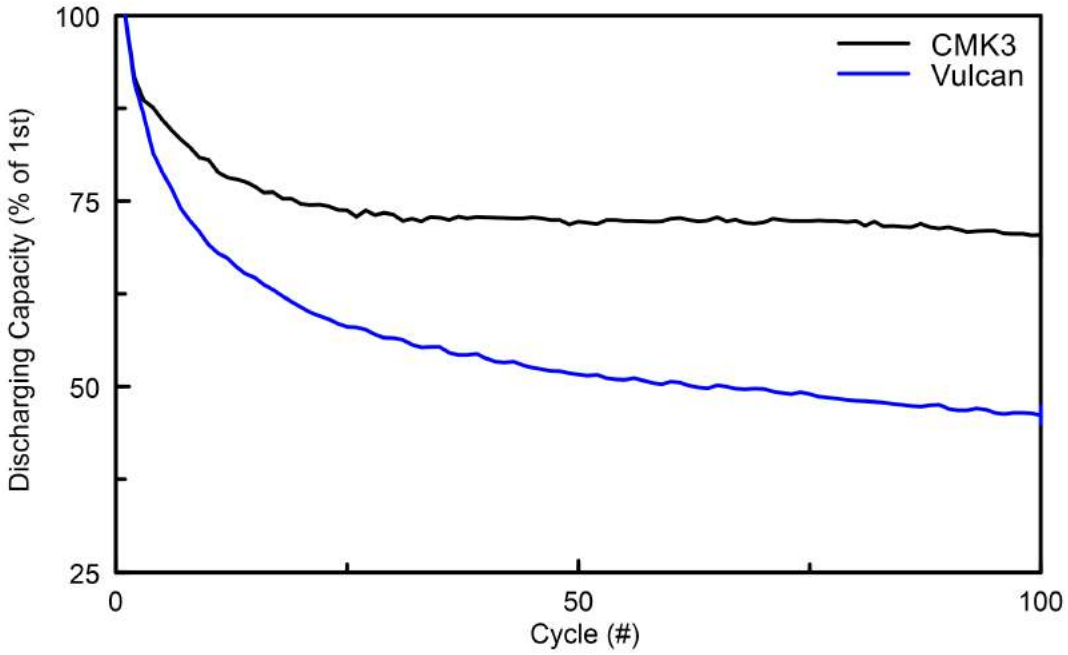

Figure 32. Comparison of the cycling stability of a Vulcan and CMK3 cathode. The porous structure of CMK3 is better suited for PS retention than the particulate, non-porous structure of Vulcan.

As a final comment in this section, the masses used for normalization of the current, capacity, and energy density should be discussed. A typical cathode consists of multiple components: sulfur, carbon host, additives (i.e. Vulcan), binder, and current collector. Since sulfur is the active material, this mass is always included. Inclusion of the other components is optional. The applied current is almost always normalized by the sulfur mass alone because the C-rate is calculated from the theoretical capacity of pure sulfur. For capacity (mAh g^{-1}) and energy density (Wh g^{-1}), the normalization has the option of including some of the electro-inactive components. If only the sulfur mass is used, the measured capacities and energy densities represent what percent of sulfur is being utilized; for example, a reversible capacity of 1000 mAh per g S indicates that 1000/1675 or 60% of the sulfur is being reversibly used. However, if the sulfur loading is very low and excess carbon is used, this number can be artificially high. Inclusion of the other masses incorporates the sulfur loading into the measured capacity: if two cathodes are compared where the sulfur loadings are considerably different, normalization with the total cathode mass makes for a fairer comparison. Moreover, for studies that focus on cathode fabrication where an electro-inactive component can be discarded (e.g. binder-free cathodes[83]), normalization with all cathode components emphasizes this key feature.

Lastly, normalization by electrode area represents another option. This yields units of mAh cm^{-2} for the capacity, for example. Normalization performed in this way takes into account how thick the cathode is. The gravimetric data can be improved by making super thin cathodes, thereby greatly attenuating some problems like ion diffusion. Normalization with respect to area takes the thickness of the cathode into account, with thicker electrodes having the advantage.[83] All

normalizations in this thesis were done with respect to the sulfur mass only. Future studies will involve other normalizations.

5 Study 1: Copper salt selection and improvement to the OMC synthesis

5.1 Overview

The objective for this first study was to determine what effect changing the anion of the dopant metal salt has on the resultant carbon material. As stated in Section 2.1.5, copper was chosen as the cation due to its soft Lewis acid character. In addition to this primary variable, two changes were made to a published procedure for the synthesis of ordered mesoporous carbons (OMCs) by Dombrovskis et. al.[15] In the context of this thesis, this first, published procedure will be referred to as Procedure 1. The modified procedure, used here in Study 1, is referred to as Procedure 2. The two important differences between these two procedures are as follows:

1. The first silica impregnation with carbon precursor solution was only performed once. The volume used corresponded to the pore volume of the silica template. Then, the sample was allowed to sit at room temperature for 2 h followed by heating for 2 h at 100°C then additional 2 h at 160°C, both under air. The sample was then carbonized for 2 h at 950°C, heating at a rate of 15 °C min^{-1} at an argon flow rate of 100 mL min^{-1}.
2. After the first carbonization, N_2-sorption was ran to determine the *residual* pore volume of the silica template. The silica-carbon composite was impregnated again with fresh carbon precursor solution, this time with a volume corresponding to the residual pore volume. The samples were then heat treated and carbonized in the same way as before.

The goal with determining the residual pore volume after one impregnation was to not "over fill" the silica pores. The old procedure fills the silica pore twice in quick succession, each time using the *full* pore volume. This almost certainly results in some precursor solution residing outside of the pore space of the silica, which, then, during carbonization, turns into bulk carbon with low surface area and porosity. The secondary objective of this study was to see if this addition to the OMC synthesis procedure can increase the surface areas and pore volumes. The procedure used for creating the copper salt solution in furfurylamine was the same as in Study 3 for iron salt solutions in the same solvent.

5.2 Copper salt selection

For the first study eight different OMC samples were made using two carbon precursors, furfuryl alcohol (FOH) and furfurylamine (FNH_2), and six different copper salts. The 8 samples are listed in Table 7. The structures of the carbon precursors and the dopant copper salts are shown in Figure 33 and Figure 34.

Table 7. Details of the eight OMC samples prepared in Study 1.

Sample number	Carbon precursor	Copper salt	Designation
1	FOH	None (undoped)	1-O
2	FNH_2	None (N-doped)	2-N
3	FNH_2	$CuCl_2$	3-Cl
4	FNH_2	$Cu(BF_4)_2$-nH_2O	4-BF4
5	FNH_2	$Cu(OTf)_2$	5-OTf
6	FNH_2	$Cu(OAc)_2$-H_2O	6-OAc
7	FNH_2	$Cu(acrylate)_2$	7-Acryl
8	FNH_2	$Cu(methacrylate)_2$	8-Meth

$CuCl_2$ was chosen as the reference salt with a "normal" anion that should show marginal solubility in the FNH_2 solvent. $Cu(BF_4)_2$-nH_2O, $Cu(OTf)_2$, represented salts with weakly coordinating, inorganic anions that should hopefully be much more soluble. The final three salts of $Cu(OAc)_2$, $Cu(acrylate)_2$, $Cu(methactylate)_2$ contain organic anions that should carbonize along with the FNH_2 carbon precursor. Interestingly, the acrylate and methacrylate anions contain a polymerizable anion, which, in principle could help form the organic polymer before carbonization (Figure 35).

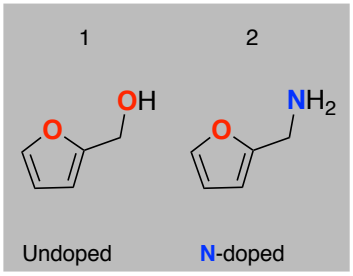

Figure 33. Structures of the carbon precursors, furlfuryl alcohol (FOH) and furlfuryl amine (FNH_2)

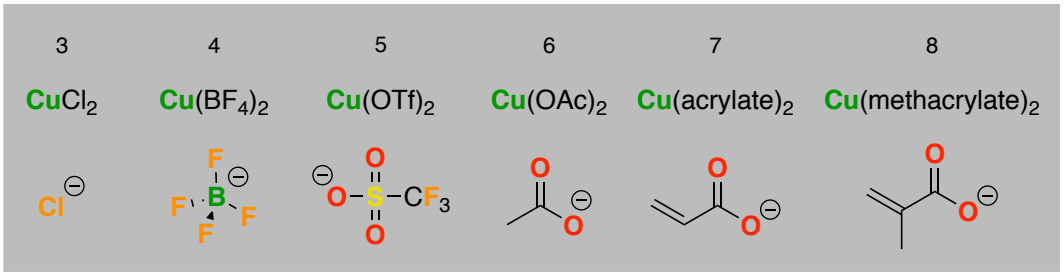

Figure 34. Structures of the anions for the dopant copper salts.

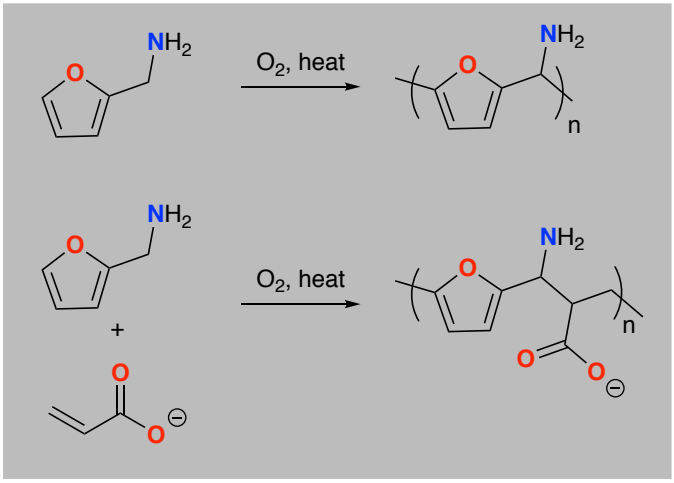

Figure 35. Possible structures of poly(furfurylamine). In the case of acrylate and methacrylate, these anions can theoretically co-polymerize with FNH_2, perhaps altering the structure of the resultant OMC.

In the process of the synthesis, the approximate solubilities of the salts were recorded (Table 8)

Table 8. Approximate solubility limits of Cu(II) salts in FNH_2

Copper salt	Approximate solubility limit (mg mL^{-1})
$CuCl_2$	30
$Cu(BF_4)_2$-nH_2O	850
$Cu(OTf)_2$	950
$Cu(OAc)_2$-H_2O	500
$Cu(acrylate)_2$	50
$Cu(methacrylate)_2$	230

Interestingly, all salts, except for the chloride, exhibited a dark blue color in solution whereas the chloride salt yielded a teal colored solution. This could have something to do with the strongly nucleophilic nature of chloride compared with the other anions. Perhaps this complex in FNH_2 solution contains Cu-Cl bonds (in addition to Cu-N bonds) but all other salts contain only Cu-N bonds.

As expected, the standard chloride salt demonstrated a solubility that was significantly less than most of the other salts. $Cu(BF_4)_2$-nH_2O and $Cu(OTf)_2$ were exceedingly soluble to the point where the solution was nearly black in color. This made the solubility limit hard to determine, but was likely over 800 mg mL^{-1}. $Cu(OTf)_2$ also showed strong exotherms upon dissolution in FNH_2. The solution had to be continuously cooled or else premature polymerization of the FNH_2 would occur; this reaction was marked by a strong color change from blue to brown. $Cu(OAc)_2$-H_2O showed much enhanced solubility relative to the chloride, but not as much as either $Cu(BF_4)_2$-nH_2O or $Cu(OTf)_2$. This could be due to that acetate anion contains a solubilizing methyl group

within its structure, but is still more coordinating than either BF_4^- or OTf^-, thereby reducing its solubility. The comparison between the last two salts, acrylate and methacrylate, demonstrates how important structure is in determining solubility. Acrylate, while organic, only contains sp^2 hybridized carbon atoms and has a solubility that is not so much higher than the standard chloride. The addition of a single methyl group to form methacrylate greatly enhances the final concentration, albeit not as high as acetate, BF_4^- or OTf^-.

5.3 N_2-sorption results

After the synthesis, the as-synthesized copper-doped OMCs (Cu-OMCs) were studied by N_2-sorption, XRD, TGA, and XPS. The first test was N_2-sorption to see if the Cu-OMCs exhibited reasonable surface areas and pore volumes. The summary of this data is shown in Table 9.

Table 9. Summary of N_2-sorption results for Study 1.

Sample	BET surface area ($m^2 g^{-1}$)	BJH pore volume ($cm^3 g^{-1}$)
1-O	1066	1.14
2-N	1082	1.54
3-Cl	887	1.09
4-BF4	580	1.13
5-OTf	630	1.08
6-OAc	662	0.84
7-Acryl	1043	1.65
8-Meth	1034	1.71

These results show that some variation exists among the eight samples, but that all samples showed reasonable surface areas and pore volumes; the addition of various copper salts of varying solubility did not seem to hinder pore impregnation into the silica template. There is, however, a correlation between solubility and surface area: the copper salts exhibiting the highest solubility (4-BF4, 5-OTf, and 6-OAc) also had the lowest surface area. This correlation could result from the addition of significant amounts of denser elements making the overall density of the OMC higher.

To see if the changes had any effect on the surface properties of these OMCs, the surface areas and pore volumes for the undoped and N-doped samples were compared to the published values. These numbers are detailed in Table 10 and Table 11.

Table 10. Comparison is BET surface areas (m^2 g^{-1})

Sample	Procedure 1	Procedure 2	Change
Undoped	653	1066	+63.2%
N-doped	704	1082	+53.7%

Table 11. Comparison in BJH pore volumes (cm^3 g^{-1})

Sample	Procedure 1	Procedure 2	Change
Undoped	0.986	1.14	+15.6%
N-doped	0.693	1.54	+122.2%

By splitting the impregnations and subsequent carbonizations into two steps, the final surface areas and pore volumes can be moderately to greatly enhanced. The surface areas of both samples increase to the level of commercially available OMCs like CMK3, which has a surface area of 1069 m^2 g^{-1}. In terms of the pore volumes, the undoped sample increases by a modest 15.6%, but the N-doped sample more than doubles its value to 1.54 cm^3 g^{-1}. For reference, this is higher than CMK3, which has a pore volume of 1.35 cm^3 g^{-1}.

5.4 XRD results

The X-ray diffractograms reveal principally two features of the OMC: one, if any crystalline particles are present, and two, the degree of graphitization of the carbon. Figure 36Figure 37 show the diffractograms of all eight samples.

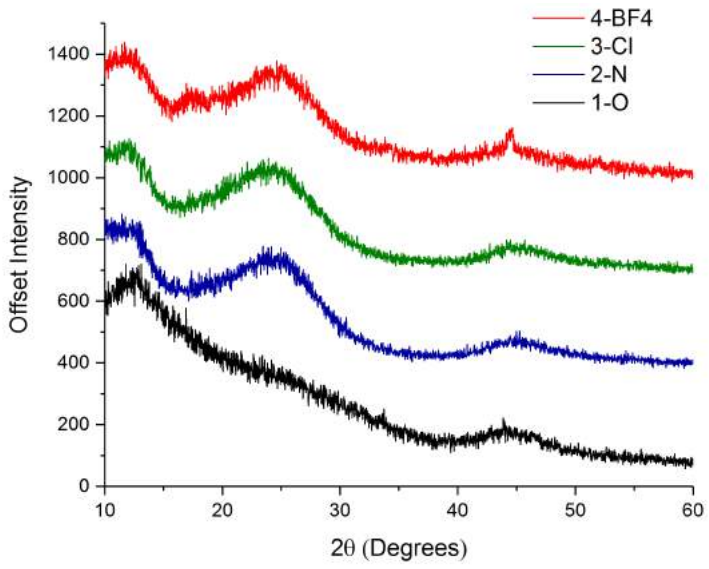

Figure 36. X-ray diffractograms of 1-O, 2-N, 3-Cl, and 4-BF4 Cu-OMCs

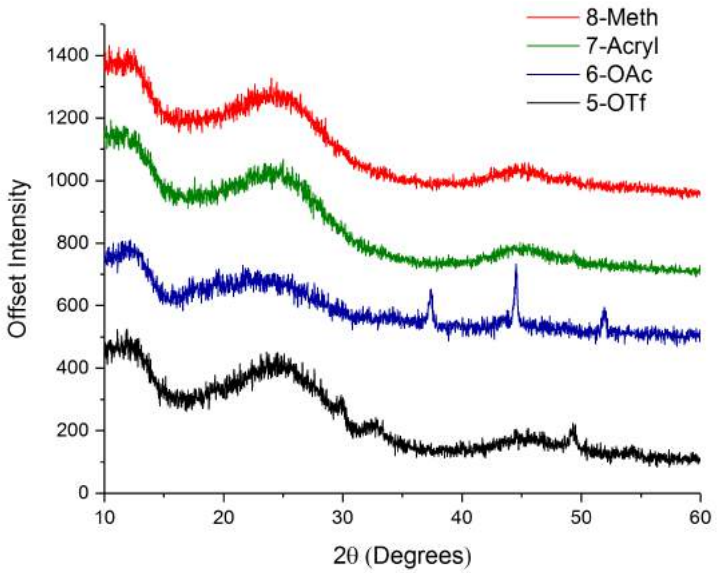

Figure 37. X-ray diffractograms of 5-OTf, 6-OAc, 7-Acryl, and 8-Meth Cu-OMCs

All diffractograms show the broad, amorphous carbon diffraction peaks at 12°, 25°, and 45°. 1-O has similar peaks at 25° and 45°, but the peak at 12° is of considerably higher relative intensity. The reason behind this increase remains unknown. The most conspicuous result comes from 6-OAc, which has sharp diffraction peaks at 37°, 44°, and 52°. This indicates the presence of crystalline phase within the sample. The 2θ value at 37° is consistent with CuO and the 44° and 52° are indicative of Cu^0. It was observed that, during the polymerization step of the synthesis, the 6-OAc material turned a deep black color immediately upon being placed in the oven. For comparison, all other samples only changed colors from blue to brown/black after the second heat treatment at 160°C for 2 hours. One possible explanation for the presence of crystalline particles is that the Cu^{2+} ions, in tandem with the acetate ions, catalyzed the polymerization of the FNH2. This fast polymerization likely resulted in a strong exotherm and volatilization of the solvent, causing Cu salt precipitation within the confines of the silica template. Upon heating at 950°C, these salts decomposed into CuO and Cu^0 crystallites.

Two other samples also showed diffraction peaks: 4-BF4 and 5-OTf. 4-BF4 exhibited two of the same peaks as 6-OAc at 2θ values of 44° and 52° (the peak at 52° is barely discernable). This sample likely has Cu^0 particles within its structure. 5-OTf showed broad, weak peaks at 2θ values of 29°, 33°, and 49°. However, no structure was possible to determine for this sample.

5.5 TGA results

The main test for these sets of samples was to determine the copper loadings and to see if they were increased relative to the standard 3-Cl sample. For this determination, two techniques were employed: TGA and XPS. In TGA, the first program was used (See Section 3.3.1) to burn off the carbon matrix and determine the effectiveness of the SiO_2 template etch and final copper loading.

The thermograms for all eight samples are shown in Figure 38 and the residual masses for all copper-doped samples are listed in
Table 12.

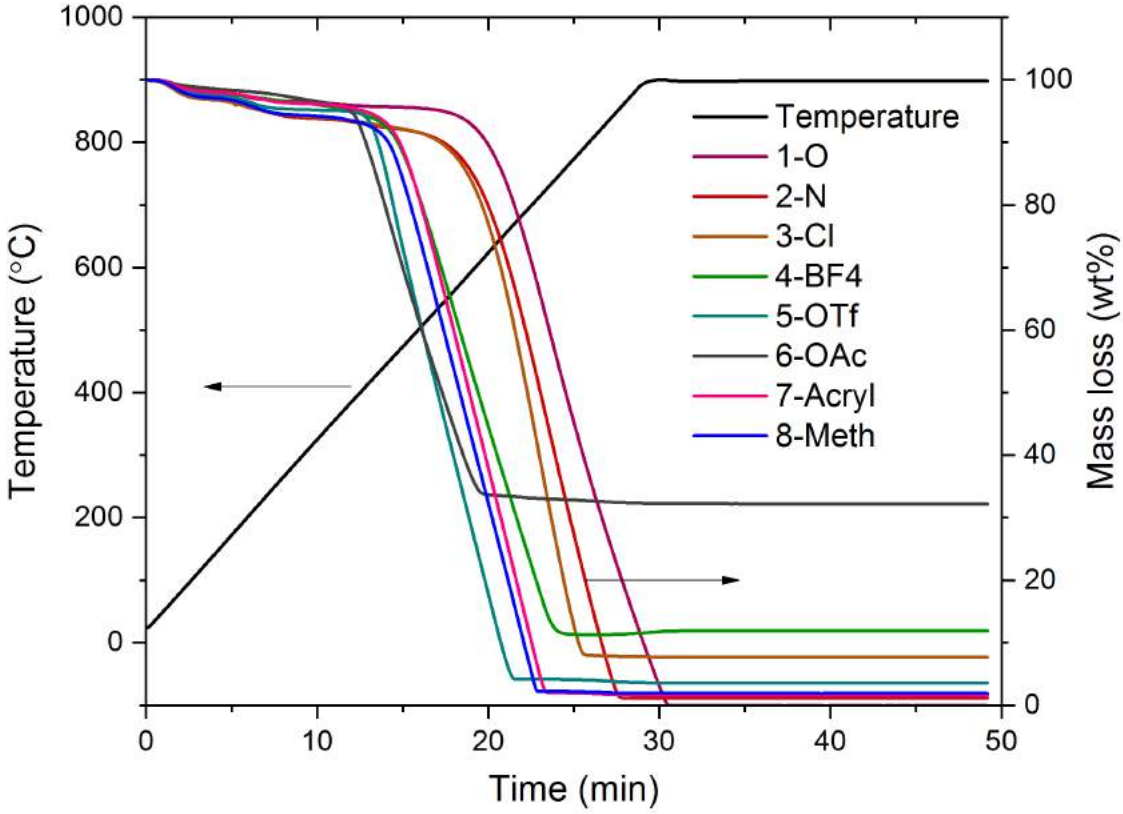

Figure 38. Thermograms of OMCs ran under air. The final masses correspond to copper loadings.

Table 12. Residual masses and calculations of copper loadings based on TGA. All numbers are in weight percent (wt%).

Sample	Residual mass	CuO mass*	Cu mass§
1-O	-0.045	N/A	N/A
2-N	1.14	N/A	N/A
3-Cl	7.70	7.96	6.36
4-BF4	11.92	12.18	9.73
5-OTf	3.58	3.67	2.93
6-OAc	32.18	32.67	26.10
7-Acryl	1.66	1.69	1.35
8-Meth	1.90	1.96	1.56

**Corrected for hydration mass*
§Based on weight % of Cu in CuO (79.89%)

To accurately determine the wt% copper in each sample, the water weight (hydration) was subtracted from the residual mass. The hydration mass was taken at the temperature of 150°C.

The residual mass, given in wt%, was assumed to be entirely CuO, since, under an oxidizing atmosphere at 900°C, any organic matter should oxidize and volatilize and any copper species should be oxidized to CuO. For 1-O, no mass was remaining after combustion, indicating complete removal of the silica template. For 2-N, however, about 1 wt% remains, so the template removal for this sample might not have been as effective. This residual mass is close to those measured for 7-Acryl and 8-Meth, so these two Cu-doped OMCs might not contain any significant amounts of Cu. 3-Cl, despite its low solubility, had a much higher residual mass around 7.7 wt%, which corresponds to a Cu-loading for 6.36 wt%. This could indicate that $CuCl_2$ is a competent dopant in this synthesis. 4-BF4 had a higher mass at nearly 12 wt% or a Cu-loading for 9.73 wt%. In the case of this salt, its higher solubility does lead to higher loadings. 5-OTf yielded an OMC with about half the Cu-loading of 3-Cl. 6-OAc had a disproportionately high Cu-loading of about 26 wt%. As mentioned in the previous section, the odd behavior of this sample during preparation could indicate an artificially high Cu-loading. Moreover, based on the X-ray diffractogram, lot of this mass is likely crystalline Cu^0 and CuO and not copper ions covalently bonded within the graphitic sheets as was the goal.

It must be stressed, however, that determination of Cu-loadings via TGA must be taken with a grain of salt. Other factors could result in a residual mass other than Cu species; residual silica template, contamination from other samples (see next section), and/or pieces of crucible in the sample could also result in residual masses.

5.6 XPS results

To further test for Cu-doping, XPS was conducted on the samples testing for the elements that could theoretically be present for each OMC based on the components of each carbon precursor, including the silica template, pTSA pretreatment, and HF etching. The results are shown in Table 13.

Table 13. Surface concentrations of elements based on XPS analysis in atomic percent.

Sample	B1s	C1s	N1s	O1s	F1s	S2p	Cl2p	Cu2p	Si2p
1-O	-	91.05	3.15	5.24	0.33	0.23	-	-	-
2-N	-	89.59	3.88	5.70	0.47	0.35	-	-	-
3-Cl	-	86.61	2.54	10.11	0.58	-	0.16	-	-
4-BF4	1.57	78.87	9.30	7.27	1.54	0.11	-	1.33	-
5-OTf	0.76	88.22	3.44	5.70	-	0.80	-	1.08	-
6-OAc	-	64.88	2.91	17.29	2.92	0.81	-	9.46	1.73
7-Acryl	-	87.24	4.76	6.97	-	0.52	-	0.52	-
8-Meth	-	89.02	3.84	6.03	0.52	0.58	-	-	-

From these data, several points can be made. The first, and likely most important, is that in 1-O, made from pure FOH, contained a significant amount of nitrogen. Since all eight samples were carbonized together, the FNH_2 must have volatilized to a significant degree and contaminated 1-O. A similar conclusion can be reached for 5-OTf, which contained some boron. The only source of boron during the synthesis was from the anion in the 4-BF4. This result also supports cross-contamination.

In spite of likely cross-contamination among the OMCs, some conclusions can be reached. Interestingly, all but one sample contained some sulfur, which must have come from the sulfonic acid group in pTSA during the pretreatment. The silica template, while washed with ethanol and dried prior to impregnation with the carbon precursor solution, must have retained some pTSA. All but 5-OTf and 7-Acryl had some amount of fluorine, likely indicating that some fluorine from the HF etch remained within the structure. All samples had large amounts of both nitrogen and oxygen, as would be expected, as the FNH_2 carbon precursor contains these elements.

Many of the anions from the Cu salts included elemental "tags" that can help to determine what happened to them during the synthesis process. 3-Cl had a small, but detectible amount of Cl, possibly indicating that this anion is incorporated into the structure during carbonization. 4-BF4 had large amounts of both boron and fluorine, so this anion was likely absorbed into the carbon matrix too. 5-OTf had a higher sulfur concentration than most samples, but no fluorine. Given these concentrations, it is impossible to say if the OTf anion incorporates itself into the carbon structure. The sulfur could come from the pTSA or from the OTf anion.

Most importantly, though, is the copper doping levels. The Cu_{2p3} spectra are shown in Figure 39Figure 40. Figure 39 displays the high-resolution spectra for 5-OTf, 6-OAc and 7-Acryl OMCs. Unfortunately, no high-resolution spectrum was acquired for 4-BF4, so a Cu2p3 region of the survey spectrum is shown in Figure 40; as such, the noise level is much higher and the accuracy of the Cu concentration is lower.

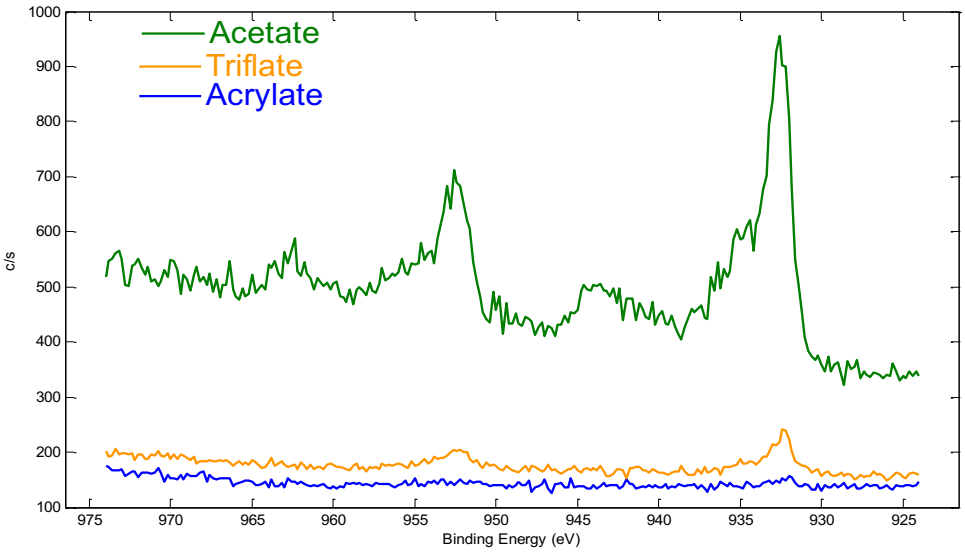

Figure 39. High resolution XPS spectra of the Cu_{2p3} region for 6-OAc, 5-OTf, and 7-Acryl.

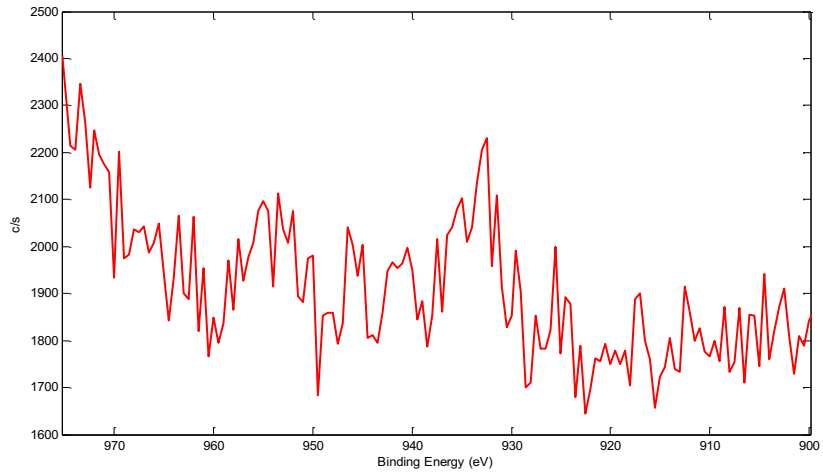

Figure 40. Spectrum of the Cu2p3 region for 4-BF4.

6-OAc, as expected, had a much higher Cu concentration than any other OMC, corroborating the findings of TGA. The chemical shifts in the Cu_{2p3} region reveal two species: Cu^0 at shifts of 934 and 953 eV and CuO at shifts of 944 and 962 eV. This validates the copper phases present in the X-ray diffractogram. The peaks in the spectra for 5-OTf and 7-Acryl suggest that the copper species present is also Cu^0, with no detectible amount of CuO or other species. The higher noise spectrum of the 4-BF4 shows a discernable peak around 934 eV and another, almost hidden peak around 953 eV. These chemical shifts likely point to Cu^0 species as well, although from the noise level, it is difficult to say definitively. Distinct from the 6-OAc, however, none of these OMCs exhibited diffraction peaks in XRD; thus, the Cu species is probably either Cu^0 atoms bound within the carbon framework or Cu nanoparticles too small in size to be detectable by XRD, or some combination of the two. The overall copper loadings determined by XPS is in the order 6-OAc >

4-BF4 > 5-OTf > 7-Acryl. No detectible amounts of copper were found for either 3-Cl or 8-Meth. From both TGA and XPS, only four samples had Cu: 4-BF4, 5-OTf, 6-OAc and 7-Acryl.

5.7 Conclusions from Study 1

Due to time constraints, these samples were not tested in Li-S batteries. However, several conclusions can be drawn from this study. First and foremost, is the importance of carbonizing the samples individually. While each sample filled its own 30 mL alumina crucible to about 1/3 the capacity, heating at 950°C with argon flow for 2 h causes sufficiently high vapor pressure of the FNH_2 polymer and, apparently, of certain copper salts as shown by contaminant boron in the 5-OTf. For future OMC syntheses, each sample should be carbonized individually.

Secondly, the two-hour impregnation time is likely too short for efficient pore filling. The Cu salt solutions in FNH_2 proved to be very viscous, which could hamper said impregnation. Lowering the Cu salt concentration from 100% saturation could facilitate template pore filling as well as allow for more nitrogen groups to coordinate to the Cu centers. The XRD and XPS results indicate that, for 4-BF4, 5-OTf, 6-OAc and 7-Acryl, Cu^0 particles were present (and in the case of 4-BF4, CuO particles). By increasing the nitrogen-to-copper ratio (i.e. diluting the precursor solution), the extra coordinating groups could help prevent agglomeration of copper species and trap the Cu^{2+} or Cu^+ ions within the graphitic sheets.

Lastly, it was observed during the HF etch that the solutions for 4-BF4, 5-OTf and 6-OAc turned blue. Indeed, by soaking them in distilled water for an hour after the HF etch resulted in blue solutions (Figure 41).

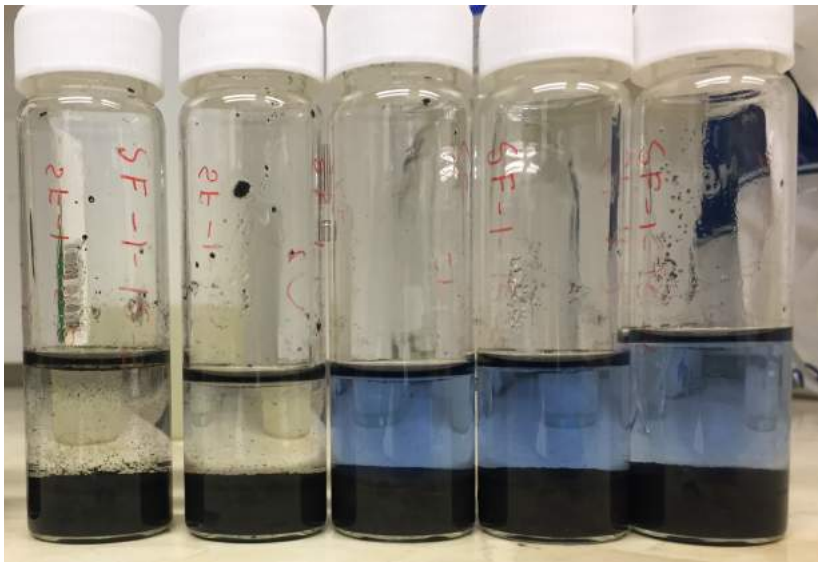

Figure 41. Picture of the water wash of OMCs. From left to right: 2-N, 3-Cl, 4-BF4, 5-OTf, and 6-OAc. For 1-O, 7-Acryl, and 8-Meth (not pictured), no blue solution was observed.

These tinted solutions indicate that there were soluble copper species not bound within the carbon framework of the OMCs. This could be attributed to a several factors. One, as stated before, lowering the concentration could allow for better incorporation of the copper ions into the graphitic sheets. Two, perhaps a 2 h carbonization time is not sufficient for complete conversion. If some organic polymer remains, the copper ions could leach out with a simple water wash. Three, the pretreatment with pTSA likely results in a simple proton transfer to the amine solvent. This lowers the number of free base amines to coordinate to the Cu ions. The pTSA treatment of the silica template was also found to greatly increase the likelihood of polymerization, many times prematurely before pore infiltration could occur. This, along with the time saved, provide additional reasons for foregoing this step.

In summary, the following changes were implemented for the synthesis of Cu-doped OMCs using highly soluble salts:

1. Carbonize individually
2. Lower concentration
3. Increase impregnation time for the solution into the template
4. Longer carbonization time
5. Skip pTSA pretreatment step
6. Wash the samples in water after the HF etch

Given the previous results, certain copper salts seem more amendable to the synthesis of doped carbons than others (Table 14).

Table 14. Comments on the feasibility of using each Cu-salt as a dopant

Salt	Comments
$CuCl_2$	Appears yield reasonably higher Cu-loadings in terms of the TGA burn off, but the lack of any detectable copper via XPS indicates little copper loading. Moreover, the low solubility limits the effect dilution could exert on the final OMC.
$Cu(BF_4)_2$-nH_2O	Gives good Cu-loadings in both TGA and XPS with very little exothermic reaction upon mixing with FNH_2. Very high solubility for dilution study. Boron incorporation into carbon yields important information on what happens to the anion upon carbonization.
$Cu(OTf)_2$	Also gives good Cu-loadings in both TGA and XPS, although not as high as $Cu(BF_4)_2$-nH_2O. Strong exothermic reactions when dissolved in FNH_2 is problematic; makes saturation hard to reach.
$Cu(OAc)_2$-H_2O	Extremely reactive solution in FNH_2. The premature polymerization when mixed with the silica template will prevent efficient pore filling. The unknown cause of the artificially high Cu loadings is concerning.
$Cu(acrylate)_2$	Limited solubility in FNH_2. Low loadings in both TGA and XPS.
$Cu(methacrylate)_2$	Higher solubility than $Cu(acrylate)_2$, but the low Cu-loadings in TGA and the lack of a Cu signal in XPS raise doubts on its effectiveness as a dopant salt.

Taking all of this into account, $Cu(BF_4)_2$-nH_2O was selected as the dopant salt for the next study due to its exceptionally high solubility, lack of any heat released when mixed with FNH_2, and its proven effectiveness as a dopant. A new synthesis procedure was drafted and is detailed in the experimental section of Study 3. This OMC procedure is referred to as Procedure 3 in this thesis.

6 Study 2: Copper salt concentration studies and finalization of OMC synthesis

6.1 Introduction: major changes to the OMC synthesis

Study 1 was the first endeavor into using various copper salts as dopants for OMCs. While none were tested in Li-S batteries, several important conclusions were obtained from the study, the majority of which deal with the Cu-OMC synthesis process. The major changes to this procedure are:

1. No pTSA pre-treatment of the silica.
2. Thoroughly drying the silica template before use.
3. A 16 h impregnation time after mixing the carbon precursor with the silica template. This is for both impregnations.
4. All sample carbonized individually to avoid cross-contamination.
5. Each carbonization time increased from 2 h to 4 h (1st carbonization) and to 6 h (2nd carbonization)
6. Washing with water after the HF etch to remove any soluble species from the surface.

The overall process is pictured in Figure 42 and is referred to as Procedure 3.

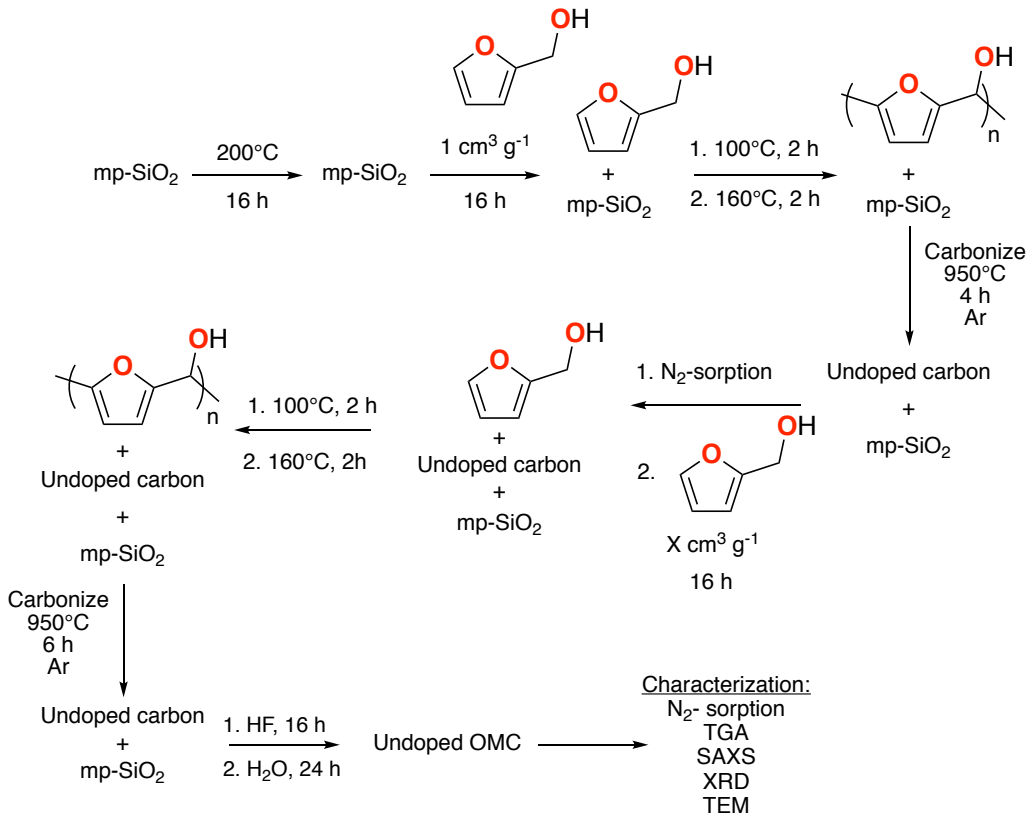

Figure 42. Overview of the OMC synthesis process using Procedure 3.

6.2 Experimental design

With the new steps for Procedure 3 determined, five new OMCs were synthesized: undoped, N-doped, and three with $Cu(BF_4)_2$-nH_2O doping at varying concentrations. The undoped and N-doped were made from neat reagents of FOH and FNH_2, respectively. The $Cu(BF_4)_2$-nH_2O salt solutions in FNH_2, this time, were varied in concentration. One solution was at saturation level; this solution was designated as 100%. Two more solutions were made from the saturated one, one at 75% saturation level and another at 50%. These were designated as such. Table 15 lists the five samples made using the new carbon synthesis.

Table 15. List of undoped, N-doped, and Cu-doped samples using the new synthesis method.

Carbon precursor	Copper salt	Concentration	Designation
FOH	None	N/A	Undoped
FNH_2	None	N/A	N-doped
FNH_2	$Cu(BF_4)_2$-nH_2O	100%	100% $Cu(BF_4)_2$
FNH_2	$Cu(BF_4)_2$-nH_2O	75%	75% $Cu(BF_4)_2$
FNH_2	$Cu(BF_4)_2$-nH_2O	50%	50% $Cu(BF_4)_2$

6.3 N_2-sorption results

As before, the synthesized Cu-OMCs were studied by N_2-sorption, XRD, TGA, and XPS. N_2-sorption was ran to see how these OMCs compared to the previous ones. The BET surface areas and BJH pore volumes are summarized in Table 16.

Table 16. Summary of N_2-sorption results in Study 2.

OMC	BET surface area (m^2 g^{-1})	BJH pore volume (cm^3 g^{-1})
Undoped	1449	1.80
N-doped	1371	2.01
100% $Cu(BF_4)_2$	582	1.18
75% $Cu(BF_4)_2$	596	1.23
50% $Cu(BF_4)_2$	631	1.19

As in Study 1, the $Cu(BF_4)_2$ doped OMCs exhibit a significantly lower surface area than their undoped and N-doped counter parts. The pore volumes are also much lower. Among the $Cu(BF_4)_2$ doped OMCs, there is a trend of increasing surface area with lowering the Cu salt concentration, which is consistent with the hypothesis stated in Section 5.3 that adding significant amounts of denser elements makes the overall density of the OMC higher, thereby lowering the specific surface area. No such trend was observed for the pore volume, however. Overall, for all samples, the N_2-sorption measurements show good replication of the silica template along with reasonable values for both surface area and pore volumes.

Additionally, it is important to see how the undoped and N-doped samples compare to the previous two procedures (Table 17 and Table 18). Excitingly, both the surface area and pore volumes for both samples appear to increase rather dramatically from either previous procedure; the values increase by at least a factor of two from the original procedure. Thus, the additional steps of a 16 h impregnation/mixing time combined with two separate carbonizations seem to dramatically enhance the surface properties.

Table 17. Comparison of BET surface areas ($m^2\ g^{-1}$)

Sample	Procedure 1	Procedure 2	Procedure 3
Undoped	653	1066	1449
N-doped	704	1082	1371

Table 18. Comparison of BJH pore volumes ($cm^3\ g^{-1}$)

Sample	Procedure 1	Procedure 2	Procedure 3
Undoped	0.986	1.14	1.80
N-doped	0.693	1.54	2.01

The samples with 100% salt concentration can also be compared between Procedures 2 and 3. In this case, however, no such drastic improvement was observed; both surface area and pore increased very modestly (Table 19). The high viscosity and/or reactivity of the copper salt-FNH_2 solution might explain these results. The viscosity limits the pore impregnation rate, so the increase in impregnation time from 2 to 24 h might have limited effect. Also, it was observed that upon storage at room temperature for 16 h, the samples turned from deep blue to brown, likely indicating polymerization of the FNH_2 solvent even before the sample was heated. The pore infiltration could be hampered by premature polymerization of the FNH_2 solvent.

Table 19. Comparison of surface characteristics of 100% $Cu(BF_4)_2$-nH_2O doped OMCs

Quantity	Procedure 2	Procedure 3	Change
BET surface area ($m^2\ g^{-1}$)	580	582	+0.34%
BJH pore volume ($cm^3\ g^{-1}$)	1.09	1.18	+8.26%

6.4 XRD results and TEM results

The XRD measurements showed some new and interesting results. To better identify any potential Cu species, the 2θ window was opened to 80 °2θ and the diffractograms are shown in (Figure 43). Along with the standard broad peaks for amorphous carbon, all $Cu(BF_4)_2$ OMCs exhibited the same XRD pattern with sharp diffraction peaks at 2θ values of 44°, 52°, and 74°, the first two of which were also observed in 4-BF4 and 6-OAc in Study 1 (Figure 36 and Figure 37).

These values match those of Cu^0 nanoparticles (Cu NPs). Interestingly, the peak at 37°, which is due to CuO, is still present, although at a reduced intensity. This indicates that using Procedure 3, with its much longer carbonization times, CuO is reduced almost entirely to Cu^0. The carbothermal reduction of Cu^{2+} to Cu^0 is nearly complete after a total of 10 hours of carbonization time.

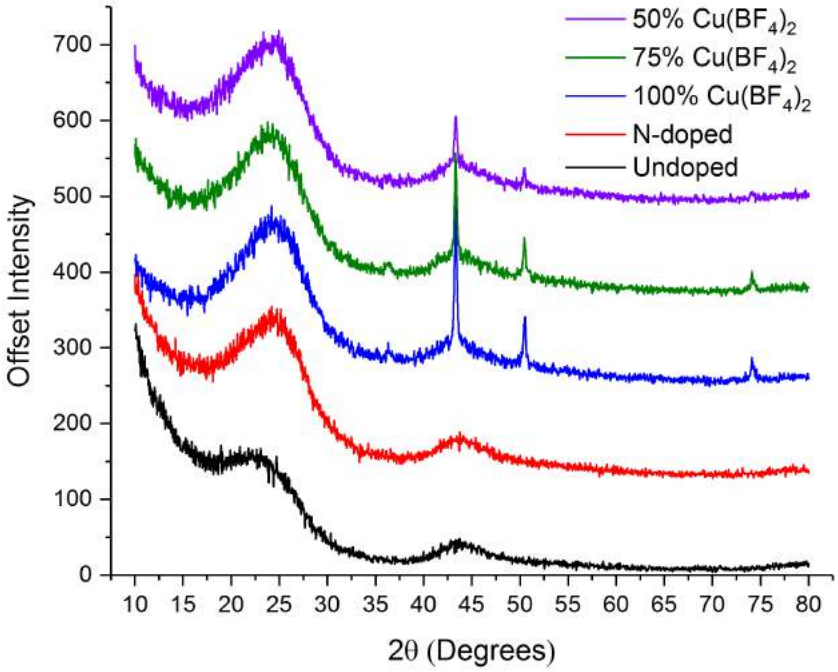

Figure 43. X-ray diffractograms of the five OMC samples made in Study 2. The diffraction peaks of the three $Cu(BF_4)_2$ samples correspond to Cu^0 particles.

The relative intensities of the Cu NP diffraction peaks also yield some valuable information. Focusing on the most intense peak at 44°, the relative intensities are in the order 100% > 75% > 50% when compared to the amorphous carbon peak at 25°. The ordering of intensities for the $Cu(BF_4)_2$ samples is what one would expect based on the concentration of copper salt used.

When the same OMCs were studied in TEM, crystalline particles with diameters around 30-40 nm were observed (Figure 44 and Figure 45). This corroborates the XRD findings in that crystalline nanoparticles are formed. Thus, the Cu^{2+} ions are carbothermally reduced to Cu^0 atoms, which then coalesce into Cu^0 nanoparticles. In Study 1, 4-BF4 exhibited much weaker diffraction peaks. The reason for this could be the increased carbonization time; more Cu^{2+} ions have the time to undergo reduction and find each other to form particles that are big enough to be seen in XRD.

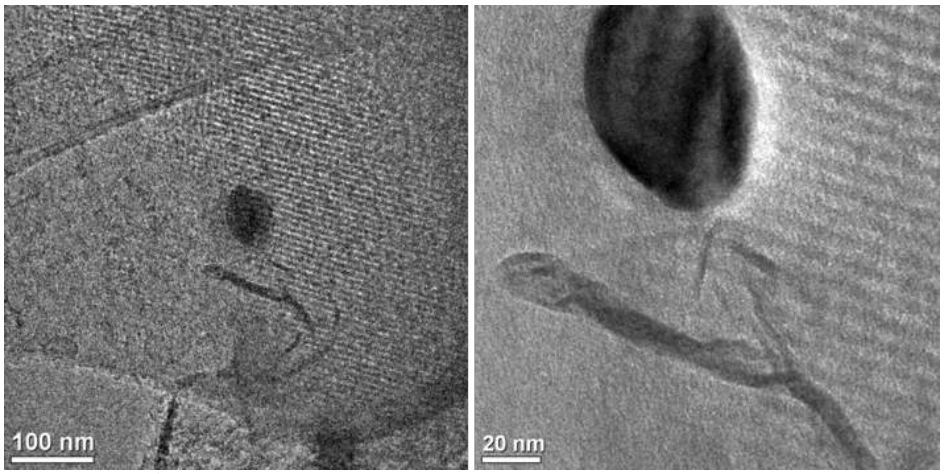

Figure 44. TEM images of Cu^0 nanoparticles in 100% $Cu(BF_4)_2$.

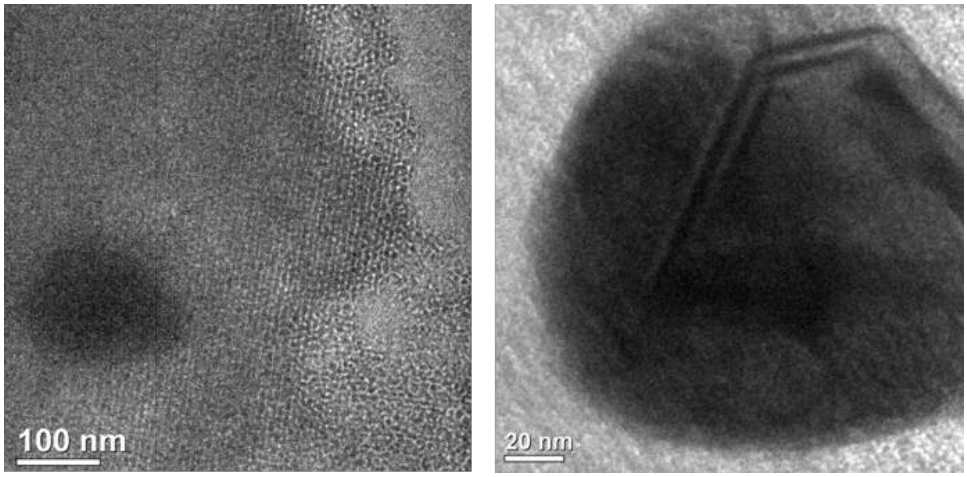

Figure 45. TEM images of Cu^0 nanoparticles in 75% $Cu(BF_4)_2$ (left) and 50% $Cu(BF_4)_2$ (right).

6.5 TGA results

The same TGA program as previously used was conducted on these samples to burn off all carbon and leave only the copper residue behind. The residual masses for the undoped and N-doped samples were negligible. This contrasts with 2-N in Study 1, where this sample had about a 1 wt% residual mass. Perhaps the final water wash helped to remove any remaining silica species from the carbon pores. As was assumed before, for the $Cu(BF_4)_2$ samples, all remaining mass was assumed to be copper residues, specifically CuO (Table 20). The residual masses are similar to those in Study 1, although a bit lower. After accounting for the water mass and O contribution, the final doping levels for these OMCs is in the range of 4.5 to 6.6 wt%. This is significantly higher than previous levels published by our group, which were in the range of 0.5 to 1.0 wt%.[15] An interesting finding is that the 75% sample was found to have slightly more Cu than the 100%, possibly indicating that more concentrated solutions do not always result in higher metal loadings.

Table 20. Residual masses as wt% and copper wt% calculations for Cu-OMCs.

Sample	Residual mass	CuO mass*	Cu mass§
Undoped	0.002	N/A	N/A
N-doped	0.004	N/A	N/A
100% $Cu(BF_4)_2$	6.9	7.5	6.0
75% $Cu(BF_4)_2$	7.7	8.3	6.6
50% $Cu(BF_4)_2$	5.3	5.7	4.5

**Corrected for hydration mass*

§Based on weight % of Cu in CuO (79.89%)

6.6 XPS results

XPS measurements were performed to compare the Cu loadings with those found by TGA. The atomic percentages for the Cu-doped samples are summarized in Table 21. The Cu-OMCs all show both B and Cu doping with relative concentrations in the order of what one would expect: 100% > 75% > 50%. The fact that more Cu was found for 100% than for 75% stands in contrast to the results from TGA. The fluorine levels were also rather high, which likely comes from the BF_4^- anion. Some small amounts of silicon were also found, meaning that the HF and water washes did not remove all silicate species.

Table 21. XPS atomic concentrations for $Cu(BF_4)_2$-nH_2O and $Cu(methacrylate)_2$ samples

Sample	B1s	C1s	N1s	O1s	F1s	Si2p	Cu2p3
100% $Cu(BF_4)_2$	2.99	82.00	6.78	5.64	1.43	0.34	0.82
75% $Cu(BF_4)_2$	1.90	85.77	6.03	4.30	1.51	0.14	0.34
50% $Cu(BF_4)_2$	0.87	88.41	5.47	3.78	1.15	0.18	0.15

6.7 Sulfur impregnation and battery testing

Because of their high Cu content, 100% and 75% $Cu(BF_4)_2$ were selected to testing in Li-S batteries. The sulfur impregnation of these OMCs was conducted using the procedure in Section 4.2, including the optional step for evaporation of surface sulfur. To gain an insight into the interaction between the added sulfur and the copper doping, XRD was performed again (Figure 46).

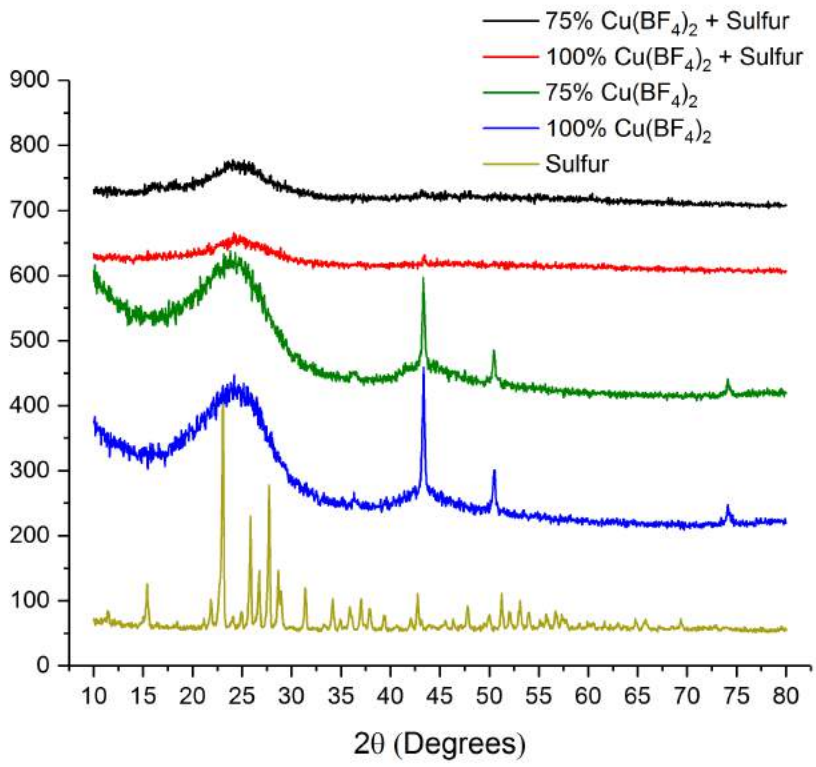

Figure 46. X-ray diffractograms of sulfur, the 100% and 75% $Cu(BF_4)_2$ OMCs, and the same OMCs impregnated with sulfur.

The addition of sulfur was found to greatly reduce the intensity of the amorphous carbon peaks with the one at 44° disappearing entirely. More importantly, the impregnation completely removed the diffraction peaks for the Cu NPs. Surprisingly, no other peaks were observed either including any for Cu_2S or CuS species. This is in contrast to other publications using Cu NP for stabilization of sulfur species, where the addition of sulfur was found to result in CuS_x peaks.[84] These results do not necessary indicate the lack of any CuS_x species, only the lack of crystalline ones. In principle, some amorphous or exceedingly small CuS_x particles could be present.

The sulfur-impregnated undoped, N-doped, and 100% $Cu(BF_4)_2$ OMCs were made into an electrode using the methods described in Section 4.3. Two batteries were made from each using the procedure described in Section 4.4. The batteries were cycled at 0.1 C for 100 cycles. The results are shown in Figure 47 -Figure 49 and are compared to the worst and best performing CMK3 electrodes from Figure 27 in Section 4.4 (cells 4 and 3, respectively).

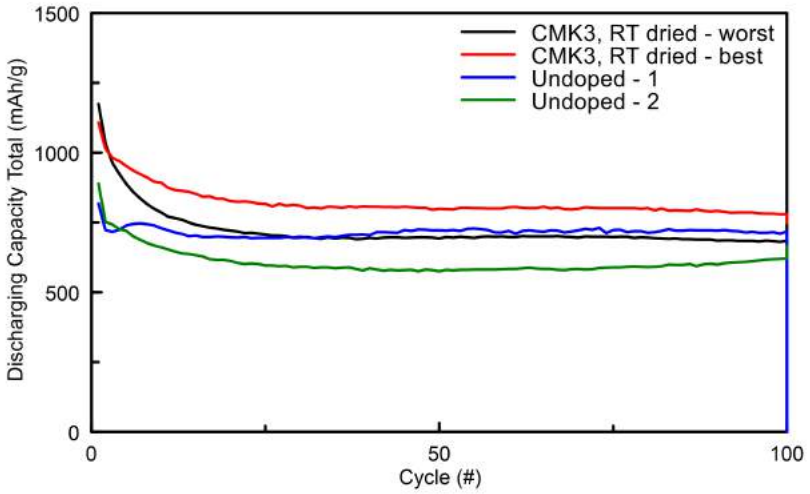

Figure 47. Cycling behavior of undoped OMCs.

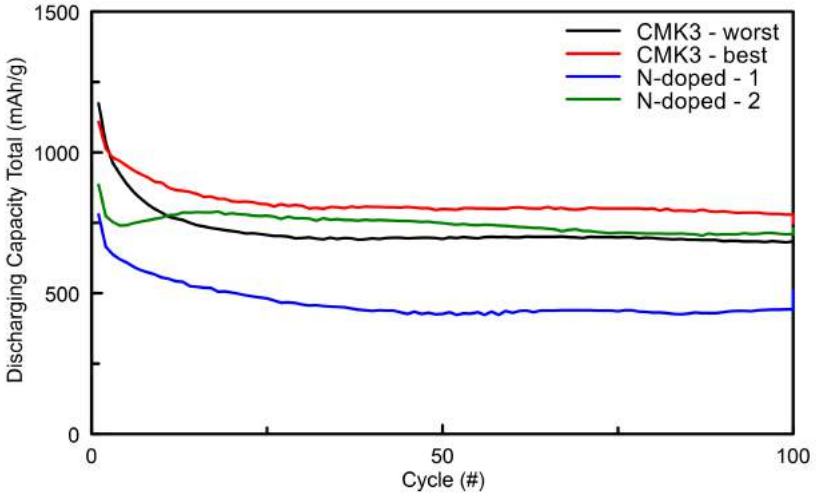

Figure 48. Cycling behavior of N-doped OMCs.

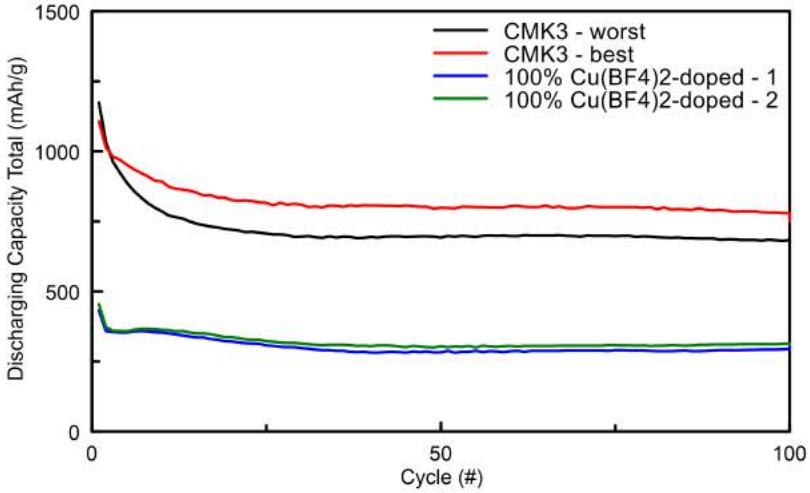

Figure 49. Cycling behavior of 100% $Cu(BF_4)_2$ doped OMCs.

The undoped and N-doped electrodes have one battery each that is within experimental error of the CMK3 batteries; thus, Procedure 3 yields OMCs that are competent hosts for sulfur. However, the cells made from 100% $Cu(BF_4)_2$ show a capacity exceptionally lower, at about one-half the level of any of the other OMCs. While some variance among batteries will always exist, the attenuation in performance is great enough such that one can definitely say that copper doping in these OMCs is detrimental for its use in Li-S batteries.

6.8 Washing studies

Clearly, something about the Cu-doping negatively impacts the battery performance. One possible explanation is that, during the carbonization process, a layer forms at the SiO_2-carbon interface. This layer has been reported before by our group and was observed to be non-porous.[85] An effective means of removing this layer or at least minimizing its effects in the context of PEMFCs was by heating the OMCs in 0.5 M sulfuric acid for 6 h at 80°C. The catalyst activity and, in turn the fuel cell performance increased. In this case, given the extremely concentrated salt solution, this layer could consist of incompletely carbonized polymer, copper/copper oxide particles, boron/fluorine residues, or some combination thereof. In any case, this layer likely hinders electron transfer from the OMC to the sulfur and/or reacts chemically with the sulfur during impregnation or battery cycling. In order to remove these species from the surface, a copper capturing reagent, sodium diethyldithiocarbamate, was employed. This molecule is routinely used to remove copper species from solution. Moreover, the anionic sulfur moieties in this molecule could mimic the PS, thereby removing any potential sulfur- or PS-reacting species from the OMC surface (Figure 50).

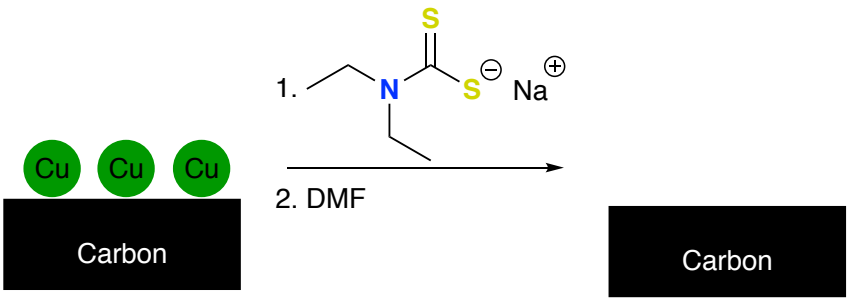

Figure 50. Illustration of how sodium diethyldithiocarbamate could remove the interfacial layer, here shown as Cu species, from the carbon surface.

The wash in sodium diethyldithiocarbamate, herein simply called carbamate, was performed as follows:

> The OMC was stirred overnight (16 h) in a 0.5 M aqueous carbamate solution at RT. The OMC was vacuum filtered and washed with copious amounts of water, then DMF, upon which a large amount of cloudy, brown particles were found to be removed from the carbon (Figure 51). The OMC was stirred overnight in DMF (16 h) to remove any more

contaminants, followed by filtering and washing with DMF, water, and ethanol, in that order. The OMC was dried overnight at 60°C in vacuum.

Figure 51. Picture of the filtrate after carbamate and DMF washes of the N-doped OMC (left) and the 75% $Cu(BF_4)_2$ doped OMC (right). The brown substance was believed to have been the non-porous surface layer.

When the N-doped OMC was washed in the same way, the brown filtrate was not observed. This brown substance could be the interfacial layer. For a control, the same wash procedure was conducted, but only with DMF. No brown filtrate was observed for any sample in this case. To see how these two washes affected the properties of the Cu-OMCs, the same tests of N_2-sorption, TGA, and XRD were ran. Only the 75% $Cu(BF_4)_2$ was studied since most of the 100% sample had been used in previous experiments. In N_2-sorption (Figure 52, left and center panels), the both carbamate washed and simple DMF washed caused little variation in either the surface area or pore volumes. The copper loadings by TGA were not heavily effected and the carbamate washed sample lost very little residual mass (Figure 52, right panel). Interestingly, the DMF-washed 75% $Cu(BF_4)_2$ was found to have a higher residual mass than before.

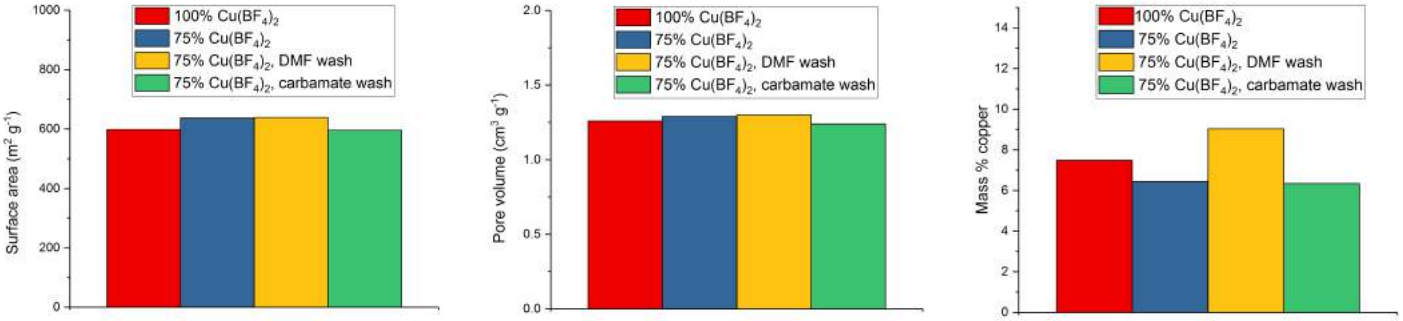

Figure 52. Comparison of the N_2-sorption and TGA results for 100% and 75 % $Cu(BF_4)_2$ as well as the 75% $Cu(BF_4)_2$ samples washed with the carbamate solution or DMF. No significant changes were observed upon either wash.

Importantly, in XRD, both washes were found to leave the Cu NP diffraction peaks unaffected. The relative intensity of the peaks, however, in particular those in the carbamate wash, lowered in relative intensity. Upon impregnation with S, all diffraction peaks disappeared as before (Figure 53).

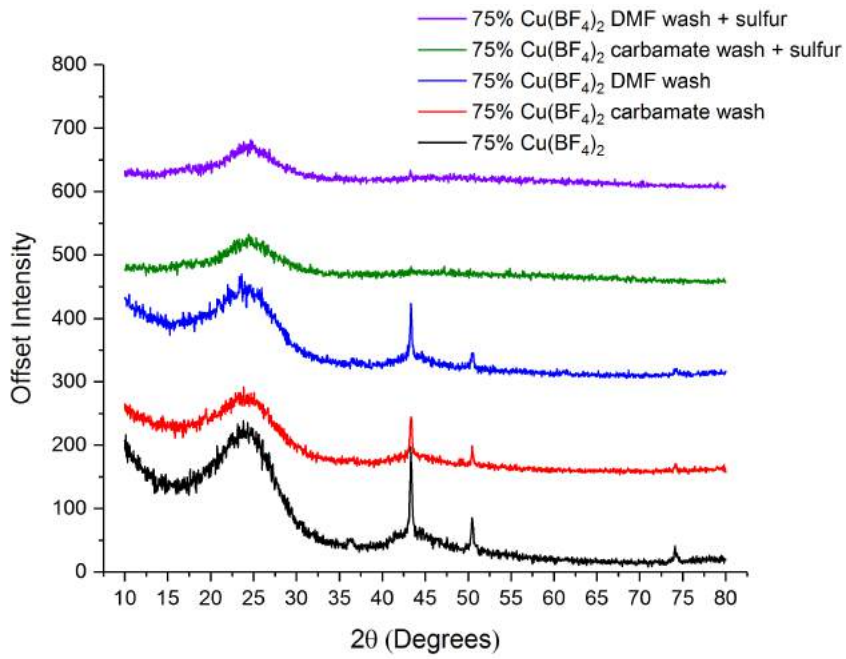

Figure 53. X-ray diffractograms of carbamate and DMF washed samples of 75% $Cu(BF_4)_2$ before and after sulfur impregnation.

Three coin-cells were made of each washed material. When tested in batteries, the various washes seemed to have little effect on the performance. The unwashed and DMF (Figure 54 and Figure 55) washed samples performed much worse than the CMK3 reference samples. The carbamate washed OMC (Figure 56) performed a little better than the other $Cu(BF_4)_2$-doped OMCs, especially cell 1, but still measurably worse than the worst performing CMK3 cell.

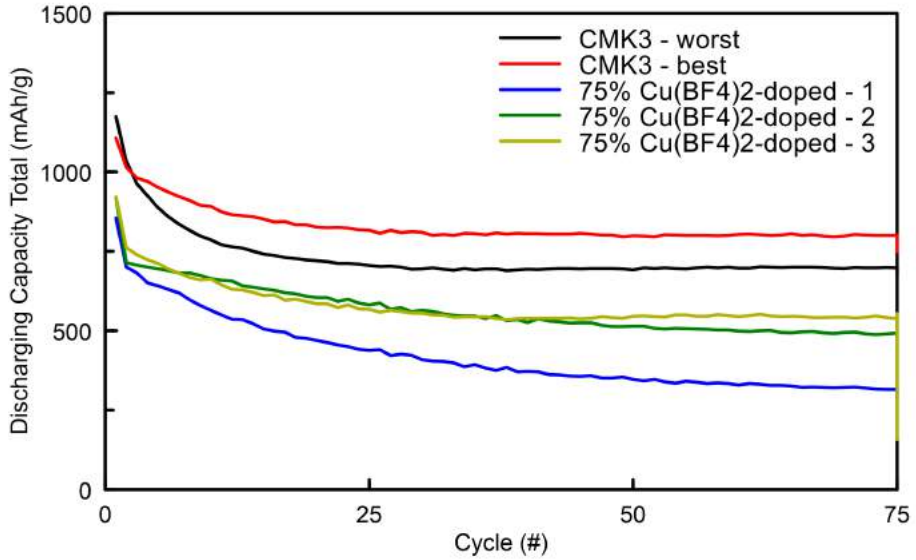

Figure 54. Cycling performance of $Cu(BF_4)_2$-doped OMCs.

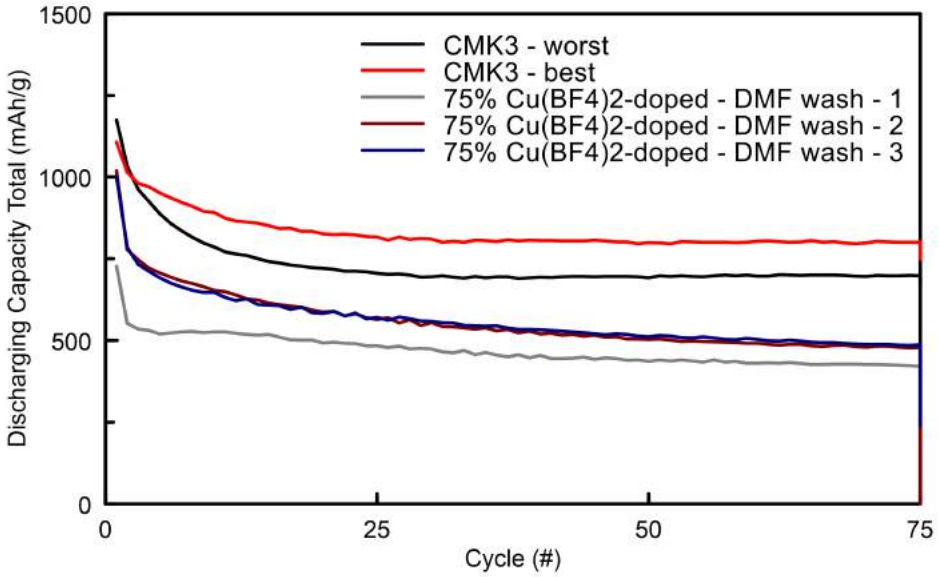

Figure 55. Cycling performance of DMF washed $Cu(BF_4)_2$-doped OMCs.

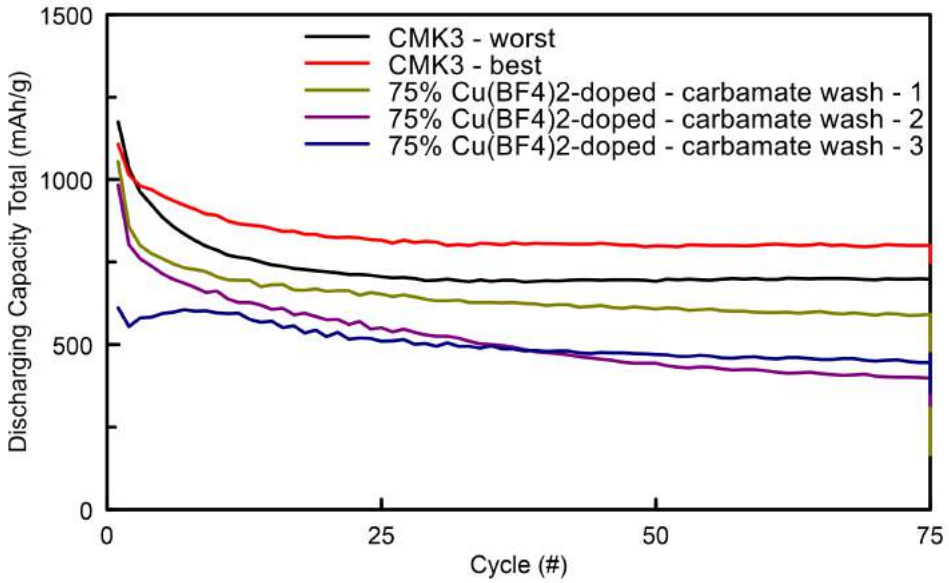

Figure 56. Cycling performance of carbamate washed $Cu(BF_4)_2$-doped OMCs.

One plausible explanation for this poor performance is the redox reaction between Cu and S before battery testing ever occurs. Sulfur reacts readily with copper, especially at elevated temperatures.[86] Since sulfur impregnation into the OMC occurs at 155°C then at 200°C, it is likely that this is hot enough to cause the two elements to react with each other, thereby forming CuS_x or copper-reduced sulfur. This reaction could explain the disappearance of the Cu NP diffraction peaks, although the lack of any CuS_x diffraction peaks is troubling. When battery discharge begins, the sulfur is already partially or completely reduced; therefore, it cannot contribute to the capacity. Since the cell does not gain capacity as it is charged and then cycled again, it is likely that this copper-reduced sulfur cannot be oxidized back to S_8. Overall, it is electrochemically "dead weight." As a control test, a small portion of the 100% $Cu(BF_4)_2$ C-S composite was subjected to Program 2 in TGA to evaporate all sulfur (Section 3.3.1) but the Cu NP diffraction peaks did not return (Figure 57).

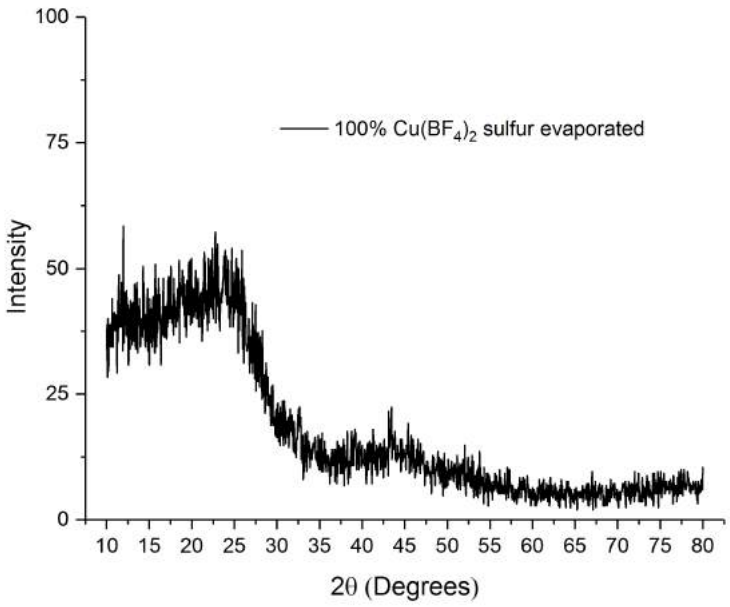

Figure 57. X-ray diffractogram of the 100% $Cu(BF_4)_2$ C-S composite with the sulfur evaporated.

6.9 Alternative sulfur impregnation method

A possible fix for this is to use an alternative sulfur impregnation method. Several methods exist that do not require heating sulfur past its melting point.[87-88] The new procedure selected was the sodium thiosulfate ($Na_2S_2O_3$) method, wherein the S_8 sulfur is produced in situ from disproportionation of aqueous $Na_2S_2O_3$ using HCl. The highest temperature employed in this method is 70°C, or about 50°C below sulfur's melting temperature. Small quantities (100 mg) of both 100% and 50% $Cu(BF_4)_2$ were washed with carbamate and were subjected to sulfur impregnation via the $Na_2S_2O_3$ method. The two new C-S composites were then studied by N_2-sorption to confirm pore filling. Both samples showed significantly reduced pore volumes (< 0.1 $cm^3\ g^{-1}$), confirming S_8 formation in the pore space. XRD was conducted to see how the Cu NP diffraction peaks were affected and so see if any S_8 resided outside of the pore space (Figure 58). In the case of 50% $Cu(BF_4)_2$, the Cu NP diffraction peaks disappeared, but with no reappearance of any CuS_x species. For 100% $Cu(BF_4)_2$, no Cu NP diffraction peaks were observed either and strong S_8 peaks were present. Since the previous results indicated that the disappearance of the Cu NP diffraction peaks leads to poor battery performance, it was determined that the same copper-sulfur reaction had happened and that battery testing was not worth the time or effort. Moreover, the presence of S_8 peaks is known to yield inferior electrodes.[73] It was at this point that this portion of the project was abandoned due to time concerns.

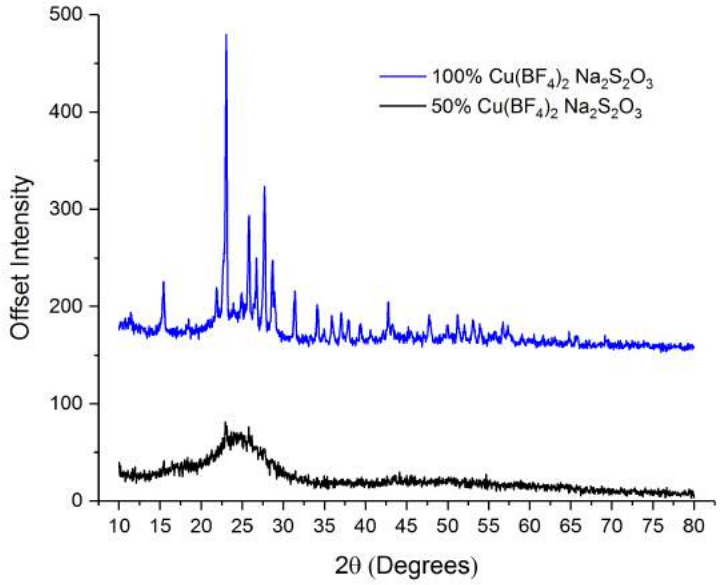

Figure 58. X-ray diffractograms of Cu(BF4)2-doped OMCs impregnated with sulfur using the $Na_2S_2O_3$ method.

6.10 Testing as catalysts for O_2 reduction

While deleterious for battery performance, the high Cu-loadings in these OMCs could serve well in other applications. Cu complexes and Cu NPs have been shown to catalyze the reduction of small molecules, e.g. O_2 to H_2O.[89-90] Small quantities of the 75% $Cu(BF_4)_2$ OMCs of each wash were mixed into inks and drip coated onto glass carbon electrodes for studies on RDE. The procedure for drip coating is detailed in the experimental section of Study 3.

The reductions on RDE were ran in one atmosphere O_2 with constant gas purging during the entire experiment. The electrolyte was 0.1 M $HClO_4$ and the rotation rate was 900 rpm. The results are shown in Figure 59.

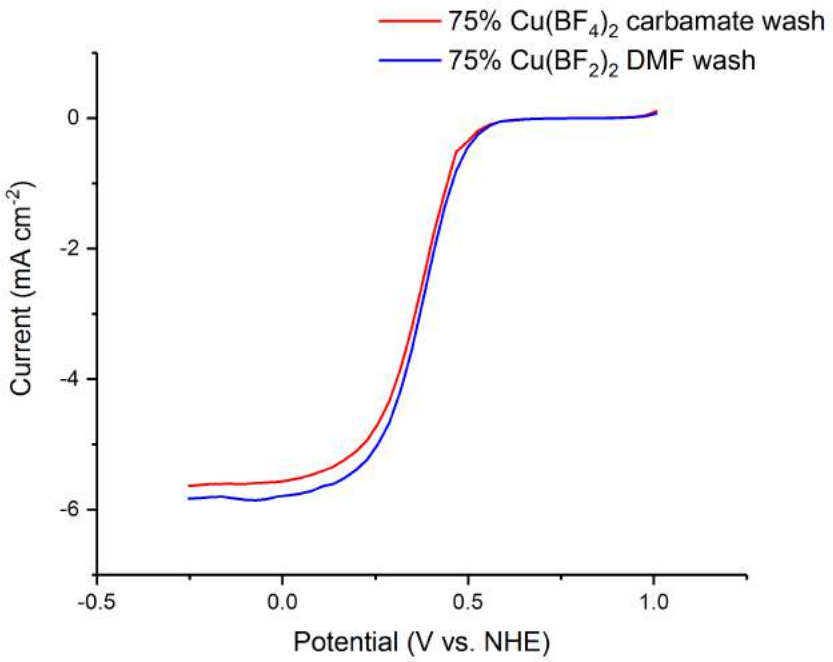

Figure 59. RDE of O_2 reduction on $Cu(BF_4)_2$ with two different washes.

The results for O_2 reduction for both washes show an $E_{1/2}$ at approximately 0.38 V vs. NHE, which is 0.79 V lower than the thermodynamic voltage of 1.17 V at this pH. For reference, a good performing Fe-doped OMC from study 3, the one derived from $FeCl_3$-$6H_2O$ shows a of 0.67 V under the same conditions. Thus, this Cu-doped OMC does not efficiently catalyze the ORR.

6.11 Conclusions from the Cu-OMC studies

In some ways, the efforts into doping OMCs with highly soluble copper salts was a success; in others, it was not. The final metal loadings in the final OMC can be raised far above the typical 0.5 to 1.0 wt% to levels in the range of 5 to 10 wt%. Ultimately, however, this extra metal within the carbon structure seemed to severely hurt the battery performance and provided poor catalysis towards O_2 and CO_2 reduction.

A main contribution to the poor performance in both applications is likely due to the reduction of Cu^{2+} to Cu^0 during carbonization. Copper was chosen for its ability to act as a soft Lewis acid, but its propensity for reduction seems to negate any potential benefit of this dopant. The reduction potential for Cu^{2+} is shown in Table 22 along with some of the other first row transition metals.

Table 22. Reduction potentials of first row transition metals.

Redox couple	Standard Reduction potential (V vs. NHE)
$Cu^{2+} + 2e^- \rightarrow Cu$	+0.3419
$Ni^{2+} + 2e^- \rightarrow Ni$	-0.257
$Co^{2+} + 2e^- \rightarrow Co$	-0.28
$Mn^{2+} + 2e^- \rightarrow Mn$	-1.185
$Fe^{2+} + 2e^- \rightarrow Fe$	-0.447

The reduction of Cu^{2+} is considerably more favorable than any of these other M^{2+} ions. More importantly, however, is that this facile reduction is then accompanied by agglomeration into relatively large particles. Thus, instead of having the metal centers efficiently dispersed throughout the carbon matrix and available for sulfur binding or O_2/CO_2 reduction, they coalesce into large particles and lower the number of available atoms on the particle surface. Being encased within a carbon shell further lowers the surface area of these particles. In the case of Li-S batteries, the copper particles can reduce the sulfur, which lowers the amount of electrochemically available sulfur and the resulting CuS_x species provide insulation for electron transfer.

Going forward with this project, a different metal ion should be chosen, but some information can be gained with respect to which anion to use. The BF_4^- anion seemed to help the carbon maintain a high metal loading in both Cu-doped OMC studies whereas other anions proved too reactive towards FNH_2 or resulted in low Cu-loadings. Study 3 used some of the corresponding salts for Fe and in the context of PEMFCs and O_2 reduction. Other candidate metal salts include $Co(BF_4)_2$-$6H_2O$ and $Ni(BF_4)_2$-$6H_2O$, both of which should resist reduction to Co^0 or Ni^0. Changing other factors of the synthesis process other than the metal ion could help prevent reduction and keep the metal ions well dispersed throughout the carbon skeleton as surface-accessible catalytic centers: raising the level of nitrogen doping by adding extra N-dopants or a different carbon precursor, lowering the salt concentration, or lowering the carbonization temperature.

7 Study 3: Fe-doped OMCs

The concept for this study is qualitatively similar to Studies 1 and 2 with Cu-OMCs but with a different metal ion and a different application. In this study, Fe was chosen as the dopant since many studies have shown that Fe and Co are the most adept at the ORR, as discussed briefly in Section 2.1.5.[36, 42-43] The selection of anions, however, was kept the same as for the Cu-OMCs with the same goal of increasing the final metal loading of the iron-doped OMCs (Fe-OMCs). The background, experimental details, and results are detailed in Manuscript 1.

To summarize the results of Study 3, three organic-soluble iron salts were selected as non-standard iron dopants: $Fe(OAc)_2$, $Fe(OTf)_2$, $Fe(BF_4)_2$-$6H_2O$ in addition to the more common $FeCl_3$-$6H_2O$. The Fe-OMCs are identified by their anion in the form X-Fe-OMC. As with the corresponding Cu salts, these Fe salts show much greater solubility in FNH_2 than the standard chloride salt. In the case of OTf-Fe-OMC and BF4-Fe-OMC, much larger residual masses in TGA were observed (Program 1, Section 3.3.1), but their performance in PEMFCs was only marginal. OAc-Fe-OMC, had a smaller residual mass than Cl-Fe-OMC and had the worst performance of all Fe-OMCs studied, likely due to its lower nitrogen content and presumably a lower Fe loading. We use a host of techniques including XRD, N_2-sorption, TGA, SAXS, RDE, and EPR to try and elucidate what effect the anions have on the Fe-OMC synthesis. Overall, the anions have a strong influence on the resultant Fe-OMC structure and, more importantly, on the *type* of iron contained within the Fe-OMC scaffold.

8 Study 4: Bromomethylation of carbon materials

Study 4 represents a completely new direction for this thesis. In place of making carbons using the bottom-up synthesis with silica templating, this study focuses on taking a preformed carbon and modifying its surface using organic chemistry. As discussed in Section 2.2, several methods already exist for modifying carbon surfaces including surface oxidation and diazonium coupling. More recently, azide-modified carbons have been studied by using iodine azide (IN_3) in the solution[90-91] or in the gas phase.[92] All of these, however, have moderate to severe drawbacks: destruction of the carbon's structure, loss of porosity and/or electrical conductivity, formation of surface multilayers resulting in pore clogging and easily detached groups, and instability of grafted surface groups. In Study 4, we introduce a new method for surface functionalization of carbon materials: the bromomethylation reaction. This reaction can be applied to a wide range of carbons and exhibits none of the previously mentioned drawbacks. The details of this reaction mechanism, its scope, and versatility are detailed in Manuscript 2.

Overall, we found that the selective reactivity of the bromomethylated carbons was well represented by the fact that a wide variety of nucleophiles could substitute bromide on the carbon surface when treated at elevated temperatures overnight. Otherwise, the bromomethyl groups are very stable when stored at room temperature under ambient conditions. This flexible platform for surface functionalization was very suitable for creating modified carbons for use as the carbon additives in sulfur cathodes for Li-S batteries. We selected two amines - diallylamine (All_2NH) and ethylenediamine (EN) – as the nucleophiles. Cathodes using these amine-functionalized carbons yielded improved performance relative to their unfunctionalized predecessors, although this improvement decreased with increased cycling.

9 Conclusions and Future Work

The results from Studies 1, 2, and 3 point to the importance of taking both the cation and anion of the dopant metal salt into account when designing a synthesis for transition metal-doped OMCs. For both Cu and Fe dopant salts, the anion has a strong impact on the resulting OMC structure, its metal loading, the type of metal species contained within the carbon structure, and its performance in PEMFCs (in the case of Fe). We discovered that creating Cu-OMCs was rather difficult since all copper species contained within the OMCs seemed to be either CuO or Cu^0 particles, the latter of which forms due to the fact that Cu^{2+} ions are relatively easy to reduce to Cu^0, which then coalesce into Cu NPs with diameters of about 40-50 nm. The Cu NPs seem to impart no benefit to the carbon material either in terms of Li-S batteries or catalytic activity in the ORR. In fact, they seem to be severely deleterious to Li-S battery performance, which is likely due to a reaction between Cu and S to form an electro-inactive CuS_x species. No such species was ever detected via XRD, however. While various synthesis parameters could be changed to possibly avoid Cu NP formation, the ease with which Cu ions reduce under carbonization conditions will likely prevent any copper ion chelates (i.e. CuN_x) from being formed within the carbon structure. *Perhaps the main conclusion to draw from Studies 1 and 2 is that certain metal ions, regardless of the counter anion, are simply not amenable for doping carbon materials.* That is, at least using the synthesis conditions used here. Such syntheses might be limited to less noble metals to avoid *in-situ* reduction. In the case of the Fe-OMCs, changing the anion from chloride to more organic-soluble salts produced competent, but not great, Fe-OMCs in terms of their performance in PEMFCs. Unlike the Cu-OMCs, however, changing the synthesis conditions could improve the Fe-OMC performance since Fe ions are much harder to reduce. Future studies will focus on how to transform more of the dissolved Fe ions from the organic-soluble salts in FNH_2 solution into more of the catalytically active Fe species. Likewise, other studies will concentrate on what conditions lead to said Fe species and how to identify them spectroscopically (i.e. EPR, solid-state NMR) using isotopically labeled FNH_2 and Fe salts.

With respect to Study 4, the bromomethylation reaction likely has a very bright future. This method of grafting organic functionality to carbon surfaces seems to have all the advantages and none of the disadvantages compared to other grafting methods. More importantly, the facile derivatization of the bromomethyl groups allows for a diverse array of functional groups to be attached to the surface, thereby allowing this reaction to find use in many applications. So far, it has been applied to the Li-S system using two amines, but other groups could just as easily be used. For example, by tethering Fe complexes to the carbon surface, such carbons could find great utility in PEMFCs. Another use could be to functionalize the carbon surface with redox active molecules (e.g. ferrocene, quinones), which could supply pseudocapacitance for supercapacitors. The inherent advantage of such grafting methods over the bottom-up carbon syntheses used in Studies 1, 2, and 3 is that more delicate functional groups can be chosen to create materials specifically tailored for the application in question. It is also much quicker and easier. Future studies will explore the multitude of possibilities for this two-step functionalization scheme.

10 Acknowledgements

This licentiate thesis has been carried out with gratefully acknowledged financial support from the Swedish Energy Agency (Energimyndigheten) for project 37671-1.

First and foremost, I need to thank my supervisor, Professor Anders Palmqvist, for his advice and guidance over the past three and half years. When I received his invitation to start my PhD at 1 AM local time in Colorado, I knew that I was about to start a great adventure! I also would like to thank my group members in chemistry, past and present: Giulio, Milene, Andrey, Yifei, Caroline, Gunnar, Joakim, Walter, Björn, Richard, Florian, Samrand, and Ma Yi. You all have made working at Chalmers a very fun experience. Many other people in chemistry (TYK) have also made these past years quite memorable who are too many to list here. I would like to extend a special thank you to my officemate and friend, Gunnar, for his advice and many conversations over the past several years.

There is also the group in physics (KMF) that I would like to thank, especially Patrik Johansson and my co-supervisor, Professor Aleksandar Matic. I would like to extend my gratitude to all of the various KMF members throughout the years for your help and support with all things battery related.

I would like to thank my examiner, Professor Hanna Härelind, for her advice and help with my thesis. I need to extend a special thanks to Professors Gunnar Westman and Peter Enoksson for reading my thesis and serving as my opponents.

I would like to take the time to thank the post-docs who took it upon themselves to help me with my projects and serve as my scientific mentors: Florian “Den Stora” Nitze, Muhammed “Master” Abdelhamid, and Marco “The Godfather” Agostini. I also would like to send a special thanks to Caroline and Walter for their help with the first manuscript (Study 3).

I need to thank my former supervisor at Stanford University, Professor Daniel Stack, for the opportunity to work on the bromomethylation project (Study 4). I am super happy our two groups could collaborate on this project! Along these same lines, I need to thank my friend and former labmate, Christopher Lyons, for his work with this topic. Also on this project were Ella Levin and my former co-supervisor, Professor Christopher Chidsey. Thank you for your effort in this endeavor.

I would also like to say thank you for my first research advisor, Professor David Hart, at The Ohio State University. I will always be grateful to him for allowing a complete novice of an undergraduate work in his lab conducting studies in synthetic organic chemistry. As it turns out, a lot of organic chemistry reactions can be run on carbon surfaces!

From my Overland High School days in Colorado, I would like to thank my teachers Marilyn Kemp (chemistry) and Rodney McKinney (math and computer science) for their continued support and advice, despite my graduation over ten years ago. I need to give a special thanks to my speech therapist, Kathleen Chase. Without her help, I would not be where I am today.

Looking to the future, I would like to thank Professors Russell Varley, Jenny Pringle, Patrick Howlett, and Maria Forsyth for the opportunity to study in Australia at Deakin University. I look forward to working with you all.

Lastly, of course, I need to thank my friends and family back in the US for their continued help in spite of the distance between us. Thank you mom, dad, Zach, and Emily for your help and advice throughout these years. I would also like to thank all of my friends and family back in Colorado, Ohio, and California and elsewhere for their continued friendship.

Peace, love, and chemistry,
Samuel J. Fretz

11 References

1. Carbon. In *Chemistry of the Elements*, Greenwood, N. N.; Earnshaw, A., Eds. Butterworth-Heinemann: Oxford, 1997; pp 268-327.
2. BBC NEWS | Science/Nature | Chinese made first use of diamond. http://news.bbc.co.uk/2/hi/science/nature/4555235.stm.
3. Krogt, P. v. d., 6. Carbonium (Carbon) - Elementymology & Elements Multidict. **2017**.
4. Ströck, M., Eight allotropes of carbon. **2006**.
5. Natural Graphite | Asbury Carbons. https://asbury.com/technical-presentations-papers/materials-in-depth/natural-graphite/.
6. King, H. How Do Diamonds Form? | They Don't Form From Coal! http://geology.com/articles/diamonds-from-coal/.
7. Bundy, F. P., Pressure-Temperature Phase-Diagram of Elemental Carbon. *Physica A* **1989,** *156* (1), 169-178.
8. Kinoshita, K., *Carbon : electrochemical and physicochemical properties*. Wiley: New York, 1988; p xiii, 533 p.
9. Jenkins, G. M.; Kawamura, K., Structure of glassy carbon. *Nature* **1971,** *231* (5299), 175-6.
10. Sun, F.; Wang, J.; Chen, H.; Li, W.; Qiao, W.; Long, D.; Ling, L., High efficiency immobilization of sulfur on nitrogen-enriched mesoporous carbons for Li-S batteries. *ACS Appl Mater Interfaces* **2013,** *5* (12), 5630-8.
11. Kicinski, W.; Szala, M.; Bystrzejewski, M., Sulfur-doped porous carbons: Synthesis and applications. *Carbon* **2014,** *68*, 1-32.
12. Kleitz, F.; Choi, S. H.; Ryoo, R., Cubic Ia3d large mesoporous silica: synthesis and replication to platinum nanowires, carbon nanorods and carbon nanotubes. *Chem Commun (Camb)* **2003,** (17), 2136-7.
13. Li, R.; Ge, Y. J.; He, F.; Dou, L. T.; Liu, B. H.; Li, Z. P., Prevention of active-site destruction during the synthesis of high performance non-Pt cathode catalyst for fuel cells. *Rsc Adv* **2017,** *7* (11), 6622-6630.
14. Pampel, J.; Fellinger, T. P., Opening of Bottleneck Pores for the Improvement of Nitrogen Doped Carbon Electrocatalysts. *Adv Energy Mater* **2016,** *6* (8).
15. Dombrovskis, J. K.; Jeong, H. Y.; Fossum, K.; Terasaki, O.; Palmqvist, A. E. C., Transition Metal Ion-Chelating Ordered Mesoporous Carbons as Noble Metal-Free Fuel Cell Catalysts. *Chem Mater* **2013,** *25* (6), 856-861.
16. Nitze, F.; Fossum, K.; Xiong, S. Z.; Matic, A.; Palmqvist, A. E. C., Sulfur-doped ordered mesoporous carbons: A stability-improving sulfur host for lithium-sulfur battery cathodes. *J Power Sources* **2016,** *317* (Supplement C), 112-119.
17. Li, Z.; Yin, L., Nitrogen-doped MOF-derived micropores carbon as immobilizer for small sulfur molecules as a cathode for lithium sulfur batteries with excellent electrochemical performance. *ACS Appl Mater Interfaces* **2015,** *7* (7), 4029-38.
18. Paraknowitsch, J. P.; Thomas, A., Functional Carbon Materials From Ionic Liquid Precursors. *Macromol Chem Phys* **2012,** *213* (10-11), 1132-1145.
19. Shen, W. Z.; Fan, W. B., Nitrogen-containing porous carbons: synthesis and application. *J Mater Chem A* **2013,** *1* (4), 999-1013.

20. Song, J. X.; Xu, T.; Gordin, M. L.; Zhu, P. Y.; Lv, D. P.; Jiang, Y. B.; Chen, Y. S.; Duan, Y. H.; Wang, D. H., Nitrogen- Doped Mesoporous Carbon Promoted Chemical Adsorption of Sulfur and Fabrication of High- Areal- Capacity Sulfur Cathode with Exceptional Cycling Stability for Lithium-Sulfur Batteries. *Adv Funct Mater* **2014,** *24* (9), 1243-1250.
21. Bo, X.; Guo, L., Ordered mesoporous boron-doped carbons as metal-free electrocatalysts for the oxygen reduction reaction in alkaline solution. *Phys Chem Chem Phys* **2013,** *15* (7), 2459-65.
22. Xia, L.; Zhong, B.; Zhang, T.; Hu, X. T.; Wu, S. S.; Yang, J.; Wen, G. W., Effect of boron doping on the thermal properties of carbon fibers reinforced lithium aluminosilicate matrix composites. *J Eur Ceram Soc* **2015,** *35* (9), 2555-2562.
23. Xie, Y.; Meng, Z.; Cai, T.; Han, W. Q., Effect of Boron-Doping on the Graphene Aerogel Used as Cathode for the Lithium-Sulfur Battery. *ACS Appl Mater Interfaces* **2015,** *7* (45), 25202-10.
24. Yang, C. P.; Yin, Y. X.; Ye, H.; Jiang, K. C.; Zhang, J.; Guo, Y. G., Insight into the effect of boron doping on sulfur/carbon cathode in lithium-sulfur batteries. *ACS Appl Mater Interfaces* **2014,** *6* (11), 8789-95.
25. Wang, H. M.; Wang, H. X.; Chen, Y.; Liu, Y. J.; Zhao, J. X.; Cai, Q. H.; Wang, X. Z., Phosphorus-doped graphene and (8,0) carbon nanotube: Structural, electronic, magnetic properties, and chemical reactivity. *Appl Surf Sci* **2013,** *273*, 302-309.
26. Yang, D. S.; Bhattacharjya, D.; Inamdar, S.; Park, J.; Yu, J. S., Phosphorus-doped ordered mesoporous carbons with different lengths as efficient metal-free electrocatalysts for oxygen reduction reaction in alkaline media. *J Am Chem Soc* **2012,** *134* (39), 16127-30.
27. Nitze, F.; Fossum, K.; Xiong, S. Z.; Matic, A.; Palmqvist, A. E. C., Sulfur-doped ordered mesoporous carbons: A stability-improving sulfur host for lithium-sulfur battery cathodes. *J Power Sources* **2016,** *317*, 112-119.
28. See, K. A.; Jun, Y. S.; Gerbec, J. A.; Sprafke, J. K.; Wudl, F.; Stucky, G. D.; Seshadri, R., Sulfur-functionalized mesoporous carbons as sulfur hosts in Li-S batteries: increasing the affinity of polysulfide intermediates to enhance performance. *ACS Appl Mater Interfaces* **2014,** *6* (14), 10908-16.
29. Ma, Z. F.; Xie, X. Y.; Ma, X. X.; Zhang, D. Y.; Ren, Q. Z.; Hess-Mohr, N.; Schmidt, V. M., Electrochemical characteristics and performance of CoTMPP/BP oxygen reduction electrocatalysts for PEM fuel cell. *Electrochem Commun* **2006,** *8* (3), 389-394.
30. Pylypenko, S.; Mukherjee, S.; Olson, T. S.; Atanassov, P., Non-platinum oxygen reduction electrocatalysts based on pyrolyzed transition metal macrocycles. *Electrochim Acta* **2008,** *53* (27), 7875-7883.
31. Vanveen, J. A. R.; Vanbaar, J. F.; Kroese, C. J.; Coolegem, J. G. F.; Dewit, N.; Colijn, H. A., Oxygen Reduction on Transition-Metal Porphyrins in Acid Electrolyte .1. Activity. *Ber Bunsen Phys Chem* **1981,** *85* (8), 693-700.
32. Vanveen, J. A. R.; Vanbaar, J. F.; Kroese, K. J., Effect of Heat-Treatment on the Performance of Carbon-Supported Transition-Metal Chelates in the Electrochemical Reduction of Oxygen. *J Chem Soc Farad T 1* **1981,** *77*, 2827-2843.
33. Ziegelbauer, J. M.; Olson, T. S.; Pylypenko, S.; Alamgir, F.; Jaye, C.; Atanassov, P.; Mukerjee, S., Direct spectroscopic observation of the structural origin of peroxide generation from co-based pyrolyzed porphyrins for ORR applications. *J Phys Chem C* **2008,** *112* (24), 8839-8849.

34. Faubert, G.; Lalande, G.; Cote, R.; Guay, D.; Dodelet, J. P.; Weng, L. T.; Bertrand, P.; Denes, G., Heat-treated iron and cobalt tetraphenylporphyrins adsorbed on carbon black: Physical characterization and catalytic properties of these materials for the reduction of oxygen in polymer electrolyte fuel cells. *Electrochim Acta* **1996,** *41* (10), 1689-1701.
35. Vanveen, J. A. R.; Visser, C., Oxygen Reduction on Monomeric Transition-Metal Phthalocyanines in Acid Electrolyte. *Electrochim Acta* **1979,** *24* (9), 921-928.
36. Wiesener, K.; Ohms, D.; Neumann, V.; Franke, R., N-4 Macrocycles as Electrocatalysts for the Cathodic Reduction of Oxygen. *Mater Chem Phys* **1989,** *22* (3-4), 457-475.
37. Bron, M.; Radnik, J.; Fieber-Erdmann, M.; Bogdanoff, P.; Fiechter, S., EXAFS, XPS and electrochemical studies on oxygen reduction catalysts obtained by heat treatment of iron phenanthroline complexes supported on high surface area carbon black. *J Electroanal Chem* **2002,** *535* (1-2), 113-119.
38. Lefevre, M.; Proietti, E.; Jaouen, F.; Dodelet, J. P., Iron-based catalysts with improved oxygen reduction activity in polymer electrolyte fuel cells. *Science* **2009,** *324* (5923), 71-4.
39. Burgess, J., *Metal Ions in Solution*. Ellis Horwood LTD: 1978.
40. Krossing, I.; Raabe, I., Noncoordinating anions--fact or fiction? A survey of likely candidates. *Angew Chem Int Ed Engl* **2004,** *43* (16), 2066-90.
41. Chan, C.-Y., *Alkali metal and ammonium perchlorates: part 1: lithium and sodium perchlorates*. Oxford University Press: 1995.
42. Ohms, D.; Herzog, S.; Franke, R.; Neumann, V.; Wiesener, K.; Gamburcev, S.; Kaisheva, A.; Iliev, I., Influence of Metal-Ions on the Electrocatalytic Oxygen Reduction of Carbon Materials Prepared from Pyrolyzed Polyacrylonitrile. *J Power Sources* **1992,** *38* (3), 327-334.
43. Faubert, G.; Cote, R.; Dodelet, J. P.; Lefevre, M.; Bertrand, P., Oxygen reduction catalysts for polymer electrolyte fuel cells from the pyrolysis of Fe-II acetate adsorbed 3,4,9,10-perylenetetracarboxylic dianhydride. *Electrochim Acta* **1999,** *44* (15), 2589-2603.
44. Miessler, G. L. T. D. A., *Inorganic Chemistry, Third Edition*. Pearson Prentice Hall: 2004.
45. Otake, Y.; Jenkins, R. G., Characterization of Oxygen-Containing Surface Complexes Created on a Microporous Carbon by Air and Nitric-Acid Treatment. *Carbon* **1993,** *31* (1), 109-121.
46. Vinke, P.; van der Eijk, M.; Verbree, M.; Voskamp, A. F.; van Bekkum, H., Modification of the surfaces of a gasactivated carbon and a chemically activated carbon with nitric acid, hypochlorite, and ammonia. *Carbon* **1994,** *32* (4), 675-686.
47. Pradhan, B. K.; Sandle, N. K., Effect of different oxidizing agent treatments on the surface properties of activated carbons. *Carbon* **1999,** *37* (8), 1323-1332.
48. Chen, X.; Farber, M.; Gao, Y. M.; Kulaots, I.; Suuberg, E. M.; Hurt, R. H., Mechanisms of surfactant adsorption on non-polar, air-oxidized and ozone-treated carbon surfaces. *Carbon* **2003,** *41* (8), 1489-1500.
49. Jun, S.; Choi, M.; Ryu, S.; Lee, H.-Y.; Ryoo, R., Ordered mesoporous carbon molecular sieves with functionalized surfaces. In *Studies in Surface Science and Catalysis*, Park, S.-E.; Ryoo, R.; Ahn, W.-S.; Lee, C. W.; Chang, J.-S., Eds. Elsevier: 2003; Vol. 146, pp 37-40.
50. Jiang, K. Y.; Schadler, L. S.; Siegel, R. W.; Zhang, X. J.; Zhang, H. F.; Terrones, M., Protein immobilization on carbon nanotubes via a two-step process of diimide-activated amidation. *J Mater Chem* **2004,** *14* (1), 37-39.
51. Titirici, M. M.; Thomas, A.; Antonietti, M., Aminated hydrophilic ordered mesoporous carbons. *J Mater Chem* **2007,** *17* (32), 3412-3418.

52. Wang, L. F.; Zhao, Y.; Lin, K. F.; Zhao, X. J.; Shan, Z. C.; Di, Y.; Sun, Z. H.; Cao, X. J.; Zou, Y. C.; Jiang, D. Z.; Jiang, L.; Xiao, F. S., Super-hydrophobic ordered mesoporous carbon monolith. *Carbon* **2006,** *44* (7), 1336-1339.
53. Cosnier, F.; Celzard, A.; Furdin, G.; Begin, D.; Mareche, J. F.; Barres, O., Hydrophobisation of active carbon surface and effect on the adsorption of water. *Carbon* **2005,** *43* (12), 2554-2563.
54. He, Q.; Xu, Y. B.; Wang, C. H.; She, S. K.; Zhou, S.; Wang, R., Silane modification and characterization of activated carbon. *Adsorption-Journal of the International Adsorption Society* **2012,** *18* (1), 23-29.
55. Stein, A.; Wang, Z. Y.; Fierke, M. A., Functionalization of Porous Carbon Materials with Designed Pore Architecture. *Adv Mater* **2009,** *21* (3), 265-293.
56. Li, Z.; Yan, W.; Dai, S., Surface functionalization of ordered mesoporous carbons--a comparative study. *Langmuir* **2005,** *21* (25), 11999-2006.
57. Kim, J. H.; Kim, T.; Jeong, Y. C.; Lee, K.; Park, K. T.; Yang, S. J.; Park, C. R., Stabilization of Insoluble Discharge Products by Facile Aniline Modification for High Performance Li-S Batteries. *Adv Energy Mater* **2015,** *5* (14), 1500268-n/a.
58. Jaffe, A.; Valdes, A. S.; Karunadasa, H. I., Quinone-Functionalized Carbon Black Cathodes for Lithium Batteries with High Power Densities. *Chem Mater* **2015,** *27* (10), 3568-3571.
59. Delamar, M.; Hitmi, R.; Pinson, J.; Saveant, J. M., Covalent Modification of Carbon Surfaces by Grafting of Functionalized Aryl Radicals Produced from Electrochemical Reduction of Diazonium Salts. *J Am Chem Soc* **1992,** *114* (14), 5883-5884.
60. Scrosati, B., History of lithium batteries. *Journal of Solid State Electrochemistry* **2011,** *15* (7-8), 1623-1630.
61. Simonin, L. In *Batteries and Na-ion batteries basics*, NAIADES Summerschool Sodium-ion Batteries: Fundamentals & Applications, Smögen, Sweden, 30-05-17; Smögen, Sweden, 2017; p 50.
62. Daniel, C.; Besenhard, J. O., *Handbook of Battery Materials*. Wiley: 2011.
63. Imanishi, N.; Yamamoto, O., Rechargeable lithium-air batteries: characteristics and prospects. *Materials Today* **2014,** *17* (1), 24-30.
64. Pang, Q.; Liang, X.; Kwok, C. Y.; Nazar, L. F., Advances in lithium-sulfur batteries based on multifunctional cathodes and electrolytes. *Nature Energy* **2016,** *1*, 16132.
65. Bruce, P. G.; Freunberger, S. A.; Hardwick, L. J.; Tarascon, J. M., Li-O2 and Li-S batteries with high energy storage. *Nat Mater* **2011,** *11* (1), 19-29.
66. Helmenstine, A. M. Table of Electrical Resistivity and Conductivity. https://www.thoughtco.com/table-of-electrical-resistivity-conductivity-608499.
67. Nazar, L. F.; Cuisinier, M.; Pang, Q., Lithium-sulfur batteries. *MRS Bulletin* **2014,** *39* (05), 436-442.
68. Chen, Z.; Jean-Pol, D.; Jiujun, Z., *Non-Noble Metal Fuel Cell Catalysts*. Wiley-VCH: 2014; p 448.
69. Williams, M. C., *Fuel Cell Handbook, 7th Edition*. US Department of Energy: 2004.
70. Moroimoto, Y., Alternative PEFC Catalysts for Future Commercial FCVs. *EFCD 2015 - Challenges Towards Zero Platinum for Oxygen Reduction* **2015**.
71. Gong, K.; Du, F.; Xia, Z.; Durstock, M.; Dai, L., Nitrogen-doped carbon nanotube arrays with high electrocatalytic activity for oxygen reduction. *Science* **2009,** *323* (5915), 760-4.

72. Wu, G.; More, K. L.; Johnston, C. M.; Zelenay, P., High-performance electrocatalysts for oxygen reduction derived from polyaniline, iron, and cobalt. *Science* **2011,** *332* (6028), 443-7.
73. Ji, X.; Lee, K. T.; Nazar, L. F., A highly ordered nanostructured carbon-sulphur cathode for lithium-sulphur batteries. *Nat Mater* **2009,** *8* (6), 500-6.
74. Carbon Black - Vulcan XC 72R. http://www.fuelcellstore.com/vulcan-xc-72r.
75. Mikhaylik, Y.; Kovalev, I.; Schock, R.; Kumaresan, K.; Xu, J.; Affinito, J., High Energy Rechargeable Li-S Cells for EV Application. Status, Remaining Problems and Solutions. *Battery/Energy Technology (General) - 216th Ecs Meeting* **2010,** *25* (35), 23-34.
76. Yuan, L. X.; Feng, J. K.; Ai, X. P.; Cao, Y. L.; Chen, S. L.; Yang, H. X., Improved dischargeability and reversibility of sulfur cathode in a novel ionic liquid electrolyte. *Electrochem Commun* **2006,** *8* (4), 610-614.
77. Tamura, T.; Hachida, T.; Yoshida, K.; Tachikawa, N.; Dokko, K.; Watanabe, M., New glyme-cyclic imide lithium salt complexes as thermally stable electrolytes for lithium batteries. *J Power Sources* **2010,** *195* (18), 6095-6100.
78. Zhang, S. S., Liquid electrolyte lithium/sulfur battery: Fundamental chemistry, problems, and solutions. *J Power Sources* **2013,** *231*, 153-162.
79. Aihara, Y.; Bando, T.; Nakagawa, H.; Yoshida, H.; Hayamizu, K.; Akiba, E.; Price, W. S., Ion Transport Properties of Six Lithium Salts Dissolved in γ-Butyrolactone Studied by Self-Diffusion and Ionic Conductivity Measurements. *J Electrochem Soc* **2004,** *151* (1).
80. Mikhaylik, Y. V., Electrolytes for lithium sulfur cells. Google Patents: 2008.
81. Ding, N.; Zhou, L.; Zhou, C.; Geng, D.; Yang, J.; Chien, S. W.; Liu, Z.; Ng, M. F.; Yu, A.; Hor, T. S.; Sullivan, M. B.; Zong, Y., Building better lithium-sulfur batteries: from LiNO3 to solid oxide catalyst. *Sci Rep* **2016,** *6*, 33154.
82. Aurbach, D.; Pollak, E.; Elazari, R.; Salitra, G.; Kelley, C. S.; Affinito, J., On the Surface Chemical Aspects of Very High Energy Density, Rechargeable Li-Sulfur Batteries. *J Electrochem Soc* **2009,** *156* (8), A694-A702.
83. Nitze, F.; Agostini, M.; Lundin, F.; Palmqvist, A. E. C.; Matic, A., A binder-free sulfur/reduced graphene oxide aerogel as high performance electrode materials for lithium sulfur batteries. *Scientific Reports* **2016,** *6*, 39615.
84. Zheng, S.; Yi, F.; Li, Z.; Zhu, Y.; Xu, Y.; Luo, C.; Yang, J.; Wang, C., Copper-Stabilized Sulfur-Microporous Carbon Cathodes for Li-S Batteries. *Adv Funct Mater* **2014,** *24* (26), 4156-4163.
85. Dombrovskis, J. K.; Prestel, C.; Palmqvist, A. E. C., Optimization of fuel cell membrane electrode assemblies for transition metal ion-chelating ordered mesoporous carbon cathode catalysts. *Apl Mater* **2014,** *2* (12), 121102.
86. Sulfur. In *Chemistry of the Elements*, Butterworth-Heinemann: Oxford, 1997; pp 645-746.
87. Moreno, N.; Caballero, A.; Morales, J.; Agostini, M.; Hassoun, J., Lithium battery using sulfur infiltrated in three-dimensional flower-like hierarchical porous carbon electrode. *Mater Chem Phys* **2016,** *180* (Supplement C), 82-88.
88. Manthiram, A.; Fu, Y.; Su, Y. S., Challenges and prospects of lithium-sulfur batteries. *Acc Chem Res* **2013,** *46* (5), 1125-34.
89. Gawande, M. B.; Goswami, A.; Felpin, F. X.; Asefa, T.; Huang, X.; Silva, R.; Zou, X.; Zboril, R.; Varma, R. S., Cu and Cu-Based Nanoparticles: Synthesis and Applications in Catalysis. *Chem Rev* **2016,** *116* (6), 3722-811.

90. McCrory, C. C.; Devadoss, A.; Ottenwaelder, X.; Lowe, R. D.; Stack, T. D.; Chidsey, C. E., Electrocatalytic O2 reduction by covalently immobilized mononuclear copper(I) complexes: evidence for a binuclear Cu2O2 intermediate. *J Am Chem Soc* **2011,** *133* (11), 3696-9.
91. Devadoss, A.; Chidsey, C. E. D., Azide-modified graphitic surfaces for covalent attachment of alkyne-terminated molecules by "click" chemistry. *J Am Chem Soc* **2007,** *129* (17), 5370-+.
92. Stenehjem, E. D.; Ziatdinov, V. R.; Stack, T. D.; Chidsey, C. E., Gas-phase azide functionalization of carbon. *J Am Chem Soc* **2013,** *135* (3), 1110-6.